Modeling and Diagnosis of Excimer Laser Ablation

A Thesis
Presented to
The Academic Faculty

by

Ronald Setia

In Partial Fulfillment
of the Requirements for the Degree of
Doctor of Philosophy
in the School of Electrical and Computer Engineering

Georgia Institute of Technology

December 2005

Modeling and Diagnosis of Excimer Laser Ablation

Approved by:

Dr. Gary S. May, Advisor
School of Electrical and Computer Engineering
Georgia Institute of Technology

Dr. Jennifer E. Michaels
School of Electrical and Computer Engineering
Georgia Institute of Technology

Dr. George J. Vachtsevanos
School of Electrical and Computer Engineering
Georgia Institute of Technology

Dr. Paul A. Kohl
School of Chemical and Biomolecular Engineering
Georgia Institute of Technology

Dr. Rao R. Tummala
School of Electrical and Computer Engineering
Georgia Institute of Technology

Date Approved: November 22, 2005

To God for the everlasting blessings and guidance

To my mother and father for their constant love and support

To my brother for his continuing friendship

To love of my heart for believing in me

ACKNOWLEDGEMENTS

I would like to express my deepest appreciation to my research advisor, Professor Gary S. May, for his constant guidance and support throughout my research endeavors. I am forever grateful to him for his patience and encouragement during difficult times in the pursuit of my academic goals. His quote "baby steps" has encouraged me to persevere in this big journey of life. Since then I have started to develop the professionalism as a researcher and be a better engineer. I would also like to thank Professor George J. Vachtsevanos and Professor Rao R. Tummala for serving on my reading committee, and extend my thanks to Professor Jennifer E. Michaels and Professor Paul A. Kohl for serving on my dissertation defense committee.

I would like to thank the Packaging Research Center staff, especially Venky Sundaram, Dr. Fuhan Liu, Mike Toole, Dean Sutter, and Boyd Wiedenman for their daily support and patience during board fabrication. Without their help, my work would neither have been successful nor complete. Additionally, I would like to acknowledge Venky Sundaram for his kind help in providing training on laser tool operation, advice about materials, as well as his valuable insights about the ablation process in particular and board fabrication processes in general.

I am grateful to the Intelligent Semiconductor Manufacturing Group members over the years, including Dr. Sang J. Hong, Dr. Rana J. Pratap, Cleon Davis, Brian Morris, and Tomas Sarmiento for their suggestions, critiques, and most importantly, for being wonderful and reliable friends. I am also grateful to the Intelligent Control Systems

Group members, including Graham Drozeski and Bhaskar Saha for our discussions regarding fuzzy logic.

I would also like to thank the National Science Foundation (Grant No. EEC-9402723) for financial support, School of Electrical and Computer Engineering and Microelectronics Research Center for cleanroom access and other tangible support of this work. I also acknowledge Hitachi Chemical, DuPont, and Cyantek for providing various materials and supplies.

I would specially thank my parents, Megadevi Setia and Dr. Budi Setia, and my brother, Albert Setia, for their forever love and support throughout my life. Their motivation and faith in me has helped me to pursue a higher education in engineering. Last but not least, I would like to thank my friend, Rungsinee Kasetpibal, for her love, care, and encouragement during my life as a graduate student.

Thank you all. I will never forget these particular years of my life.

I started with doubt in my heart and in my mind
Things could be difficult and painful
To make things more complicated, I was jealous
But then
I prayed for comfort
Miracles did happen; Details were forgotten
I learned to love
I learned to work
The concept that makes things work or go awry
The process to succeed

TABLE OF CONTENTS

LIST OF TABLES

LIST OF FIGURES

SUMMARY

Recent advances in the miniaturization, functionality, and integration of integrated circuits and packages, such as the system-on-package (SOP) methodology, require increases in both vertical and horizontal package wiring density. Microvia fabrication is an essential process that generates vertical signal paths in a high-density multilayer substrate. To meet the future needs for local microvia densities greater than 5000 per cm^2 and via diameters less than 50 μm, a scanning projection excimer laser system has been developed. To ensure repeatable and reliable laser-based microvia fabrication, the interaction between the laser and the material must be understood and the target process responses must be maintained.

In this thesis, a novel technique implementing statistical experimental design and neural networks (NNs) is used to characterize and model the excimer laser ablation process for microvia formation. Vias with diameters from 10 – 50 μm have been ablated in DuPont Kapton® E polyimide using an Anvik HexScan™ 2150 SXE pulsed excimer laser operating at 308 nm. Accurate NN models with prediction errors less than 6%, which are developed from experimental data, are obtained for several microvia characteristics, including ablated thickness, via diameter and wall angle. In addition, prediction error of less than 15% is obtained for a via resistance model. The NN models are used to perform sensitivity analysis and derive response surfaces to obtain insight on trends and impact of laser system parameters on microvia characteristics. Subsequently, NNs and genetic algorithms (GAs) are utilized to generate optimized process recipes for the laser tool. Such recipes provide the capability to produce desired target responses, including specific via diameter, steeper wall angle, and low via resistance. The

improvement achieved over the non-optimized recipes (i.e., those recipes used during the designed experiment) and the optimal recipes is as large as 40% for the ablated thickness response, 30% for top via diameter, 9% for via wall angle, and >100% for via resistance.

With continuing advancement in the use of excimer laser systems in microsystems packaging has come an increasing need to offset capital equipment investment and lower equipment downtime. Since microvia characteristics are process-dependent and the process is tool-dependent, when a process shifts, the characteristics deviate from targets. Such shifts are often indicative of necessary process adjustments or failures. Therefore, there is a need for fast, accurate, and robust automated malfunction detection and diagnosis. In this thesis, an automated *in-line* failure diagnosis system using neural networks and Dempster-Shafer (D-S) theory is implemented. For the sake of comparison, a neuro-fuzzy logic approach is also applied to achieve the same objective. Both the D-S theory and neuro-fuzzy logic are used to develop an automated inference system to specifically identify failures. Successful failure detection (100%) is achieved using NNs in 19 possible failure scenarios. Using ANFIS, only a single false alarm occurs. Successful failure diagnosis is also achieved using NN-DS technique: a single false alarm occurs in 19 possible failure scenarios. Using ANFIS, a single false alarm and a single missed alarm occur.

In essence, the four specific objectives for this research are the following: (1) to characterize and model the laser ablation process for microvia formation; (2) to optimize the ablation process for specific target responses; (3) to detect possible failures in the process; (4) to diagnose the possible sources of failures. The result of this investigation will benefit both engineering and management. Engineers will benefit from high yield,

reliable production, and low equipment down-time. Business people, on the other hand, will benefit from cost-savings resulting from more production-worthy (i.e., lower maintenance) laser ablation equipment.

CHAPTER 1

INTRODUCTION

Microsystems packaging is among the most important strategic technologies in the world. As the bridge between integrated circuits (ICs) and end-product systems, this technology is fundamentally dependent on the manufacture of microelectronic, photonic, radio frequency (RF), and micro-electromechanical systems (MEMS). The system-on-a-package (SOP) methodology, pioneered by the Packaging Research Center at the Georgia Institute of Technology, has been identified as a key approach for future packaging technologies [1-2]. The SOP technique involves two main aspects: (1) wafer-level packaging at the IC level and (2) SOP substrates with embedded system-level functions, such as high-speed digital wiring, high-bandwidth embedded optical waveguides, RF, and MEMS (see Figure 1.1).

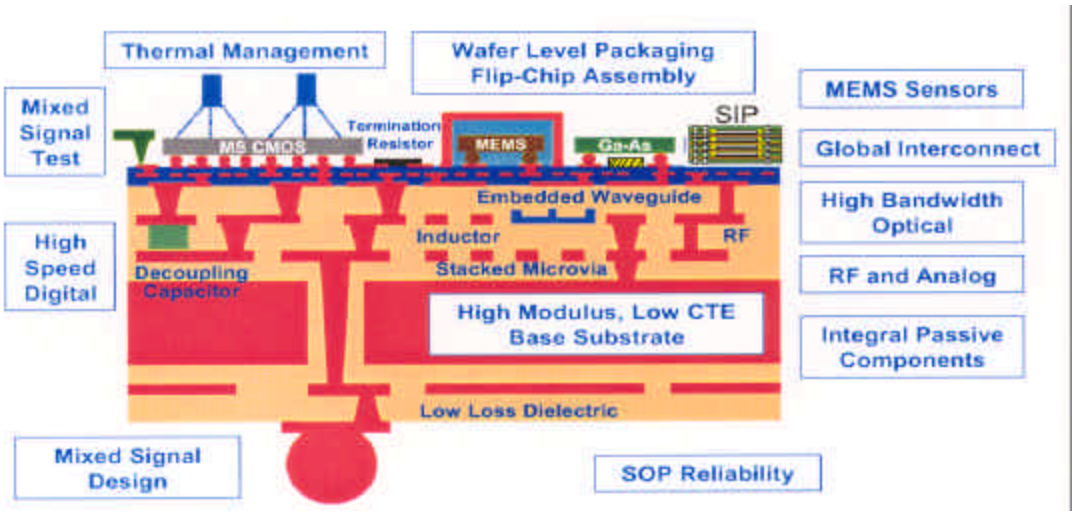

Figure 1.1. Cross-section of SOP substrate illustrating diverse technology functions.

Microsystems packaging involves power distribution to ICs and passive devices in a circuit board, as well as signal distribution among ICs and between ICs and circuit boards. Recent advances in the miniaturization, functionality, and integration of ICs and packages require increases in both vertical and horizontal package wiring density. Microvia fabrication is an essential process that generates vertical signal paths through a polymer layer in a high-density multilayer substrate. The polymer acts as an insulator between metal lines. To meet future needs for local microvia densities greater than 5000 per cm^2 and via diameters less than 50 μm, a laser-based solution has been developed.

This chapter discusses the use of lasers in the microelectronics industry, with a particular focus on the application of excimer lasers for microvia formation, along with a review of previous work aimed at understanding the laser ablation process. The chapter also presents the motivation and objectives of this research and organization of this thesis.

1.1 Lasers in Microelectronics

The use of lasers in industrial and research applications varies according to specific needs. For example, in automotive, military, and large-scale electronics applications, the laser used tends to have a high power output (in the kW range). On the other hand, in small-scale electronics, healthcare, and consumer product applications, a low-power laser is more desirable and suitable. There is also an immediate need to reduce the amount of debris generated as a byproduct in all laser-based applications. Several types of lasers, including CO_2, Nd:YAG, and excimer lasers, have demonstrated their abilities to drill/ ablate [3-11], cut [12], engrave [12], weld [12-13], clean [14], and deposit [15] various

metals and polymers in many microelectronics applications. Table 1.1 shows a key comparison of different types of lasers [4-7] [16].

Table 1.1: Comparison of laser devices.

	CO_2	Nd:YAG	ArF or XeCl
Wavelength	10.6 μm (mid-infrared)	1.064 μm (near-infrared)	193 or 308 nm (ultraviolet)
Lasing Medium	Gas	Solid State	Gas
Practical Via Size	75 – 150 μm	< 75 μm	< 50 μm
Local Thermal Damage (HAZ)	High	Medium	Low
Average Output Power	High	Medium	Low
Via Drilling	Thermal	Thermal	Ablation
Corrosive Halogen Gas	No	No	Yes
Material Bond Excitation	Outer Electron Excitation	Outer Electron Excitation	Molecular Vibrations and Rotational Excitation

The development of microvia processing has progressed steadily in recent years, and the quality of vias has become critical to the overall system performance and reliability. Currently, the five most common microvia processing approaches are wet etching, reactive ion etching (RIE), laser ablation, photosensitive polymer lithography, and mechanical drilling. Table 1.2 shows a comparison of microvia generation techniques [4-7] [16-17]. Laser ablation has several key advantages over the other methods, including the lowest number of process steps, the most desirable via shape for subsequent metallization steps (i.e., trapezoidal), and the capability of tight control over the via wall angle (with the proper combination of focal plane ablation and tool parameters, vias with wall angle up to 75^{o} have been ablated) [6-8]. Another advantage of laser-based via

generation is its high depth-to-diameter ratio (or "aspect ratio"). It has been reported that vias with an aspect ratio of up to 20:1 have been ablated [5]. To obtain smaller microvias, higher feature resolution, and lower thermal damage in microelectronics, excimer lasers – such as the XeCl laser – are used. This type of laser produces light in the ultraviolet (UV) frequency range. The excimer laser is a key method for microvia formation in packaging substrates for the SOP technology [1].

Table 1.2: Comparison of microvia generation techniques.

	Wet Etching	**RIE**	**Laser Ablation**	**Photosensitive Polymer Lithography**	**Mechanical Drilling**
Microvia Production	Large Scale	Large Scale	Large Scale	Large Scale	Small Scale
Drilling Method	Chemical	Thermal	Ablation or Thermal	Chemical	Mechanical
Process Type	Wet	Dry	Dry	Wet	Dry
Aspect Ratio	1:1.5	5:1	> 10:1	1:1.5	10:1
Number of Steps*	3	6	1	2	1
* Steps from mask deposition to etching					

As large-area microvia production is needed, an excimer laser ablation system has been developed to accommodate critical objectives of increasing the production yield and lowering manufacturing cost. This tool embodies advanced developments in laser optics, beam profile, active gas lifetime, scanning stage technology, process control, and sensors. However, a major challenge regarding the use of this tool is to offset capital investment with enhanced process modeling and optimization, as well as with advanced equipment failure detection and diagnosis. To ensure repeatable and reliable laser-based microvia fabrication, the interaction between the laser and the material must be understood and the

target process responses must be maintained. Much research has been conducted to understand the fundamental physics and chemistry involved in the laser ablation process [18-30].

1.2 Review of Previous Work

The spontaneous removal of material from the surfaces of solid organic polymers by pulsed ultraviolet (UV) laser radiation was first discovered in 1982 [18]. One of the early mathematical models introduced the idea of threshold fluence, below which material removal did not occur [19]. Later work has been devoted to explaining ablation behavior by means of a time-dependent model that includes non-linear photon absorption, plume screening on incoming radiation, and incubation effects [20-21]. Some polymers, such as poly-methyl-methacrylate (PMMA), are known to exhibit a significant incubation effect, where the ablation etch rate is affected by previous laser pulses. Polymers, such as polyimide (PI), do not show such effects significantly.

Other work studied the impact of chromophores (i.e., chemical entities within a material that allow photon absorption at wavelength of interest) and the generated plume [22-23], the effect of thermal diffusivity [24], and the effect of pulsewidth and laser intensity on threshold fluence [25]. An extension based on [22-23] using a one-dimensional heat transfer model taking into account thermal diffusivity and conductivity was proposed to predict threshold fluence and ablation etch rate for a range of fluences and pulse widths [26]. Further insight into the ablation mechanism has been obtained by a variety of techniques, including spectroscopy of the ablation products and high-speed photography [27-28].

An attempt was made to develop linear least-squares models for excimer laser micromachining that included such aspects as pulse fluence, angle of incidence, and reflection to predict surface topology and side-wall profiles [29]. Numerical models for 2-D via wall angle structures based on 3-D aerial image taking into account the partial coherence illumination and etch rate for non-normal incident radiation were also developed [30]. Another study focused on the physical microscopic views of the ablated material and an explanation of the ablation process as a function of laser fluence and pulse width using a molecular dynamics approach [28].

The previously mentioned work involved the use of physical and numerical models to understand the interactions between the laser and the material. Another modeling technique, namely, statistical modeling based on designed experiments and analysis of variance (ANOVA), has also gained popularity for understanding such complex interactions. This technique is advantageous for studying the relationship between a large number of input parameters (i.e., > 4 parameters) and process responses when physical models are too complicated or time consuming to develop. Many authors have conducted such studies, particularly with regard to laser drilling sheet metals using a pulsed Nd:YAG laser. One study employed a full-factorial design to investigate the effects of laser energy, focal plane position, thickness, vacuum pressure, and material specification in single-pulsed laser drilling on microvia quality [31]. Another study was performed using the response surface method (RSM) together with the central composite design (CCD), taking into account the laser peak power, pulse width, pulse frequency, number of pulses, assist gas pressure, and focal plane position in multi-pulsed laser drilling to study via quality [32].

In efforts to better understand excimer laser-based material removal, both academic and industrial researchers have done a great deal. For example, IBM research centers conducted pioneering studies involving key laser parameters (e.g., laser fluence, pulse width, laser wavelength, number of pulses, and repetition rate) and tool parameters (e.g., mask technology and focusing mirror) affecting polymer ablation, thus via formation [6-8] [33]. These studies transformed the basic understanding of the laser ablation process from pure science to include practical needs and product-oriented results.

In recent years, several studies have been conducted that used neural networks for the empirical modeling and prediction of different laser processes. One study used a CO_2 laser for a paper cutting application, and the process was modeled using neural networks [34]. The input parameters included laser power, cutting speed of the laser, temperature of the roller, pressure of the roller, and rolling speed, whereas the process response was laser cutting width. Another attempt to use neural networks to model the CO_2 welding process of stainless steel butt joints was conducted [35]. In this study, laser power, laser speed, and joint thickness were selected as inputs to the model, whereas the melted volume-energy input ratio, weld crown, and depth were selected as the outputs. In a metal removal application using an Nd:YAG laser, neural networks were used to model the pulse energy, variance of depth, and variance of diameter using the mean depth and mean diameter of the crater and material property as the inputs [36]. All efforts have shown that the neural network modeling approach successfully predicted the behavior of laser processes with a high degree of accuracy supported by experimental data. These efforts have provided the motivation to understand laser ablation process for microvia formation using neural networks.

1.3 Research Motivation and Objectives

Although previous work has been aimed at understanding the laser ablation process, none to date has used neural networks (NNs) [37] to model the excimer laser ablation process. Most of the physical models developed in previous studies involved a small number of parameters (i.e., < 3 parameters) of interest, and the responses modeled were not practical from a manufacturing point of view. Many simplifying assumptions were also made to the physical models to reduce complexity, resulting in less accurate models. Numerical models, on the other hand, provide sufficient accuracy but are computationally extensive. In many cases, simplifying assumptions were also made to these models. Examples of such assumptions include linear (as opposed to non-linear) energy absorption within materials, perpendicular (as opposed to non-perpendicular) angle of light incidence, a certain beam profile distribution, and the non-effect of the residual thermal energy in the non-degraded material on subsequent ablation [24][26][29-30]. In addition, the results obtained from physical and numerical methods can vary from the measured data because of process variations. Previous efforts have also implemented an ad-hoc experimental approach, as opposed to a systematic experimental design method, which is a much more effective way of studying relationships between multiple input factors and responses.

Empirical modeling techniques, such as statistical modeling [38-39] and NNs, make no assumptions regarding the physical or chemical aspects of a process. However, the statistical technique has some drawbacks. This method is simple to implement and interpret, but limited in range and accuracy. There is a serious trade-off among the amount of experimental data available, complexity of the regression model, and accuracy

of the model. Neural networks, on the other hand, have the intrinsic capability to model a non-linear and complex process (such as a laser ablation). Moreover, NN models also exhibit less prediction error and better model generalization accounting for manufacturing variations and parameter indeterminacy issues [40-43].

In this thesis, the main motivation for using the NN technique is not solely for process modeling. The technique is also used in conjunction with genetic algorithms (GAs) [44] for process optimization and as an enabling mechanism for malfunction diagnosis. Models that characterize the relationship between the laser ablation process conditions and responses have been derived using statistical experimental design in conjunction with neural networks. The experimental design method was utilized to identify the significance of input parameters affecting responses. The significant parameters were then used as inputs to neural network models. GAs were used as a recipe synthesis procedure to provide optimized sets of values of input parameters to achieve (potentially conflicting) process objectives.

With continuing advancement in the use of excimer laser systems in microsystems packaging has come an increasing need to offset capital equipment investment and lower equipment downtime. Since microvia characteristics are process-dependent and the process is tool-dependent, when a process shifts, the characteristics deviate from targets. Such shifts are often indicative of necessary process adjustments or failures. Therefore, there is a need for fast, accurate, and robust automated malfunction detection and diagnosis. In this thesis, an automated *in-line* failure diagnosis system using neural networks and Dempster-Shafer (D-S) theory [45-46] was implemented. For the sake of comparison, a neuro-fuzzy logic approach [47-48] was also applied to achieve the same

objective. Both the D-S theory and neuro-fuzzy logic were used to develop an automated inference system to specifically identify failures.

In summary, the four specific objectives for this research are the following: (1) to characterize and model the laser ablation process for microvia formation; (2) to optimize the ablation process for specific target responses; (3) to detect possible failures in the process; (4) to diagnose the possible sources of failures. The result of this investigation will benefit both engineering and management. Engineers will benefit from high yield, reliable production, and low equipment down-time. Business people, on the other hand, will benefit from the cost savings resulting from more production-worthy (i.e., lower maintenance) laser ablation equipment.

1.4 Thesis Organization

The remainder of this thesis describes the neural networks and genetic algorithm-based methodology for the modeling and optimization of excimer laser ablation. It also discusses the use of neural networks, Dempster-Shafer theory, and neuro-fuzzy logic for failure detection and diagnosis. Chapter 2 provides descriptions of excimer laser ablations and the materials used in fabrication. It also presents the laser input parameters and responses, as well as the mask design used in the scanning projection laser system. Chapter 3 describes the microvia fabrication steps and the characteristics of microvias measured. Chapter 4 describes the neural networks used in this research. Chapter 5 presents the modeling results and sensitivity analysis using the excimer laser ablation neural network models. In Chapter 6, laser process optimization using neural networks and genetic algorithms is presented. Run-to-run failure detection and diagnosis of the

excimer laser ablation process using Dempster-Shafer theory and neuro-fuzzy logic is presented in Chapter 7. Finally, Chapter 8 summarizes the main contributions of this thesis and lists potential future research directions.

CHAPTER 2

EXCIMER LASER ABLATION

LASER is an acronym for "light amplified stimulated emission of radiation". In general, a laser beam can be generated by incorporating a laser medium (gas, liquid, or solid), a pumping process that achieve a population inversion, an optical feedback system for light amplification, and a laser cavity for determining the frequency [49]. All laser beams possess distinct properties: single wavelength (i.e., monochromaticity), low divergence, high density of photons, and phase coherence. The use of lasers for material processing has several advantages over the other types of methods, including non-contact between the tool and the material reducing chance of damage to the material, no chemical solvents (reducing waste handling costs), selective material removal, and advanced computer control and automatic handling [16].

An excimer laser uses gas as the active medium. Table 2.1 shows the typical gas mixtures used to produce an excimer laser [16][49]. The wavelength of the beam produced is typically in the range of 193 – 351 nm. The first demonstration of an excimer laser was in the late 1970's. Since then, many improvements have occurred, including increased gas lifetime, upgraded electronics for computer control, sensors for process monitoring, and scanning stage technology.

Table 2.1: Excimer gas mixtures.

Mixture	Wavelength	Gas Lifetime	Average Power
F_2	157 nm	10^5 pulses	< 5 Watts
ArF	193 nm	10^6 pulses	30 Watts
KrCl	222 nm	2 x 10^6 pulses	30 Watts
KrF	248 nm	10^7 pulses	50 – 200 Watts
XeCl	308 nm	2 x 10^7 pulses	50 – 200 Watts
XeF	351 nm	10^6 pulses	< 50 Watts

The pumping mechanism for excimer lasers, such as the XeCl laser, is electronic with up to 45 kV DC voltage by means of a gas discharge. When pumped by the gas discharge, the Xe and Cl atoms are ionized and they form the excited dimer molecule. The lifetime for the molecule is typically less than 5 ns, during which stimulated emission must occur or the atoms will fall to their ground state spontaneously or through collisions. In the gas mixture, neon atoms constitute most of the volume. The neon acts as a third body collision partner in the formation of the excited $XeCl^*$ dimer molecule. The pulse forming network consists of a thyratron switch (solid state or hydrogen), magnetic pulse compression circuit, and storage capacitors. When the thyratron switch is closed, a high voltage spike is impressed across the pre-ionization pins and electrodes, ionizing the gas and pumping the excimer atoms to their excited state; thus, creating a plasma. The electrons in the gas plasma are accelerated by the electric field between the electrodes as they transfer their kinetic energy to the surrounding atoms. The excited dimer molecules are created by inelastic collision with the electrons. These molecules have an approximate lifetime > 5 ns in their excited state and will decay spontaneously if not stimulated by an additional photon. The laser transition step is initiated by those photons produced by stimulated emission along the laser axis. These photons are reflected back along the axis by the resonator optics at each end of the laser so that they

may subsequently cause stimulated emission with other excited molecules. The laser emission occurs in about a 20 ns pulse because the electronic circuitry can not sustain a constant high voltage and the gas discharge is short-lived. After the pulse is completed, the gas constituents require a 100 ms relaxation period before they can participate in the next discharge cycle. Figure 2.1 shows the basic components of an excimer laser [16][50].

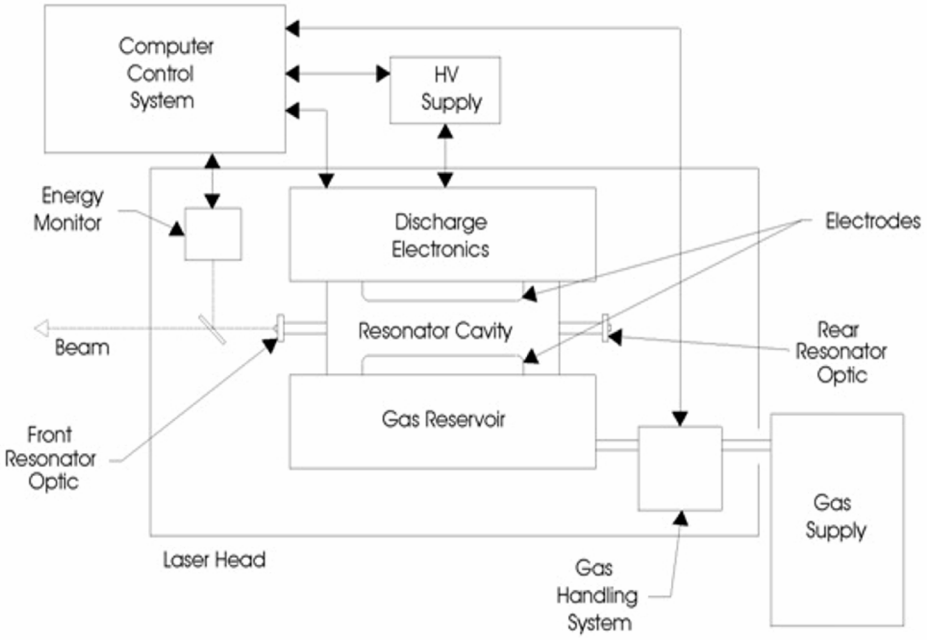

Figure 2.1. Basic components of an excimer laser.

2.1 Laser Equipment and Material

Excimer laser ablation is a material removal process that uses localized thermal energy caused by stimulated radiation. According to the Merriam-Webster dictionary, to ablate means "to remove especially by evaporating" [51]. In general, ablation occurs

when a material absorbs the light energy strongly at the laser's wavelength and the absorbed energy density is beyond the material mechanical threshold [11][28][33], as shown in Figure 2.2. Some of the advantages of excimer lasers over the other types of lasers include low thermal damage (or low heat-affected zone), high-resolution, and low average power.

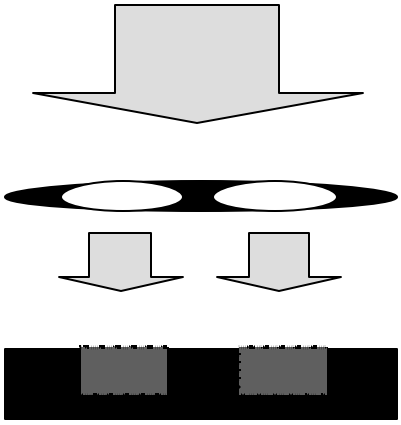

a) Absorbed laser energy density exceeds material threshold

b) Broken molecular bonds result in "gas-like" state

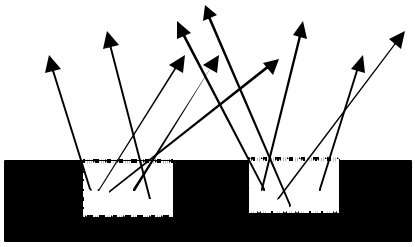

c) Particles ejected due to rapid volume expansion

Figure 2.2. Steps in polymer laser ablation.

In this research, an Anvik HexScan™ 2150 SXE excimer laser system (shown in Figure 2.3) was utilized. This tool emits an ultraviolet (UV) laser with primary operating wavelength of 308 nm and pulse duration of 14-26 ns. The laser uses a xenon chloride (XeCl) gas mixture as the active component to produce the pulsed light. The thyratron switch is hydrogen-based, and the partial pressure of hydrogen inside the thyratron is maintained by a voltage applied to the thyratron's reservoir (see Figure 2.1). The Anvik tool incorporates projection mask technology, as shown in Figure 2.4. The substrate and the mask are positioned rigidly on a single planar stage capable of moving in both *x* and *y* directions. The tool implements scanning technology with hexagonal illumination such that the complementary overlap between adjacent hexagonal scans produces a seamless and uniform energy exposure over the whole substrate [52-53]. Additionally, the laser system incorporates a debris removal system (see Figure 2.5) consisting of a flow of helium gas and two nozzles: one to release the gas and the other to take in debris generated during ablation. The debris removal system can be manually adjusted both in the vertical and horizontal directions.

Figure 2.3. Anvik laser system.

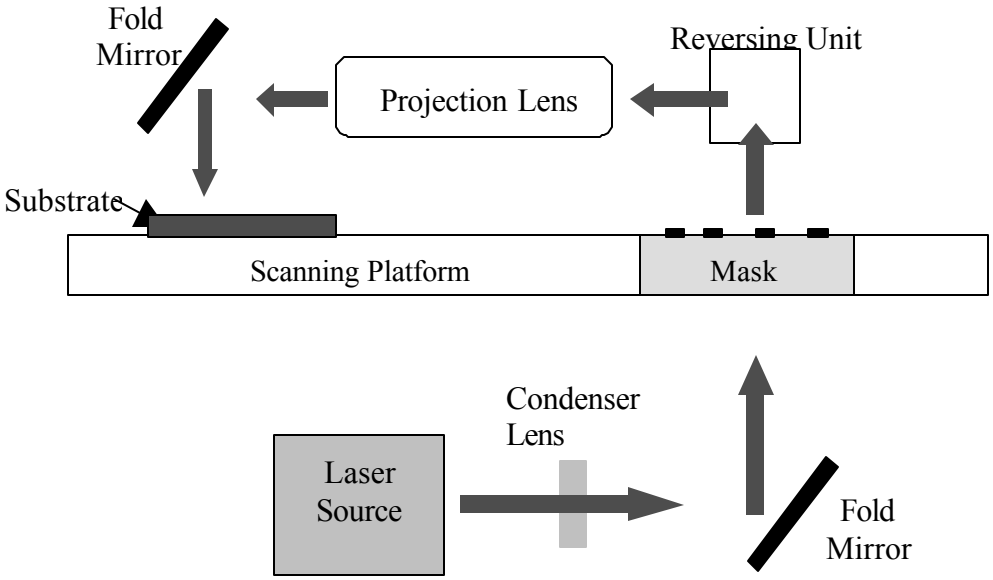

Figure 2.4. Schematic of Anvik's projection mask technology showing a substrate and a mask held rigidly on a single planar stage capable of moving in both *x* and *y* directions.

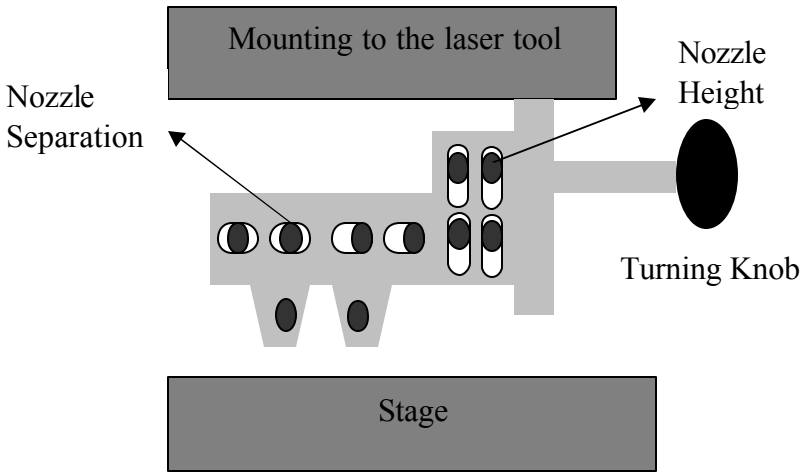

Figure 2.5. Anvik debris removal system.

Vias with diameters in the range of 10 – 50 μm were fabricated, and they were ablated in 25 μm thick DuPont Kapton® E polyimide using the Anvik tool. The polymer

is manufactured as DuPont Pyralux® TM122500ME resin-coated copper (RCC). Table 2.2 and Table 2.3 describe the properties of the polymer.

Table 2.2: DuPont Pyralux® description.

Symbol	Meaning
TM	Product name
12	1st copper layer thickness, µm
25	Polymer thickness, µm
00	2nd copper layer thickness, µm
M	Tie coat metal: monel = Ni-Cu
E	Kapton® E

Table 2.3: Properties of Kapton® E.

Properties	Value
Dielectric Constant (1 MHz)	3.2
Dissipation Factor (1 MHz)	0.003
Dielectric Strength	235 kV/mm
Moisture Absorption	1.8%
Coefficient of Thermal Expansion (CTE)	16 ppm/^{o}C
Tensile Strength	280 Mpa
Tensile Modulus	5250 Mpa

The choice of the polymer used in this research was determined based on potential success as the dielectric insulator in the system-on-package (SOP) technology substrate and the fact that Kapton® E polyimide can be easily ablated using the Anvik tool.

2.2 Laser Input Parameters and Responses

Several key laser input parameters were selected, and their relationships with the characteristics of microvias were studied. The input parameters can be adjusted by the operator. The laser fluence (measured in mJ/cm^2/pulse), shot frequency (in Hz), number

of pulses, and vertical ("up" and "down") and horizontal ("side" and "middle") positions of the debris removal system in the laser tool were selected. The first three parameters are quantitative factors and are characteristics of the laser, whereas the other two are qualitative factors and are part of the debris removal system. The microvia characteristics measured include ablated thickness, top and bottom via diameter (which are used to derive the sidewall angle), and the electrical resistance. The resistance measurements on metal deposited in the ablated vias were conducted to characterize the degree to which debris remaining inside the vias affected via quality.

2.3 Mask Design

As stated previously, the Anvik laser system incorporates scanning projection mask technology in which a substrate and a mask are held rigidly on a single planar stage capable of moving in both *x* and *y* directions (see Figure 2.4). There exist features on the mask representing microvias with diameters range from 10 – 50 μm. The features are clear, allowing the laser to pass through several optical objects and ablate the substrate. The rest of the area of the mask is reflective from the side of incoming laser. The reflected light increases the usage efficiency of the laser.

The size of mask is 6 × 6 inch (or 15 × 15 cm), with 32 replicates of each via size (Figure 2.6). The location of each via size on the mask is random. The mask is made of aluminum on quartz suitable for excimer laser. The thickness of the Al is 0.2 mm, while, the total thickness of the mask is approximately 3 mm (or 120 mil). The pattern was designed using the APD/Cadence design software package [54].

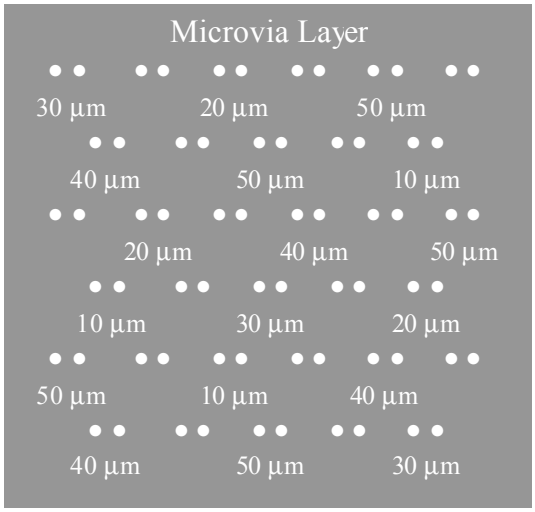

Figure 2.6. Microvia mask layout.

2.4 Summary

The behavior of an excimer laser is complex, and the interactions between the laser and the material being processed requires a high level of understanding, particularly in a manufacturing environment. This chapter introduced the operating principles of an excimer laser, provided a description of the laser system – including projection mask design and the material used for microvia fabrication. Key laser input parameters were presented, as well as the characteristics of microvias that serve as process responses. In the next chapter, the details of microvia fabrication are described.

CHAPTER 3

MICROVIA FABRICATION

The microvia structures were fabricated using the Anvik laser system in a class 1000 cleanroom. The substrate was 1-mm thick Hitachi Chemical FR-4 (MCL-E-679F), with 18-μm dual copper cladding fabricated on both sides of the glass-impregnated epoxy resin. The size of the substrate was approximately 15 cm × 15 cm (or 6 inch × 6 inch).

3.1 Fabrication Steps

3.1.1 Pre-Ablation Processing

Several process steps, including organic cleaning, baking, and hot pressing of the samples, had to be performed prior to the laser ablation process. Organic cleaning using acetone, methanol, and isopropanol (in that order) was applied to the substrate to remove fingerprints, dust, and other organic particles or residue. Afterwards, the substrate was pre-baked at 85 ^{o}C for 30 minutes to remove solvents. DuPont Pyralux® TM122500ME resin-coated copper (RCC) was then hot-pressed on top of the DuPont Pyralux® FR0100 acrylic adhesive to establish a mechanical bond to the substrate. The DuPont Pyralux® material uses dry film Kapton® E polyimide as the resin.

The polyimide thickness was 25 μm (1 mil), and the copper thickness was 12 μm. The thickness of the adhesive layer was 25 μm. The hot press conditions were 300 psi of pressure at 370 ^{o}F for 85 minutes to guarantee good adhesion of the RCC and the substrate. These conditions were safe for the FR-4 board due to its high glass transition

(T_g) and high modulus. DuPont Teflon® was also used during the process to prevent the samples from sticking to the plates. Figure 3.1 shows the schematic of the materials used in the hot-press process.

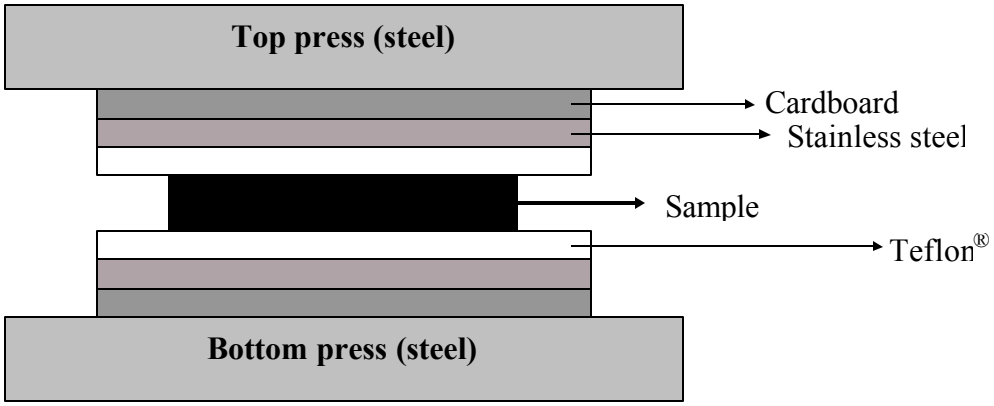

Figure 3.1. The schematic of materials used in the hot-press process.

3.1.2 Laser Ablation

The laser ablation process took place after the hot press using the Anvik tool at varying conditions for each test sample. Figure 3.2 shows the flow for the experiments prior to laser ablation. An aluminum-on-quartz mask was used as a projection mask to fabricate the vias. Vias with diameters of 10, 20, 30, 40, and 50 µm were ablated on each substrate. Each via size had 32 replicates positioned across the substrate. This process was conducted in an automated mode in which the tool stage moved in both *x* and *y* directions in a serpentine fashion, while the laser beam, lenses, and optical components were stationary. The stage moved with a user-supplied velocity in the *x* direction based on the shot frequency and number of pulses. To preserve a seamless and uniform energy exposure over the whole substrate, the stage moved in the *y* direction with a constant

velocity. Laser processing took for 20 – 50 minutes per board, depending on the stage velocity. Figures 3.3 show an example of ablated 50 μm vias.

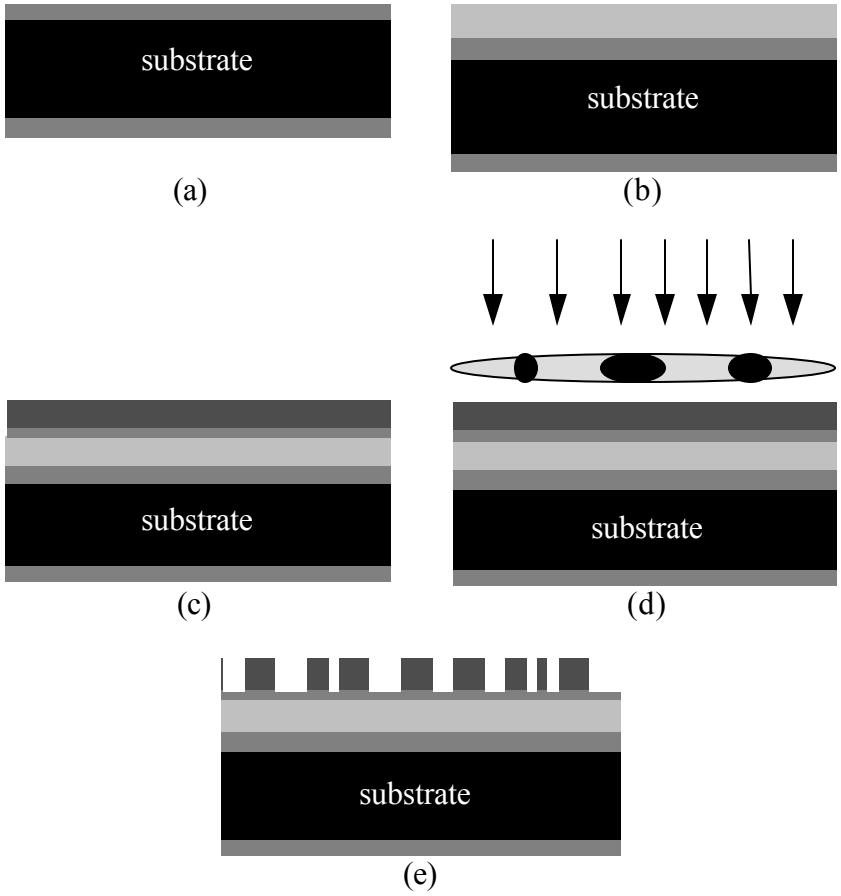

Figure 3.2. Process flow for the experiments:
(a) substrate preparation; (b), (c) hot pressing the acrylic adhesive layer and the Pyralux® RCC; (d) ablation of the Kapton® E polyimide through a projection mask;
(e) creation of microvias.

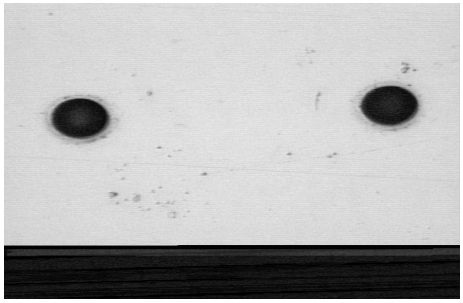

Figure 3.3. Ablated 50 μm vias.

3.1.3 Post-Ablation Processing

After ablation, the next steps in the process were to deposit copper inside the ablated vias and create copper pads for resistance measurement purposes. The metallization process consisted of two primary steps: DC sputtering chromium and copper seed layers and electrolytic plating of copper. Sputtering deposited a few hundred angstroms of chromium and copper. The chromium layer was used to provide good adhesion to the polyimide. Electrolytic plating was used to deposit 12 μm of copper. Standard photolithography was implemented to pattern the copper pads. The photoresist used was DuPont Riston® FX515 (negative resist). In the photolithography process, the photoresist was laminated on the board using a vacuum laminator. The tool was for 75°C, 80 psi, and one minute processing. Subsequently, the resist was exposed with UV light with a power density of 9mW/cm^2 for twelve seconds. The resist was developed using 1% DuPont D-4000 liquid concentrate in water solution. This process was run at 45°C for 90 seconds.

Metal etching steps were performed after the resist development. First, the copper layer was etched away using mixture of sodium persulfate (Na2S2O8) powder and amitrole (C2H4N4 catalyst) diluted in water for 30 minutes. Then, the chromium layer was etched using Cyantek CR-100 for one minute. The photolithography process concluded with the stripping of resist using PCI Specialty Chemicals UltraStrip® 6600 liquid at 55°C for twelve seconds. Resistance measurements took place afterwards. Figure 3.4 and 3.5 show the process flow and a finished test sample, respectively.

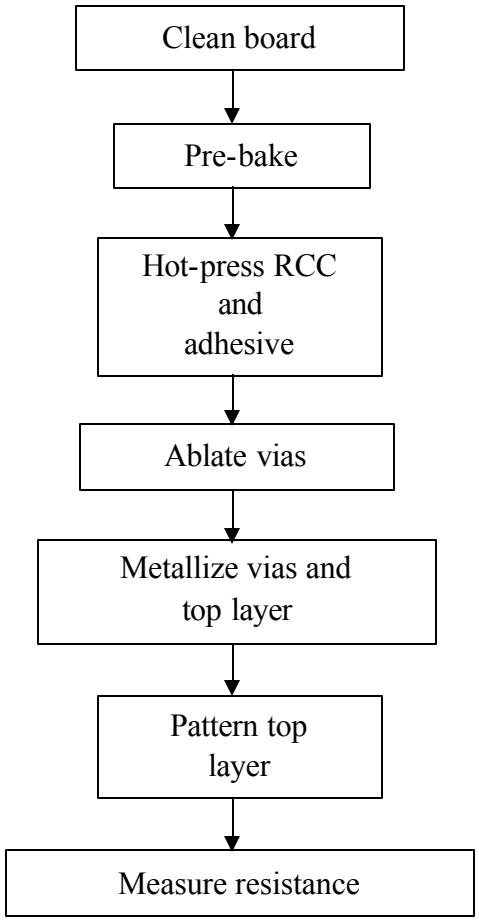

Figure 3.4. Process flow.

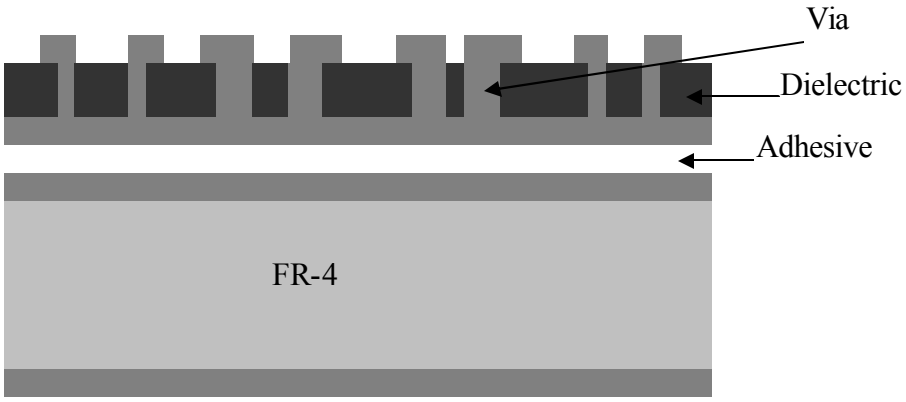

Figure 3.5. Test structure diagram (cross-sectional view).

3.2 Via Characterization

Twenty-four to twenty-six measurements of the top via diameter and via wall angle and 10 – 13 measurements of the via resistance for each via size per board were performed. The ablated dielectric thickness was measured using a Veeco Dektak 3030 Profilometer. The top via diameter was measured using a Nikon Microscope. The via wall angle (θ, in degrees) was derived from top and bottom via diameter measurements using:

$$q = 90^{o} - \arctan\left(\frac{d_t - d_b}{2 \times t_d}\right) \tag{3.1}$$

where d_t is the top via diameter, d_b is the bottom via diameter, and t_d is the dielectric thickness (25 μm). The resistance of the ablated microvias was measured using a digital ohmmeter. These measurements were then divided into two groups: one was used to train the neural networks, while, the other was used to validate them. Figure 3.6 illustrates via characterization.

3.3 Summary

In this chapter, the fabrication steps for microvia formation and measurements were presented. Next, a description of the neural networks used in this research is described. The description includes neural network structure, the learning method, and the implementation used for this research.

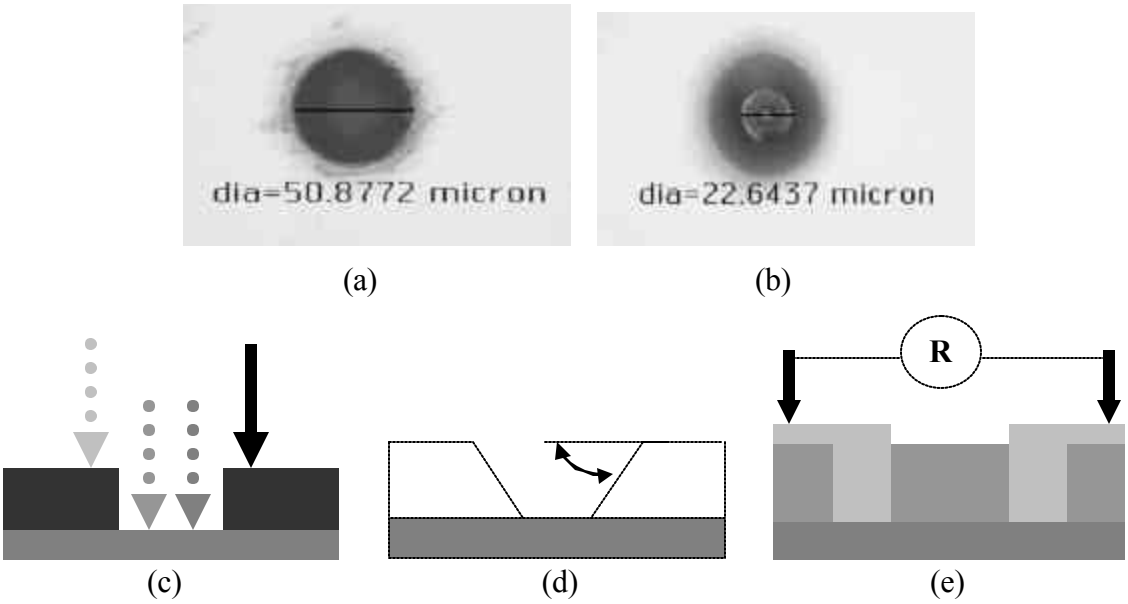

Figure 3.6. Microvia characteristics: (a) and (b) measured top and bottom ablated 50 µm via; (c) measured ablated dielectric thickness; (d) calculated via wall angle using (a) and (b); (e) measured via resistance.

CHAPTER 4

NEURAL NETWORKS

Neural networks (NNs) are an artificial intelligence approach in which biological neurons are represented by a mathematical model. Neural networks offer a fast, efficient, accurate, and cost-effective method of process modeling. The ability of a NN to capture complex input/output relationships from limited data is very valuable in microelectronics packaging fabrication, where manufacturing processes, such as laser ablation, exhibit nonlinear behavior and experimental data for process modeling is difficult and expensive to obtain [55]. In addition, it has been reported that neural network models exhibit as much as 40-70% improvement in experimental error, as well as nearly 40% improvement in generalization, as compared to statistical response surface models [40][43]. NN models also facilitate robust recipe synthesis.

4.1 Structure

Neural networks consist of interconnected computational nodes, called *neurons*, for which knowledge regarding the input/output relationship is stored in the *weights* (or connection strengths) between nodes. Neurons that receive stimuli from outside the network are called input neurons. Neurons whose responses are used externally are called output neurons. The remaining neurons within the network are called "hidden" neurons. A general multilayer perceptron feed-forward NN structure consists of multiple neurons in one input layer, one or more hidden layers, and one output layer (see Figure 4.1). This type of NN is capable of approximating several classes of functions, including continuous

and integrable functions [56]. Each neuron computes the weighted sums of its inputs filtered by a sigmoidal activation function, thereby providing the neural networks with the ability to generalize with an added degree of freedom not available in statistical regression techniques [39]. An example of such an activation function is

$$y_j(n) = \frac{\exp(x_j) - \exp(-x_j)}{\exp(x_j) + \exp(-x_j)} \tag{4.1}$$

where, x_j is the weighted sum of neural inputs, and $y_j(n)$ is the output of neuron j at iteration n. The neurons in the input and output layers corresponded to the input factors and the process responses, respectively. The number of neurons in the hidden layer(s) is varied to give the best modeling results for the input/output mapping. A large number of hidden neurons is required to model complex relationships; however, too many may result in an overtrained network and result in poor generalization [57].

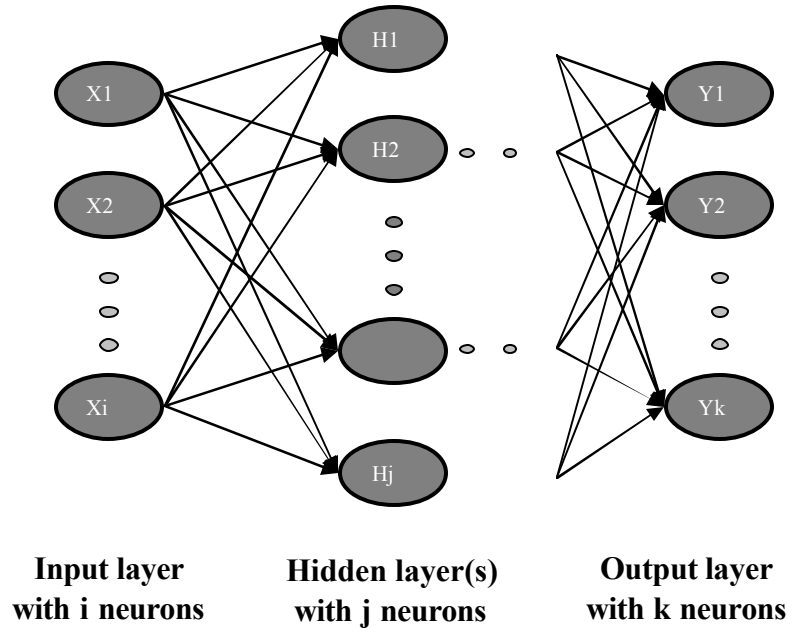

Figure 4.1. Typical feed-forward neural network structure.

4.2 Learning

In this research, the feed-forward neural networks progress through a supervised learning stage by means of constructing relationships between the inputs and the outputs. The NNs are trained using the error back-propagation (BP) algorithm. Although there exists other training algorithms, the BP method is the most popular and simplest to implement for non-linear mapping. In the BP algorithm, the NN starts with a random set of weights, and the input data is scaled to a range of ±1. Then, the network output is calculated using the initial weight matrix and compared with a target to generate an error value. Forward propagation occurs using (4.1), in which $x_j(n)$ is given by

$$x_j(n) = \sum_{i=0}^{p} w_{ji}(n) y_i(n) \tag{4.2}$$

where $w_{ji}(n)$ is the synaptic weight connecting the output of neuron i to the input of neuron j at iteration n.

The algorithm iteratively updates the weight matrix using the *gradient descent* approach to minimize the root-mean-squared error (RMSE) for all the I/O pairs, which is defined as the Euclidean distance in the weight space between the network output and its target. The root-mean-squared error (RMSE) is given by:

$$RMSE = \sqrt{\frac{1}{n-1}\sum_{i=1}^{n}\left(y_i - \hat{y}_i\right)^2} \tag{4.3}$$

where n is the number of trials and y_i is the measured values of each response, and y_i is the neural model output. The value of a weight at the $(n+1)^{th}$ iteration is given by

$$w_{sr}(n+1) = w_{sr}(n) + \alpha \Delta w_{sr}(n) + \eta \Delta w_{sr}(n+1) \tag{4.4}$$

where Δw_{sr} is the calculated change in that weight that reduces the error function of the network. The parameter η is a positive learning rate, and α is the momentum constant. The learning rate determines the speed of convergence by regulating the step size. If the learning rate is too large or too small, however, the network can become unstable or need longer training time, respectively. Typical values of the learning rate range from 0.01 – 0.7. The momentum term gives each connection some inertia proportional to the weight change from the previous iteration, resulting in an increase of the effective learning rate. This increased effective learning rate reduces the potential of the network of being trapped in local minima, thus providing faster convergence that is less susceptible to oscillation [37]. The momentum constant typically ranges from 0 – 0.3.

Training concludes when the scaled RMSE converges to a user-defined value, typically 0.05 or less. The networks in this thesis are trained by epoch, which means that no network weights are updated until the network has been exposed to all available training vectors (one epoch is one pass through all the training vectors). Figure 4.2 shows an example of the network structure for the excimer laser ablation response.

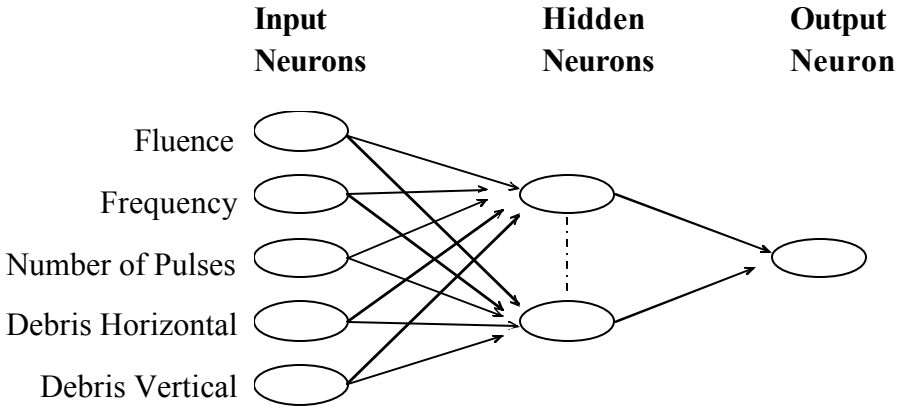

Figure 4.2. Laser ablation neural network model.

4.3 Implementation

To build the neural network models for this research, the Object-Oriented Neural Network Simulator (ObOrNNS) is used. ObOrNNS is a Java-based software package developed by the Intelligent Semiconductor Manufacturing Group at the Georgia Institute of Technology that allows the user to create, train, and test multilayer perceptron NN models [58]. ObOrNNS implements the error back-propagation training algorithm. ObOrNNS also contains an optimization routine based on genetic algorithms for use in recipe synthesis. This software is used to generate optimal process recipes for the excimer laser ablation to achieve specific microvia targets. As a Java-based application, the program is available to all platforms that support the Java Runtime Environment. To create a network, the user must specify the structure of the feed-forward network by providing the number of layers and the number of neurons in each layer. There must be at least three layers in a network. The first layer is considered the input layer, while, the last layer is the output layer. After a network is created, the user can view the network structure and select training parameters for the network. These parameters include: selecting datasets, activation functions, learning rate, momentum, and training error (scaled value), randomizing network weight, shuffling data vectors during training, saving networks, and testing networks. After training a network, the users can validate it. Both datasets for testing and training a network are automatically scaled to [-1, 1] and [-0.5, 0.5], respectively. After the network output is displayed (unscaled value), the users can save the network and load it for future use. In this research, the inputs to the feed-forward NN models of the excimer laser ablation are the laser input process parameters. The NNs predict the microvia characteristics.

In process failure detection and diagnosis, however, the inputs and the outputs of the NN models are reversed. In other words, the inputs are the microvia characteristics, and the process responses originating directly from the laser tool serve as the failure symptoms. The NNs predict the laser input process parameters that are the root cause of the observed evidence. During training, 75% of the data acquired from the experimental trials is used, while, the remaining 25% is used to derive prediction error.

4.4 Summary

This chapter describes the feed-forward neural networks used in this research. The NNs are trained using the error back-propagation algorithm to construct input/ output mappings. The Object-Oriented Neural Network Simulator (ObOrNNS) is used to create, train, and validate NN models. This NN structure is used throughout the remaining of the thesis for modeling the excimer laser ablation process, optimizing the process in conjunction with the genetic algorithms, and diagnosing process failures using Dempster-Shafer theory. In the next chapter, modeling the laser ablation process for microvia formation is presented, and the results are used to generate three-dimensional contour plots of the I/O relationships of the process. The models are also used for sensitivity analysis.

CHAPTER 5

MODELING EXCIMER LASER ABLATION

As mentioned in Chapter 1 and 2, excimer laser ablation has several advantages over the other types of methods for microvia formation in a multilayer microsystems substrate. Those advantages include non-contact between the tool and the material, no chemical solvents, selective material removal, the lowest number of process steps, the most desirable via shape for subsequent metallization steps (i.e., trapezoidal), and high depth-to-diameter ratio (or "aspect ratio"). Since the quality of the laser ablation process is influenced considerably by the process set points, studies that characterize the relationship between these conditions and the characteristics of the vias formed are necessary. In this chapter, models that characterize the relationship between laser ablation process conditions and responses are achieved using statistical experimental design and neural networks. The NN models are then used to generate three-dimensional contour plots of the I/O relationships of the process. The models are also used for sensitivity analysis. A flow chart for this chapter is shown in Figure 5.1.

5.1 Screening Experiment

The first step to facilitate a better understanding of the relationship between the laser input parameters and characteristics of microvias is to perform sets of experiments, measure the responses, and analyze the data. Such an analysis was conducted using a statistical method (i.e., analysis of variance [ANOVA]) to determine significant input parameters affecting process responses [38]. This method is called screening experiment.

The significant input parameters found from this study were used in subsequent neural network modeling.

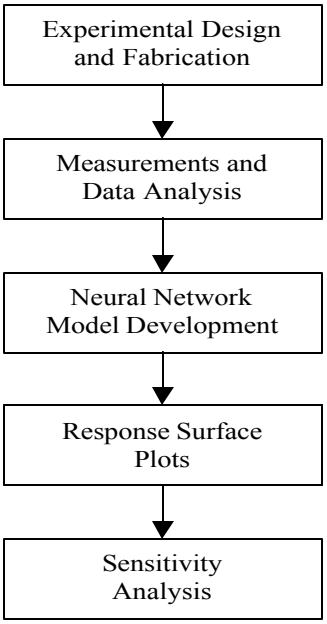

Figure 5.1. Flow chart for modeling and analysis.

5.1.1 Experimental Design

Statistical experimental design was used to characterize the effect of laser ablation conditions on fabricated vias. This approach consists of a systematic series of trials in which purposeful changes are made to the input factors of a process so that the corresponding changes in the output factors can be observed and identified [38]. The experimental design method is a suitable tool for process characterization, development, and troubleshooting to improve performance or to obtain a process that is robust and insensitive to external sources of variability.

The tool used for experimental design and analysis was the *RS/Discover*® commercial software package [59]. An experiment employing a 2^{5-1} fractional factorial design

(requiring 16 trials) was conducted to study the significance of the five factors affecting the quality of the vias. The input factors varied were laser fluence, shot frequency, number of pulses, and the vertical and horizontal positions of the debris removal system. The first three factors are quantitative, whereas the latter two are qualitative. The responses were the top via diameter, via wall angle, via resistance, and the ablated thickness of the dielectric. The via resistance measurement was conducted on the copper deposited in the ablated vias, and the measured data was used to study the effect of the debris generated (in the form of carbon residue) during the via fabrication. The experimental input factors and their respective ranges are shown in Table 5.1. The order of the experimental trials was randomized to minimize the effect of any nuisance factors that might influence the observed responses.

Table 5.1: Input factors and ranges of experimentation.

	Input Factors	**Range**
1	Laser Fluence	100 – 200 mJ/cm^2/pulse
2	Shot Frequency	100 – 150 Hz
3	Number of Pulses	500 – 1000
4	Vertical Position of Debris Removal	Up and Down
5	Horizontal Position of Debris Removal	Middle and Side

Initially, it was found that vias were not opened under most experimental conditions. To rectify this situation, an adjustment on the minimum laser fluence was implemented. The initial value of the minimum laser fluence, 100 mJ/cm^2/pulse, was increased to 175 mJ/cm^2/pulse, and the experiments with the minimum laser fluence were then repeated.

Table 5.2 – 5.5 show the experimental data for the ablated dielectric thickness, top via diameter, via wall angle, and via resistance based on the fractional-factorial design. The measurements for ablated thickness and bottom via diameter showed that the 10 and 20 μm vias were not completely opened under the adjusted range of experimentation. Further increase to the fluence or frequency was not performed due to maintaining broad range of study and the fact that damaging results (i.e., burned and cracking) occurred on the polyimide. The resistance measurement of the metallized vias showed that the 10, 20, and 30 μm vias were not opened by any combination of the five process conditions.

Table 5.2: Fractional factorial experimental data for ablated dielectric thickness.

Laser Fluence	**Shot Frequency**	**Number of Pulses**	**Vertical Debris Removal**	**Horizontal Debris Removal**	**Ablated Thickness (μm)**
200	150	1000	Up	Side	25.05
100	100	500	Down	Side	15.28
200	100	1000	Up	Middle	25.00
100	100	500	Up	Middle	14.94
100	150	1000	Down	Side	24.89
200	100	1000	Down	Side	25.00
200	150	500	Down	Side	25.00
200	150	1000	Down	Middle	25.03
100	100	1000	Down	Middle	25.01
200	150	500	Up	Middle	24.95
200	100	500	Up	Side	24.85
200	100	500	Down	Middle	24.94
100	150	1000	Up	Middle	24.90
100	150	500	Down	Middle	15.06
100	100	1000	Up	Side	25.00
100	150	500	Up	Side	14.22

Table 5.3: Fractional factorial experimental data for top via diameter.

Laser Fluence	Shot Frequency	Number of Pulses	Vertical Debris Removal	Horizontal Debris Removal	Top Via Diameter (mm)		
					30	40	50
175	100	1000	Down	Middle	32.07	42.56	52.80
200	150	1000	Up	Side	32.12	42.06	51.67
200	150	500	Down	Side	37.34	46.37	55.95
175	150	1000	Down	Side	35.17	45.49	55.84
175	100	500	Up	Middle	30.06	40.02	49.88
175	150	1000	Up	Middle	30.51	40.30	50.81
200	100	500	Down	Middle	35.83	43.49	54.41
175	100	500	Down	Side	31.72	42.74	51.74
175	100	1000	Up	Side	30.56	40.89	51.04
200	100	500	Up	Side	31.71	41.59	52.05
200	100	1000	Down	Side	40.03	48.99	59.23
200	150	1000	Down	Middle	37.81	46.85	56.99
175	150	500	Down	Middle	29.58	39.06	49.54
200	100	1000	Up	Middle	32.35	42.15	52.30
175	150	500	Up	Side	30.35	40.39	50.41
200	150	500	Up	Middle	31.45	40.92	51.64

Table 5.4: Fractional factorial experimental data for via wall angle.

Laser Fluence	Shot Frequency	Number of Pulses	Vertical Debris Removal	Horizontal Debris Removal	Via Wall Angle (degrees)		
					30 µm	40 µm	50 µm
175	100	1000	Down	Middle	63.09	60.68	59.16
200	150	1000	Up	Side	68.33	62.50	61.57
200	150	500	Down	Side	59.93	59.89	58.85
175	150	1000	Down	Side	62.17	59.94	59.06
175	100	500	Up	Middle	64.41	62.70	60.06
175	150	1000	Up	Middle	65.53	63.17	60.86
200	100	500	Down	Middle	61.61	62.56	60.34
175	100	500	Down	Side	61.76	59.73	58.18
175	100	1000	Up	Side	65.62	63.16	61.39
200	100	500	Up	Side	64.72	63.50	62.08
200	100	1000	Down	Side	59.98	58.65	58.87
200	150	1000	Down	Middle	61.84	60.44	59.70
175	150	500	Down	Middle	65.91	63.81	60.38
200	100	1000	Up	Middle	64.90	63.29	61.25
175	150	500	Up	Side	65.49	62.66	61.22
200	150	500	Up	Middle	65.94	63.38	62.52

Table 5.5: Fractional factorial experimental data for via resistance.

Laser Fluence	Shot Frequency	Number of Pulses	Vertical Debris Removal	Horizontal Debris Removal	Via Resistance (ohm)	
					40 μm	50 μm
175	100	1000	Down	Middle	37.01	4.18
200	150	1000	Up	Side	806.68	282.55
200	150	500	Down	Side	317.67	5.41
175	150	1000	Down	Side	73.09	156.63
175	100	500	Up	Middle	9012.03	3148.66
175	150	1000	Up	Middle	197.25	3.91
200	100	500	Down	Middle	1297.78	516.88
175	100	500	Down	Side	177.38	4.66
175	100	1000	Up	Side	744.73	123.27
200	100	500	Up	Side	1787.04	653.99
200	100	1000	Down	Side	33.73	10.09
200	150	1000	Down	Middle	55.45	73.98
175	150	500	Down	Middle	6501.52	1202.41
200	100	1000	Up	Middle	129.59	40.62
175	150	500	Up	Side	1611.53	467.41
200	150	500	Up	Middle	4638.36	1317.62

5.1.2 Statistical Analysis

After the collection of data from the experiments, RS/Discover® was used to determine which input factors were statistically significant (p-value < 0.05) in their affect on the laser ablation responses. The results showed that laser fluence and the number of pulses significantly affected the ablated thickness of the dielectric, as shown in Table 5.6. This finding supports earlier studies, such as [7] and [11], that indicated that these two factors dominantly affect the ablated dielectric thickness. There were also several significant two-term interactions affecting the ablated thickness. These interactions occurred between fluence and frequency, fluence and number of pulses, and frequency and horizontal position of the debris removal system. Since Kapton® E polyimide strongly absorbs laser energy at the operating wavelength, increasing the fluence and

number of pulses results in the breaking of molecular bonds and (i.e., more polyimide ablated). As time progresses, more debris byproducts are generated; therefore, moving the position of the debris removal system closer to the ablation site to determine a clear path for laser beam becomes increasingly important.

Table 5.6: Significance of input factors for dielectric thickness.

Input Factors	**Ablated Thickness (*p*-value)**
Laser Fluence (E)	**0.0000**
Shot Frequency (F)	0.2999
Number of Pulses (P)	**0.0000**
Vertical Position of Debris Removal (V)	0.0514
Horizontal Position of Debris Removal (H)	0.5687
E x F	**0.0429**
E x P	**0.0000**
F x H	**0.0063**

All of the input factors except shot frequency were found to be statistically significant in affecting the top size of the vias, as shown in Table 5.7. In addition, several two-term interactions were also found to be significant. The same significant interactions occurred for all via sizes. They included fluence and vertical position of the debris removal system, number of pulses and vertical position of the debris removal system, and vertical and horizontal position of the debris removal system. The breaking of bonds on the surface of polyimide defined the geometry of the top via diameter. Due to beam divergence and possible reflections from the surface, the total energy density varied with via size.

Table 5.7: Significance of input factors for top via diameter.

Input Factors	*p*-value		
	Top Via Diameter		
	30 μm	40 μm	50 μm
Laser Fluence (E)	**0.0000**	**0.0000**	**0.0000**
Shot Frequency (F)	1.0000	0.8656	0.9211
Number of Pulses (P)	**0.0000**	**0.0000**	**0.0000**
Vertical Position of Debris Removal (V)	**0.0000**	**0.0000**	**0.0001**
Horizontal Position of Debris Removal (H)	**0.0002**	**0.0000**	**0.0005**
E x V	**0.0000**	**0.0000**	**0.0002**
P x V	**0.0003**	**0.0001**	**0.0002**
V x H	**0.0003**	**0.0001**	**0.0011**

As for the via wall angle, the data showed that the vertical position of the debris removal system was statistically significant, but the number of pulses was not for all via sizes, shown in Table 5.8. The interaction between the vertical and horizontal position of the debris removal system was found to significantly affect wall angle for all via sizes. The analysis also showed that for smaller feature sizes, more factors affected the via wall angle. However, the beam profile and effectiveness of the debris removal system were apparently the most critical determining factors.

As for the 40 and 50 μm via resistance, results indicated that both number of pulses and horizontal position of the debris removal system, as well as their two-factor interaction significantly affected the 40 and 50 μm via resistance, as shown in Table 5.9. There is also some evidence that the vertical position of the debris removal system may be significant as well. The resistance measurement largely depended on how free via holes were from debris. While open vias were created, increasing the number of pulses aided the debris removal process by ablating the debris itself. The position of the debris

removal system to the ablation site was also important in reducing the possibility that debris re-deposited inside the hole.

Table 5.8: Significance of input factors for via wall angle.

Input Factors	*p*-value		
	Via Wall Angle		
	30 μm	40 μm	50 μm
Laser Fluence (E)	0.0905	0.668	0.0587
Shot Frequency (F)	**0.0312**	0.692	0.2403
Number of Pulses (P)	0.662	0.073	0.4519
Vertical Position of Debris Removal (V)	**0.0000**	**0.0002**	**0.0000**
Horizontal Position of Debris Removal (H)	0.1748	**0.0167**	0.2084
E x V	**0.0068**	0.358	0.214
P x V	0.112	0.055	0.951
V x H	**0.0082**	**0.0349**	**0.0225**

Table 5.9: Significance of input factors for via resistance.

Input Factors	*p*-value	
	Via Resistance	
	40 μm	50 μm
Laser Fluence (E)	0.180	0.271
Shot Frequency (F)	0.892	0.631
Number of Pulses (P)	**0.005**	**0.006**
Vertical Position of Debris Removal (V)	0.127	0.060
Horizontal Position of Debris Removal (H)	**0.033**	**0.037**
P x H	**0.017**	**0.017**

5.2 Neural Network Modeling

Following the collection of the experimental data, feed-forward neural networks were trained using the error back-propagation algorithm to model the average values of the responses. The learning rate, η, and the momentum constant, α, selected were 0.01 and 0, respectively. With these values, all NN models converged quickly and did not oscillate. The inputs to the NN models were the significant factors found from the screening experiment, while, the outputs were the microvia characteristics. One neural network model was trained and tested for each via size for a particular response, as well as for a combination of all responses. Although the individual response models elucidate the conditions that impact a given response, the adjustments required to optimize these conditions for all responses simultaneously are often conflicting. The combined model, therefore, has greater practical utility, since all responses are subject to the same set of process conditions. The responses for the combined model were top via diameter, via wall angle, and via resistance (see Figure 5.2). Seventy-five percent of the data was used for training the networks, and 25% was used for testing.

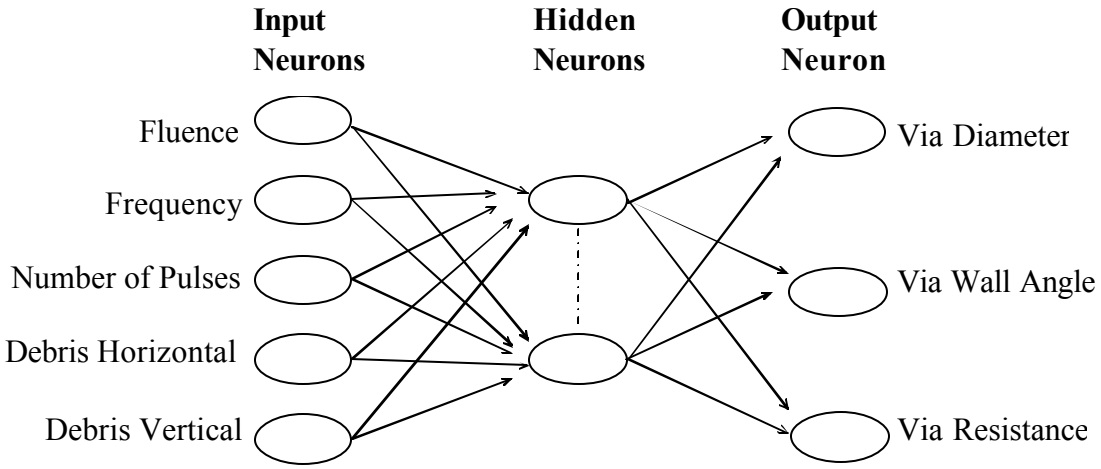

Figure 5.2. Combined neural network model.

5.2.1 Results and Discussion

The results are shown in Table 5.10. The *x*-*y*-*z* values of neural structure in this table refer to the number of neurons in the input, hidden, and output layers, respectively. In the case of the individual models, the prediction error for nearly all responses, with the exception of ablated thickness and via resistance, was less than 5%. The prediction error for the average value of the ablated thickness was 5.5%, whereas that of via resistance was less than 15%. Although only two or three of the five experimental factors were statistically significant in predicting via resistance, all five factors were utilized for subsequent neural network modeling. The reason for this decision was that all five factors were statistically significant in their effects on the other laser ablation responses, including the ablated dielectric thickness, via diameter, and via wall angle.

Table 5.10: Prediction error for neural network modeling of excimer laser ablation.

Neural Network Type	**Microvia Responses**		**Neural Network Structure**	**Average Percentage Errors for Test Data**		
Individual Model	Ablated Dielectric Thickness		5-2-1	5.4974		
	Top Via Diameter (V)	30 μm	4-3-1	2.1454		
		40 μm	4-2-1	1.5724		
		50 μm	4-6-1	3.8840		
	Via Wall Angle (W)	30 μm	4-6-1	4.0468		
		40 μm	4-5-1	1.9602		
		50 μm	4-6-1	1.5378		
	Via Resistance (R)	40 μm	5-5-1	14.6751		
		50 μm	5-4-1	14.4597		
				V	W	R
Combined Model	VWR	40 μm	5-6-3	5.7240	1.9905	13.038
		50 μm	5-5-3	3.3930	1.5307	14.352

Initial modeling results of via resistance were inadequate, so a logarithmic transformation of the resistance data was performed. Data transformations such as this are widely used in cases where there is a vast disparity in the scale of the data being modeled [39] [60]. In this case, the logarithmic data transformation was used to reduce the range of the resistance data prior to neural network training. The networks trained on the transformed data exhibited a much-improved prediction error over those trained on the raw resistance data (<15% versus >200% before the logarithmic transformation).

5.2.2 Three Dimension Contour Plots

Using the neural network models, the interrelationships between the process set points and responses can be graphically illustrated by 3-D contour plots. A few examples of such relationships are shown in Figures 5.3 – 5.9. Figure 5.3 illustrates the impact of laser fluence and number of pulses on the ablated dielectric thickness, with shot frequency held at its mid-range value and the vertical and horizontal positions of the debris removal system set at "up" and "side," respectively. Both fluence and number of pulses have a strong positive correlation with the ablated thickness. The graph shows a plateau because the extremes of both input conditions are sufficient to ablate through the dielectric. One important conclusion that can be drawn from this plot is that ablate through 25 μm of polyimide requires a total energy density of approximately 100 J/cm^2.

Figure 5.4 shows the effects of laser fluence and number of pulses on 30 μm vias, with the vertical and horizontal position of the debris removal system set at "up" and "middle," respectively. The 30 μm vias can be sufficiently ablated with fluence in the range of 175 – 183 mJ/cm^2/pulse and 500 – 620 pulses. Figure 5.5 shows a similar plot

for the 40 μm vias, with the vertical and horizontal position of the debris removal system set at "down" and "middle," respectively. For this via size, it appears that fluence should be kept in the range of 177 – 182 mJ/cm^2/pulse and the number of pulses in the range of 540 – 640 to achieve successful ablation. As total energy density increases, the via diameter for both cases increases due to beam divergence and potential reflections from the polyimide surface.

Figure 5.6 illustrates the variation of wall angle for 30 μm vias with laser fluence and shot frequency, with the vertical and horizontal position of the debris removal system set at "down" and "side," respectively. Steeper wall angles can be achieved with fluence in the range of 175 – 181 mJ/cm^2/pulse and frequency in the range of 144 – 150 Hz. As frequency increases, more debris is generated inside the vias. Due to the smaller size of these vias, the debris is less capable of escaping, resulting in absorption of laser energy by the debris. The absorbed energy is released in horizontal direction (parallel to the substrate), resulting in an increase of via wall angle. In other words, the absorbed energy inside the via increases the temperature significantly compared to that near the surface, resulting in more ablation of the debris and the polyimide in the horizontal direction [28]. As the energy increases, the top diameter increases faster than the bottom diameter, resulting in a decreased wall angle. Figure 5.7 shows a similar plot for 50 μm vias, with the vertical and horizontal position of the debris removal system set at "up" and "side," respectively. For these vias, steeper wall angles can be fabricated with laser fluence in the range of 180 – 188 mJ/cm^2/pulse and shot frequency in the range of 128 – 140 Hz. Since the via size is larger, the wall angle does not vary as much.

Figure 5.8 illustrates the effect of laser fluence and number of pulses on 40 µm via resistance, with shot frequency held at its mid-range value and the vertical and horizontal positions of the debris removal system set at "up" and "middle," respectively. Low resistance (i.e., little debris remaining inside the via) can be achieved with fluence in the range of 195 – 200 mJ/cm^2/pulse and 940 – 1000 pulses. Figure 5.9 shows a similar plot to that of Figure 5.8 for the 50 µm via resistance. For this via size, fluence should be kept in the range of 175 – 180 mJ/cm^2/pulse and the number of pulses in the range of 940 – 1000 to result in low resistance. When total energy density increases, the via resistance tends to decrease for both cases because the ablation of the debris inside results in cleaner vias. In the case of the 50 µm via, the debris has a greater possibility of re-deposition inside of the hole because of the larger via size.

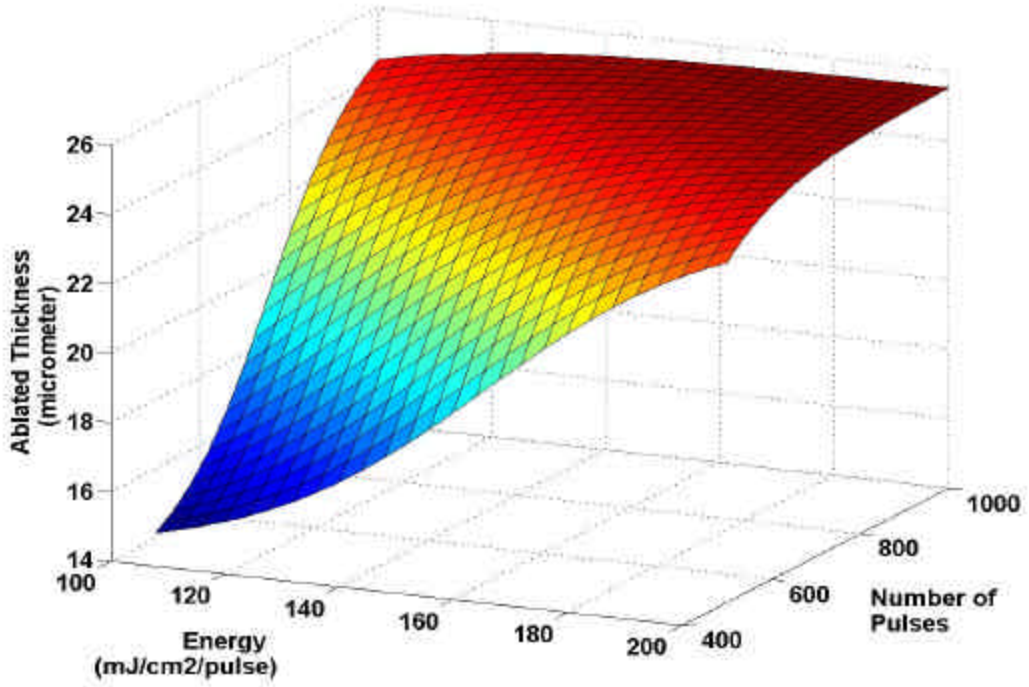

Figure 5.3. Effect of laser fluence and number of pulses on ablated dielectric thickness.

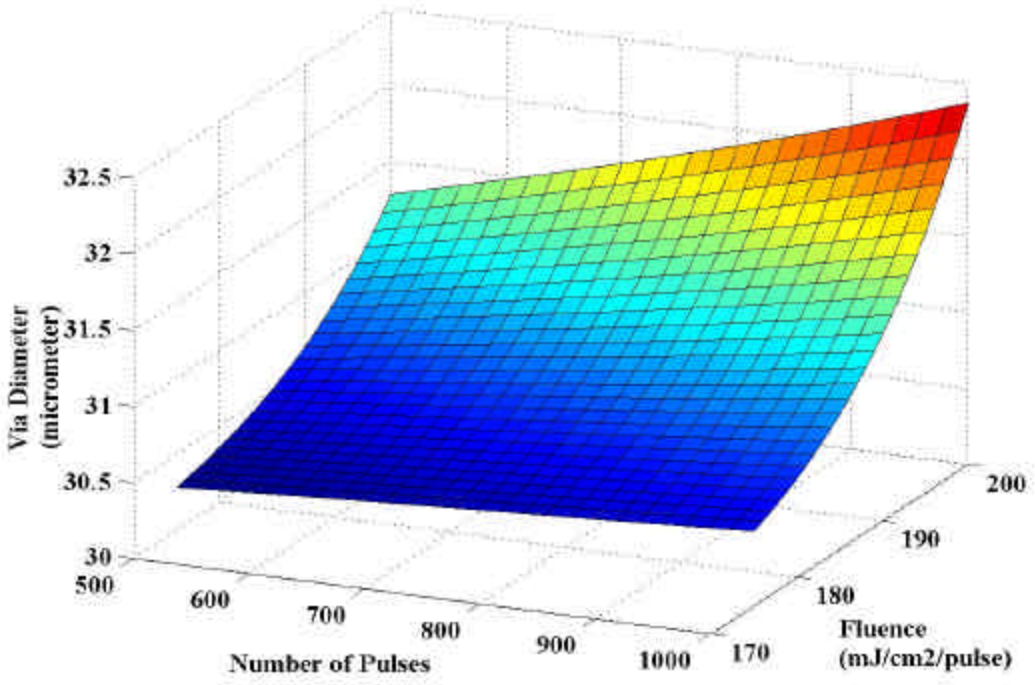

Figure 5.4. Effect of laser fluence and number of pulses on 30 µm via diameter.

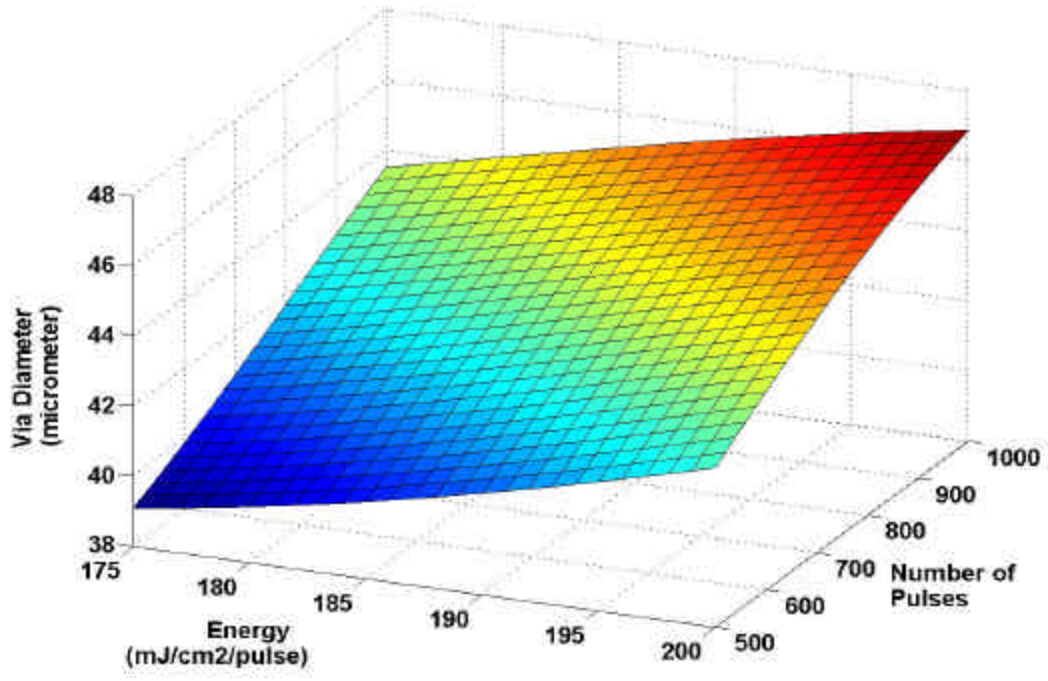

Figure 5.5. Effect of laser fluence and number of pulses on 40 µm via diameter.

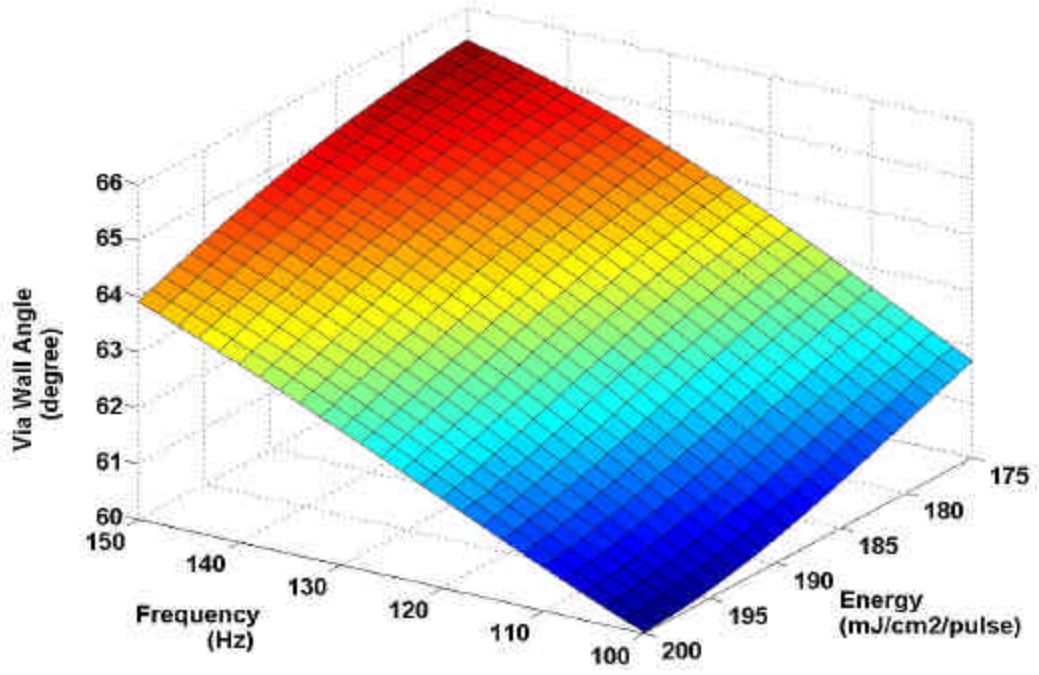

Figure 5.6. Effect of laser fluence and shot frequency on wall angle for 30 µm vias.

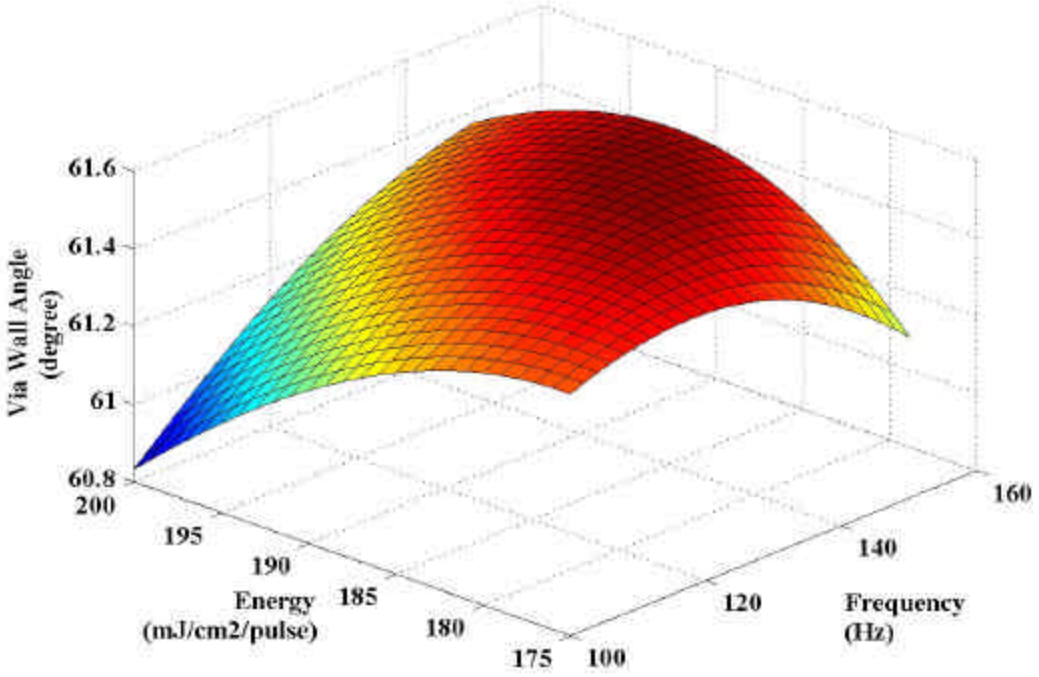

Figure 5.7. Effect of laser fluence and shot frequency on wall angle for 50 µm vias.

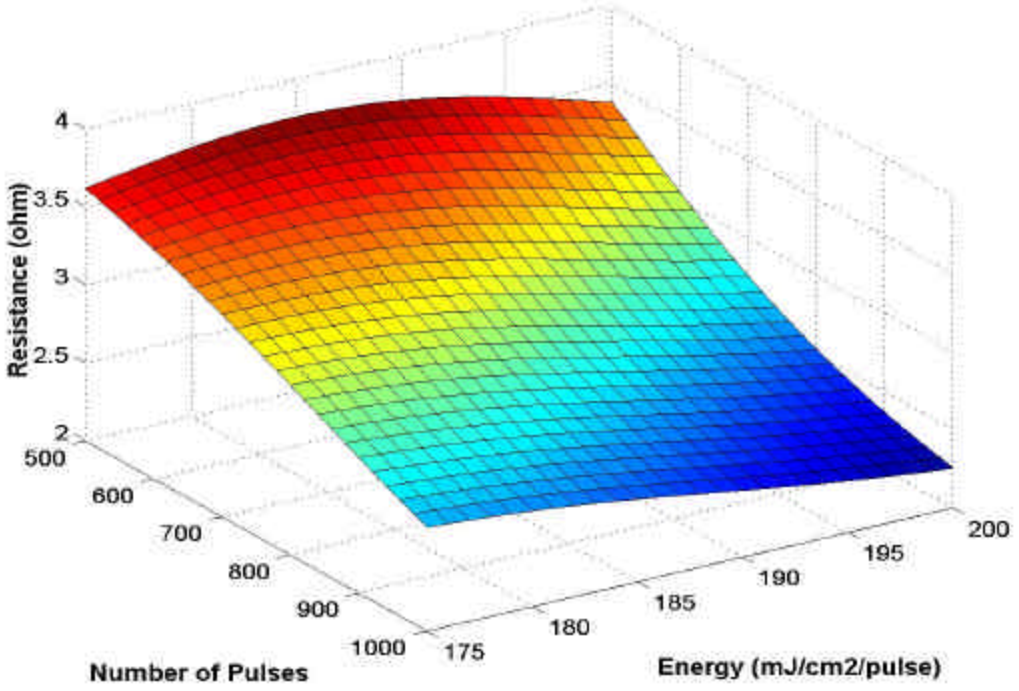

Figure 5.8. Effect of laser fluence and number of pulses on 40 µm via resistance.

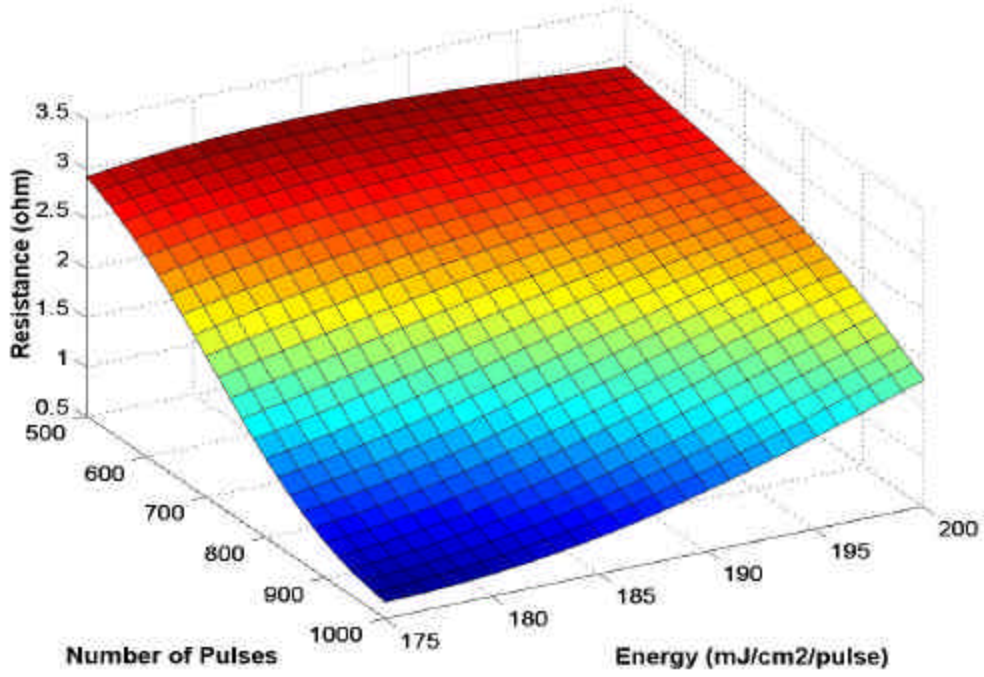

Figure 5.9. Effect of laser fluence and number of pulses on 50 µm via resistance.

5.3 Sensitivity Analysis

The artificial neural network (NN) technique has been utilized to model the laser ablation process used in microvia fabrication. The effect of variation in the NN inputs was subsequently evaluated by means of sensitivity analysis designed to quantify the variation in process responses for incremental changes in process conditions. The sensitivity of one output response with respect an input variable is found by computing the partial derivative of the response with respect to the input of interest while holding the other inputs constant. In other words,

$$\frac{\partial f}{dx_i} \cong \left. \frac{f(x + \Delta x_i) - f(x)}{\Delta x_i} \right|_{\Delta x_i \to 0} \tag{5.1}$$

where f is the functional relationship encoded in the NN model, $\boldsymbol{x}$ is vector of input parameters and $?\boldsymbol{x}_i$ is an incremental change in one of the elements of $\boldsymbol{x}$.

In the modeling of the laser ablation process, two of the five input parameters – namely, the vertical and horizontal positions of the debris removal system in the laser tool - are quantitative factors with two levels. Therefore, the sensitivity analysis for the process responses was grouped based on these two factors. The analysis was performed at the mean value of the range of deviation for each input parameter and making 10% changes in that input. The resulting sensitivity was then normalized for the sake of comparison.

Sensitivity analysis was performed on the neural network (NN) models for individual ablation responses to investigate the impact of varying process inputs on each process response (i.e., ablated dielectric thickness, top via diameter, via wall angle, and via resistance). The NN model of ablated Kapton® E polyimide thickness is most sensitive to

both the laser fluence and number of pulses (see Figure 5.10), which is consistent from the viewpoint of the statistical significance of these parameters. Since polyimide strongly absorbs laser energy at the 308 nm wavelength, increasing the fluence and number of pulses results in the breaking of molecular bonds (i.e., more polyimide ablated). More debris byproducts are generated as time progresses, and it appears that the "up" and "side" position of the debris removal system creates a clearer path for the laser beam to ablate the dielectric than the other positions.

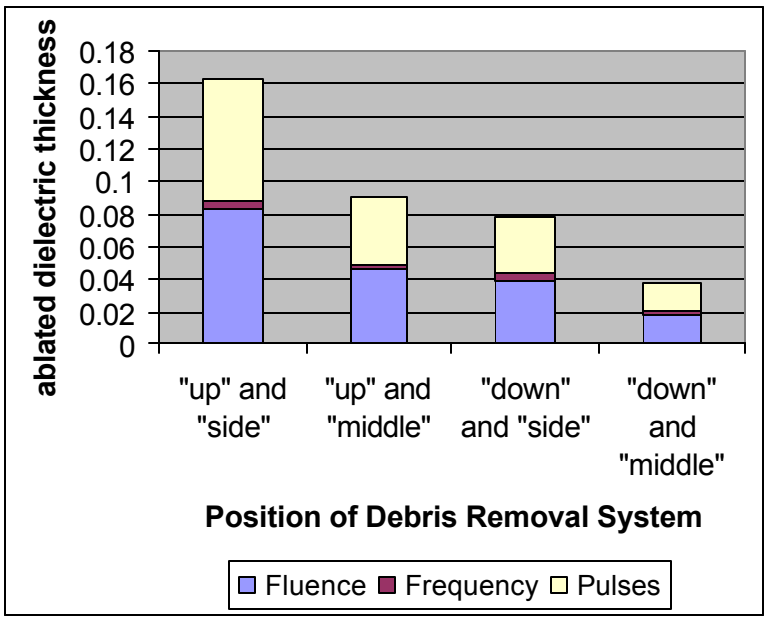

Figure 5.10. Sensitivity of ablated dielectric thickness (normalized)

The geometry of the top via diameter was defined by breaking bonds on the polyimide surface. Figure 5.11 shows the sensitivity of the NN models for 30 μm and 40 μm top via diameters for a constant shot frequency. (Shot frequency was not statistically significant in affecting the top via for all diameter sizes). Based on this figure, top via diameter is most sensitive to fluence. Since the laser energy used in this study was guaranteed to cause ablation of the material, the top via diameter was primarily

determined by the energy contained in each pulse. Due to beam divergence and possible reflections from the surface, the total energy density (laser fluence multiplied by the number of pulses) varied with via size. It appears, from Figure 5.11(a), that the 30 µm via diameter increases faster with the position of the debris removal system "up" and "side". For the 40 µm via diameter, "down" and "middle" position has the largest effect on via size.

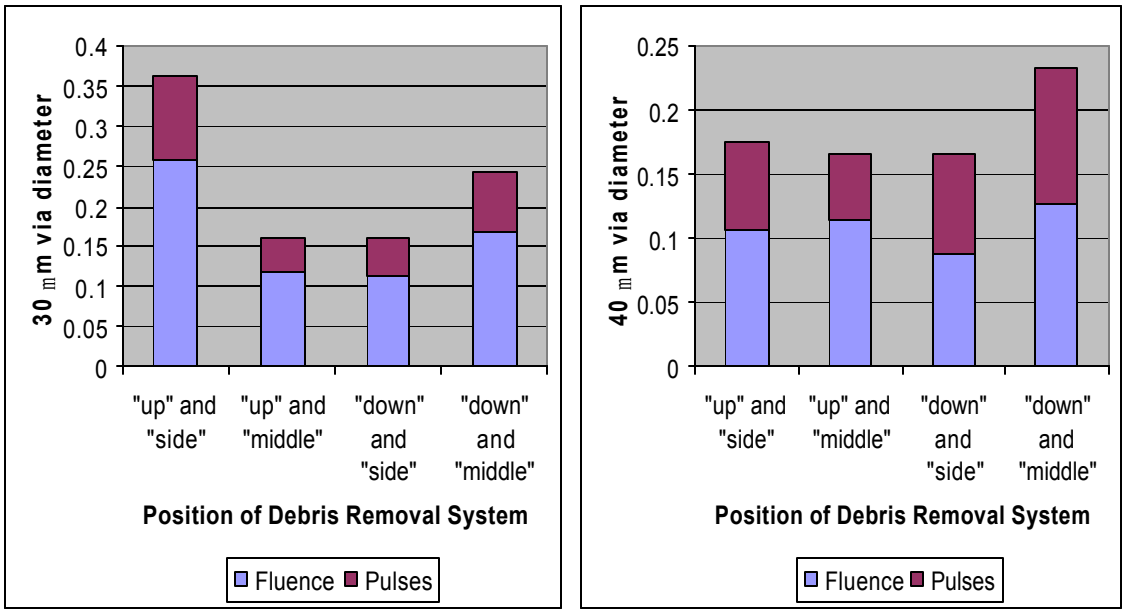

(a) (b)

Figure 5.11. Sensitivity of (a) 30 µm, and (b) 40 µm top via diameter (normalized)

The interaction between the vertical and horizontal position of the debris removal system was found to significantly affect wall angle for all via sizes. However, the beam profile and effectiveness of the debris removal system were apparently the most critical determining factors (as shown in Figure 5.12 for the 30 µm and 50 µm vias). Due to the small size of these vias, debris is less capable of escaping, resulting in possible absorption

of laser energy by the debris. The absorbed energy is released in the horizontal direction (parallel to the substrate), resulting in an increase of via wall angle.

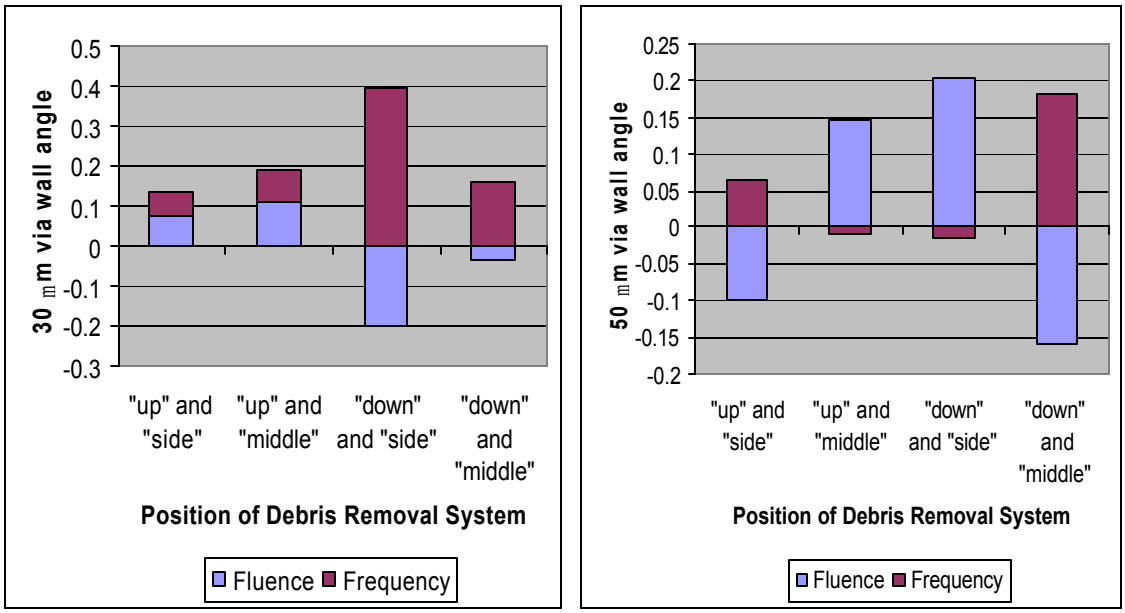

(a) (b)

Figure 5.12. Sensitivity of (a) 30 μm, and (b) 50 μm via wall angle (normalized)

The resistance measurement largely depended on the cleanliness of the vias. While open vias were created, increasing the number of pulses (the most significant factor affecting this response) aided the debris removal process by ablating the debris itself. The relative position of the debris removal system and the ablation site was also important in aiding the removal of debris. Figure 5.13 shows the sensitivity of 40 μm and 50 μm via resistance. When total energy density increases, the via resistance tends to decrease for both cases because the ablation of the debris inside results in cleaner vias. In the case of the 50 μm via, debris has a greater possibility of re-deposition inside of the hole because of the larger via size, resulting in increased resistance.

(a) (b)

Figure 5.13. Sensitivity of (a) 40 µm, and (b) 50 µm via resistance (normalized)

5.4 Summary

In this chapter, microvia formation by excimer laser ablation was characterized and modeled using statistical experimental design and back-propagation neural networks, respectively. Results of neural network modeling indicated the ability of the technique to predict process responses accurately. Three-dimensional surface plots revealed overall trends of microvia responses with respect to laser input parameters. Sensitivity analysis of the networks was performed to quantify the effect of varying process conditions on the responses. In the next chapter, the laser ablation process is optimized using genetic algorithms to identify optimal recipes to yield specific microvia responses. These targets include open vias, specific via diameters and wall angles, and zero via resistance. Experimental verification of the optimized recipes is also conducted.

CHAPTER 6

LASER PROCESS OPTIMIZATION

In this chapter, a systematic method of identifying specific sets of excimer laser process conditions (or "recipes") to achieve desired microvia targets is developed. These desired targets include open vias, specific via diameter, steep wall angle, and low via resistance. In the previous chapter, neural network models of microvia responses were developed. These models represent multidimensional response surfaces that depict the overall trends of microvia response variations with respect to laser input parameters. These response surfaces serve as search spaces for process optimization. Both individual and combined NN models are used in conjunction with genetic algorithms (GAs) [44] to generate optimal recipes. Although the individual response models elucidate the conditions that impact a given response, the adjustments required to optimize these conditions for all responses simultaneously are often conflicting. The combined model, therefore, has greater practical utility, since all responses are subject to the same set of process conditions. The suggested recipes are then used as inputs to the laser tool for verification purposes.

6.1 Genetic Algorithms

Genetic algorithms were first proposed in 1975 [61]. Genetic algorithms are guided stochastic search techniques based on the mechanics of genetics [44] [61-62]. GAs offer several benefits, including the obviation of the need for derivatives in finding the solution (resulting in low probability for GAs getting "trapped" in local minima), the parallel

search of the solution space (as opposed to a point-by-point search), and the manipulation of *potential* solutions (rather than the solutions themselves). Consequently, these algorithms require neither a complete model of the problem nor for the search space to be regularly shaped and differentiable. The only problem-specific requirement is the ability to evaluate the trial solutions based on their relative fitness [62].

The use of GAs in optimizing the laser ablation process is motivated by the need to find a set of process set points for achieving specific target responses. The neural network technique has established the process models that define the relationship between the process set points and responses. GAs are used to obtain the (potentially conflicting) target responses. It has been shown that GAs represent a powerful method for searching the solution space to find optimal recipes in electronic packaging and semiconductor manufacturing applications [63-64].

6.1.1 Creation of Population

Genetic algorithms simulate basic genetic operations found in nature to guide their search through the solution space. The first step in implementing GAs is the creation of a population of trial solutions. Those possible solutions are commonly represented by binary strings (called "chromosomes"), which are to be manipulated by a set of genetic operators. The number of digits assigned to a given parameter determines the numerical accuracy. Multiple parameters are encoded in a single chromosome where sections of the string represent encoded parameters of the solution. Figure 6.1 shows a 3-parameter coding where the first, second, and third parameter are 1 – 8, 0 – 31, and 1 – 14, respectively.

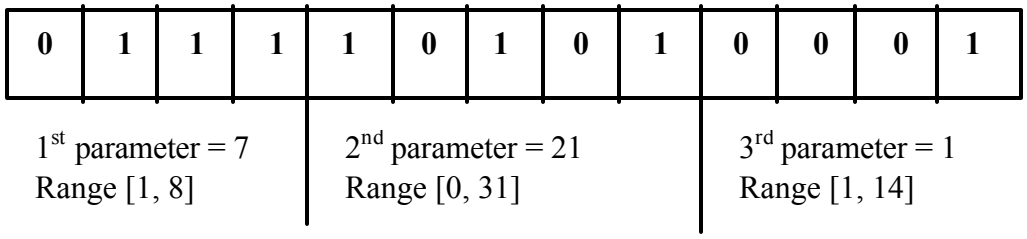

Figure 6.1. Example of multi-parameter coding.

6.1.2 Evaluation and Selection of Individuals

Chromosomes are decoded and evaluated based on how well they solve the problem. This is accomplished by means of a *fitness measure* that is used to allocate reproductive opportunities in such a way that those chromosomes representing a better solution to the problem are given a better chance to generate offspring. In the reproduction process, individuals with high fitness values (i.e., good solutions to the optimization problem under consideration) receive larger number of copies in the new population. In the *elitist roulette wheel* selection method [44], those strings with large fitness values (F_i) are assigned a proportionately higher probability of survival into the next generation. This probability distribution is determined by

$$P_{select\_i} = \frac{F_i}{\sum F} \tag{6.1}$$

An individual whose fitness is n times better than another will potentially produce n times the number of offspring in the subsequent generation. The fitness of each individual of the population is evaluated with respect to the constraints imposed by the problem, considering the desired set points of each parameter. An example of a fitness formula is

$$F = \frac{1}{1 + \sum_{n} \left| K_n (y_d - y_o) \right|} \tag{6.2}$$

where n is the number of responses, K_n's are the weights of the process responses, y_d is the desired process response, and y_o is the process output resulting from the current input parameters. Once the individuals have reproduced, they are stored in a "mating pool" while awaiting the genetic manipulation process. The population propagates through the reproduction and genetic manipulation process, and each generation is increasingly capable of solving the problem.

6.1.3 Crossover and Mutation

The genetic manipulation process combines chromosomes from one generation and produces new chromosomes that maintain the best features of the previous generation. The most common methods for such manipulation are *crossover* and *mutation*. The crossover operator takes two randomly selected chromosomes and interchanges part of their genetic information to produce two new chromosomes, as shown in Figure 6.2. The crossover point is randomly chosen, and portions of the parent strings are swapped to produce new offspring based upon a specified crossover probability. Mutation is motivated by the possibility that the initially defined population does not contain all the information necessary to solve the problem. This operation is implemented by randomly changing a fixed number of bits every generation based upon a specified mutation probability. Figure 6.3 shows an example of mutation. Typical values of the probabilities of crossover and mutation range from 0.6 to 0.9 and 0.001 to 0.03, respectively. Higher mutation and crossover rates disrupt good "potential solutions" more often, and for

smaller populations, sampling errors tend to wash out the predictions. For this reason, the greater the mutation and crossover rates and the smaller the population size, the less frequently predicted solutions are confirmed.

GAs thus progress through a cycle of four stages: 1) creation of a "population" of strings; 2) evaluation of each string; 3) selection of "best" strings; and 4) genetic manipulation to create a new population of strings.

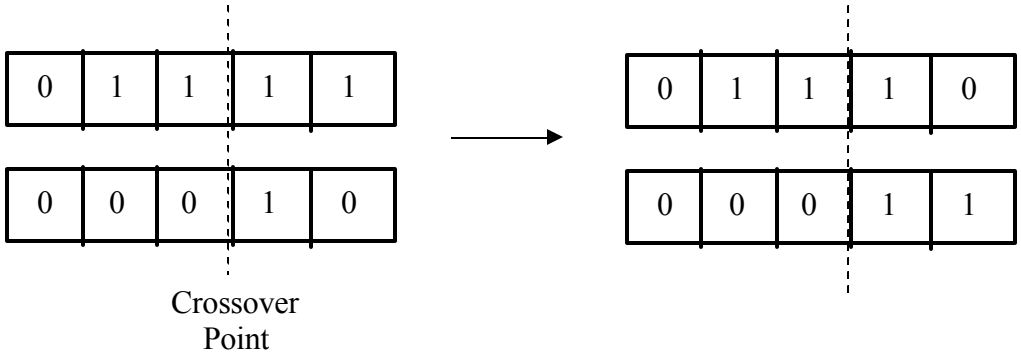

Figure 6.2. Crossover of two parent chromosomes resulting in two offspring.

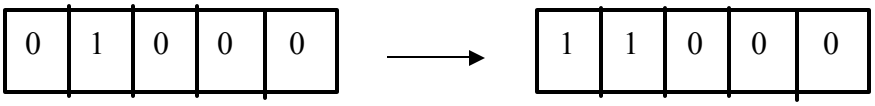

Figure 6.3. A chromosome experiencing mutation.

6.1.4 Neuro-Genetic Implementation

In this study, GAs were coded in ObOrNNS, which allows the user to load a trained neural network model [58]. The model was used as an evaluation function. Genetic algorithms produce laser process inputs from the neural network model, which calculates the predicted microvia responses. The output is fed back into the GAs until a suitable stopping criterion is achieved, such as a maximum number of generations or a user-

defined minimum error. The weighing coefficients for the desired responses in (6.2) must also be determined depending upon the application and the order of importance of the responses. Figure 6.4 illustrates the process optimization method.

6.2 Optimal Recipe Synthesis

Genetic algorithms were used to find optimal set points that give the desired output from all NN models. The selected probabilities of crossover and mutation were 0.65 and 0.01, respectively. An average population size of 200 was used for each generation, and generations evolved through 200 iterations. The quantitative input factors (i.e, laser fluence, shot frequency, and number of pulses) were coded to a 10-bit string, while the qualitative factors were encoded in a single bit. Thus, 32-bit chromosomes were required to find the desired value(s) for the individual response models (ablated thickness and via resistance), as well as the combined response model (top via diameter, via wall angle, and via resistance) because all five inputs were significant in affecting at least one response. On the other hand, 22-bit chromosomes were sufficient to find the desired value of the individual response model for top via diameter and via wall angle, since only four inputs (two quantitative and two qualitative factors) were significant for these responses.

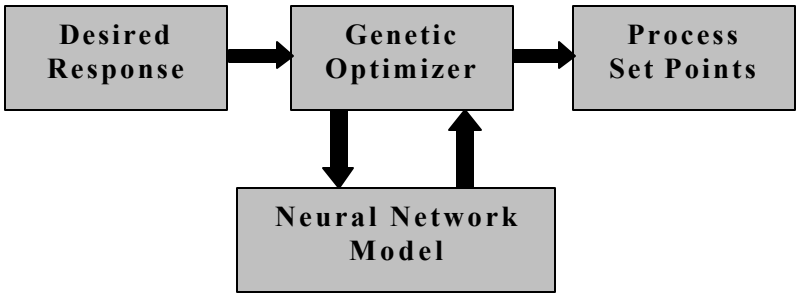

Figure 6.4. Process optimization procedure.

6.2.1 Optimization Results and Discussion

In this research, the desired ablated thickness, top via diameter, and via resistance were 25 μm, 30/40/50 μm, and 0 Ω, respectively. The weight coefficients in (6.2) were chosen based on consultation with a microelectronics packaging expert [65]. The more important the response is in the packaging industry, the more weight was attributed to the response. The desired outputs and weight coefficients are listed in Table 6.1. Tables 6.2 – 6.3 show the recipes generated by the algorithms and the resulting outputs.

Table 6.1: Desired outputs and weight coefficients
for recipe synthesis optimization
(combined response model).

	Desired Output	**Weight Coefficient**	
		40 μm Vias	**50 μm Vias**
Top Via Diameter	40 or 50 μm	8	3
Via Wall Angle	75°	3	2
Via Resistance	0 Ω	20	15

The genetic algorithms were not able to find the optimal process recipe to simultaneously satisfy the desired via wall angle and via resistance. Discrepancies between the desired and simulated outputs stem from any combination of possible sources of error, including equipment error, measurement error, fabrication error, and model error. Equipment error refers to issues in repeatability and process shifts. Measurement error includes human error and inaccuracies in the measurement tools. Fabrication error refers to less than optimum process conditions for each fabrication step. Model error accounts for less than ideal process model developed.

Table 6.2: Generated recipes and simulated results (individual model).

Model Name	Model Type	Laser Fluence (mJ/cm2 /pulse)	Shot Frequency (Hz)	Number of Pulses	Vertical Position of Debris Removal	Horizontal Position of Debris Removal	Simulated Output	Desired Output
Ablated Thickness		151.9	128	860	Up	Side	25.0 μm	25.0 μm
Top Via Diameter	30 μm	176.6	-	521	Down	Middle	30.0 μm	30.0 μm
	40 μm	178.9	-	645	Up	Middle	40.0 μm	40.0 μm
	50 μm	180.2	-	624	Up	Middle	50.0 μm	50.0 μm
Via Wall Angle	30 μm	200.0	150	-	Up	Side	68.3°	75.0°
	40 μm	175.0	141	-	Down	Middle	63.8°	75.0°
	50 μm	184.5	135	-	Up	Side	61.6°	75.0°
Via Resistance	40 μm	182.5	100	1000	Down	Middle	30.2 Ω	0 Ω
	50 μm	176.0	149	991	Down	Middle	1.78 Ω	0 Ω

Table 6.3: Generated recipes and simulated results (combined model).

Model Name	Laser Fluence (mJ/cm2/ pulse)	Shot Frequency (Hz)	Number of Pulses	Vertical Position of Debris Removal	Horizontal Position of Debris Removal	Simulated Output			Desired Output		
40 μm	176.6	100	999	Down	Middle	42.4 μm	60.4°	37 Ω	40.0 μm	75°	0 Ω
50 μm	178.8	146	992	Up	Middle	50.9 μm	60.8°	4.8 Ω	50.0 μm	75°	0 Ω

6.2.2 Experimental Verification

After the process set points were synthesized, experimental verification of the optimized recipes was conducted. Based on the verification results, the error between the average measurements and predicted values derived from the NN/GA-generated recipes was less than 4% for the individual model of ablated dielectric thickness, top via diameter, and via wall angle. As for via resistance, there was a difference in magnitude of a few hundred ohms between experimental results and predicted values. The differences in resistance can be attributed to the behavioral inconsistency of the debris/residue resulting from the ablation and the sensitivity of the materials used in the fabrication process, including metal deposition, metal etching, and the post-bake process [66].

The prediction error for the combined response model was less than 7% for the top via diameter and via wall angle responses. A similar discrepancy was found for the via resistance response. Despite the discrepancies in via resistance modeling, the NN/GA approach adequately provided suitable process recipes. Table 6.4 shows the deviation between the experimental results and the NN/GA model. The improvement achieved from the non-optimized recipes (i.e., those recipes used during the designed experiment) and the optimized recipes is as large as 40% for the ablated thickness response, 30% for top via diameter (individual and combined models), 9% for via wall angle (individual and combined models), and >100% for via resistance (individual and combined models). These improvements clearly demonstrate the effectiveness of the genetic optimization approach.

Table 6.4: Deviation between model and experiment.

Model Name			**Deviation of Model from Experiment**		
Individual Model	Ablated Thickness		1.32%		
	Top Via Diameter	30 μm	1.92%		
		40 μm	2.22%		
		50 μm	0.90%		
	Via Wall Angle	30 μm	3.35%		
		40 μm	0.33%		
		50 μm	1.36%		
	Via Resistance	40 μm	400 Ω		
		50 μm	60 Ω		
			Top Via Diameter	Via Wall Angle	Via Resistance
Combined Model	40 μm		6.58%	1.88%	380 Ω
	50 μm		0.76%	1.04%	150 Ω

6.3 Summary

In this chapter, microvia formation using excimer laser ablation was optimized using genetic algorithms in conjunction with the neural network models of the ablation to synthesize recipes to yield specific target responses. The targets included open vias, a specific via diameter, steep via wall angles, and low via resistance. Experimental verification demonstrated that the optimized recipes improved ablation results by as much as 40% for film thickness, 30% for the via diameter, 9% for via wall angle, and by more than 100% for via resistance. In the next chapter, run-to-run process failure detection and diagnosis is presented. A systematic methodology using neural networks, Dempster-Shafer theory, and neuro-fuzzy methods for identifying the cause of deviations in microvia responses is described.

CHAPTER 7

PROCESS FAILURE DETECTION AND DIAGNOSIS

The formation of microvias in multilayer substrates is critical in microelectronic packaging manufacturing. Such microstructures can be produced efficiently by excimer laser ablation. An excimer laser ablation system has been developed to accommodate the objectives of increasing production yield and lowering manufacturing cost. This tool utilizes the latest developments in the laser optics, beam profiling, active gas lifetime, scanning stage technology, process control, and on-line sensors. However, tool requirements have evolved to a level where the need to offset high capital equipment investment and lower equipment downtime are imminent.

Thus, a major challenge in the use of this tool is to achieve automated failure detection and diagnosis. Since microvia characteristics are process-dependent and the process is tool-dependent, when a process shifts, the characteristics deviate from targets. Although a certain amount of random variability in any process is inevitable, significant process shifts may occur when this variability becomes large. Such shifts beyond an acceptable level often result in deviations in process responses that are unacceptable. These deviations are indications of necessary process adjustments or malfunctions.

In Chapter 5 and 6, the excimer laser ablation process was characterized, modeled, and optimized for microvia formation in polyimide using combinatorial techniques involving statistics, neural networks, and genetic algorithms. In this chapter, an

automated *in-line* run-to-run (R2R) failure diagnosis system using neural networks and Dempster-Shafer (D-S) theory is presented. For the sake of comparison, a neuro-fuzzy logic approach is also applied to achieve the same objective. Both the D-S theory and neuro-fuzzy logic are used to develop an automated inference system – thereby uncovering possible cause(s) of problems in the process and minimizing product loss and overall cost. Promising results are achieved using both inference techniques. A flow chart for this procedure is shown in Figure 7.1.

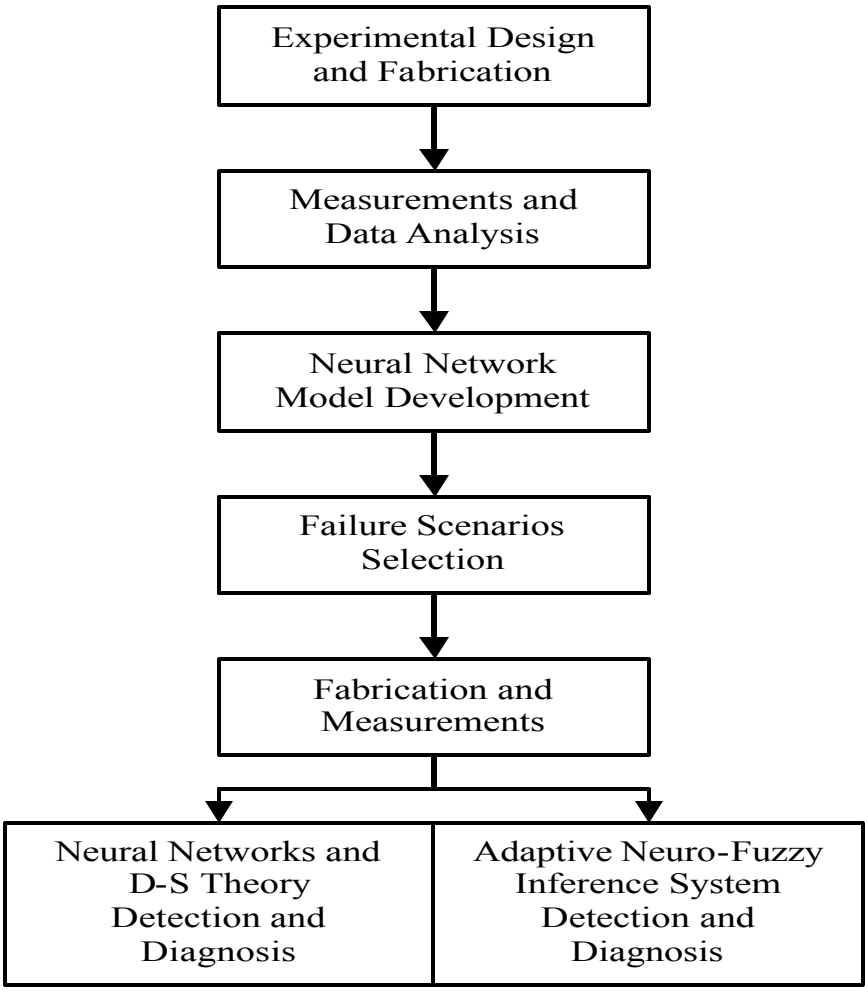

Figure 7.1. Flow chart for failure detection and diagnosis.

7.1 Experimental Design and Data Acquisition

In Chapter 5, laser input parameters – including laser fluence, shot frequency, number of pulses, and vertical and horizontal positions of the debris removal system – were found to be statistically significant in their effects on dielectric thickness, via diameter, via wall angle, and via resistance. Subsequently, neural network models were built to map the relationships between the inputs and responses selected. The optimal process recipes were then generated for specific target responses in Chapter 6.

In the first effort to detect and diagnose failure in laser ablation, quantitative user-controllable laser input factors were selected. Since the vertical and horizontal positions of the debris removal systems are qualitative factors that do not easily shift during operation, an additional quantitative factor was selected: helium pressure flow (part of the debris removal system). The addition of a new factor required a new screening experiment to determine whether the factor was statistically significant. Meanwhile, the vertical and horizontal positions of the debris removal system were optimally positioned – "down" and "middle", respectively. The positions were selected based on the optimal recipes for the two factors generated by the combined neural network models (i.e., 40 and 50 μm via models) and genetic algorithms. Although the 50 μm combined NN/GA suggested the "up" and "middle" positions for the debris removal system to produce target via diameter, wall angle, and via resistance, as shown in Chapter 6, the algorithms actually also suggested the "down" and "middle" positions as an alternative. The average error between the recipe generated by the NN/GA and the alternative was less than 3%.

7.1.1 Statistical Analysis

The laser input parameters selected in this study included laser fluence (measured in mJ/cm^2/pulse), shot frequency (in Hz), number of pulses, and helium pressure flow (in psi). The first three parameters are characteristics of the laser, while the fourth is part of the debris removal system. The microvia characteristics measured included the top and bottom via diameters, which are used to derive the sidewall angle, and the electrical resistance.

Experimental data used for subsequent process modeling was obtained through a central composite circumscribed (CCC) design [38]. A CCC design consists of a full factorial experiment augmented by axial points at a distance α from the center of the design space (Figure 7.2). The full factorial design was used to determine the significance of laser process input parameters. The other points in the CCC design were used as additional data for subsequent neural network modeling, resulting in a more robust network. The number of experiments required for the CCC design was 31 trials ($2^4 = 16$ trials from the factorial corner points, 8 trials based on the axial points, and 7 replicates at the center of the design). The range of experimentation for the input factors is shown in Table 7.1. The order of the experimental trials was randomized so that the effect of any nuisance factors that might influence the observed responses was minimized. The tool used for experimental design and analysis was the *RS/Discover*® commercial software package. Table 7.2 – 7.3 show the experimental data for the top diameter, wall angle, and resistance for the 40 and 50 μm vias based on the CCC design. In those tables, the grey lines represent the full-factorial design points.

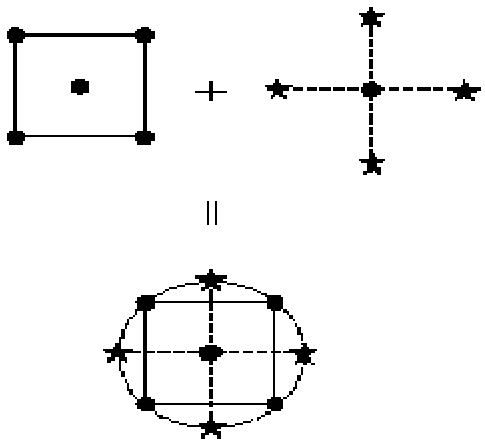

Figure 7.2. CCC Design for two factors.

Table 7.1: Input factors and ranges of experimentation based on central composite circumscribed design.

	Input Factors	**Range**
1	Laser Fluence	162.5 – 212.5 mJ/cm^2/pulse
2	Shot Frequency	75 – 175 Hz
3	Number of Pulses	250 – 1250
4	Helium Pressure Flow	0 – 80 psi

Based on statistical analysis of the experimental data, all input parameters were found to be statistically significant (p-value < 0.05) in affecting at least one microvia response. Table 7.4 gives the p-values for the terms contributing to the responses with the bold-typed values indicating significance at 95% confidence.

Table 7.2: Central composite circumscribed experimental data for 40 μm via.

Laser Fluence	Shot Frequency	Number of Pulses	Helium Pressure Flow	Top Via Diameter (mm)	Via Wall Angle (degrees)	Via Resistance (ohm)
187.5	125	750	40	41.33	60.68	90.73
187.5	125	1250	40	43.08	60.76	108.59
187.5	125	750	40	40.90	60.71	103.22
187.5	125	750	40	41.08	60.55	17.77
200	150	1000	20	44.82	59.56	111.97
187.5	125	750	40	39.89	60.83	1782.68
175	150	500	20	40.11	57.78	10.67
187.5	125	750	80	38.85	60.21	128.34
175	100	500	60	37.79	58.48	5701.66
187.5	75	750	40	38.92	59.96	32.18
187.5	125	250	40	38.92	52.10	1000000
187.5	125	750	40	40.52	60.26	1904.03
212.5	125	750	40	41.12	61.86	29.47
187.5	125	750	40	41.06	60.72	36.27
175	150	1000	60	39.27	60.33	44.17
175	150	500	60	37.61	59.31	170416.67
187.5	175	750	40	41.90	60.89	38026.53
200	100	1000	60	40.44	60.67	434.06
200	150	500	20	41.59	60.11	4583.72
162.5	125	750	40	39.73	58.27	60690
175	150	1000	20	38.37	60.23	584.80
200	150	1000	60	40.04	62.64	633.76
200	100	1000	20	40.12	60.97	6817.44
200	150	500	60	39.45	61.03	375.05
175	100	1000	60	38.75	60.00	1114.73
175	100	1000	20	38.63	59.79	9153.55
200	100	500	60	39.24	60.42	1450.70
187.5	125	750	40	43.54	59.16	211.83
187.5	125	750	0	38.72	61.55	179.92
175	100	500	20	37.14	58.72	358338.33
200	100	500	20	39.43	60.69	5753.33

Table 7.3: Central composite circumscribed experimental data for 50 μm via.

Laser Fluence	Shot Frequency	Number of Pulses	Helium Pressure Flow	Top Via Diameter (mm)	Via Wall Angle (degrees)	Via Resistance (ohm)
187.5	125	750	40	50.59	59.97	78.13
187.5	125	1250	40	53.00	59.98	110.84
187.5	125	750	40	51.59	59.13	12.55
187.5	125	750	40	51.20	59.55	54.68
200	150	1000	20	55.05	58.90	98.01
187.5	125	750	40	50.42	59.53	829.48
175	150	500	20	50.54	56.89	21513.81
187.5	125	750	80	49.00	59.33	141.71
175	100	500	60	47.56	56.99	29522.99
187.5	75	750	40	49.25	58.49	44.47
187.5	125	250	40	48.37	45.95	1000000
187.5	125	750	40	50.37	59.41	1200.05
212.5	125	750	40	51.78	60.26	22.97
187.5	125	750	40	51.44	59.98	60.08
175	150	1000	60	49.42	58.67	7077.70
175	150	500	60	47.82	58.59	10.85
187.5	175	750	40	52.44	60.10	77939.68
200	100	1000	60	50.34	59.81	637.26
200	150	500	20	52.05	59.14	1021.42
162.5	125	750	40	49.24	57.33	18912.60
175	150	1000	20	48.78	58.87	732.70
200	150	1000	60	50.59	61.11	874.42
200	100	1000	20	50.41	60.01	1228.65
200	150	500	60	49.59	59.82	510.80
175	100	1000	60	49.06	58.52	497.46
175	100	1000	20	48.71	58.25	4220.48
200	100	500	60	49.27	59.25	998.91
187.5	125	750	40	54.17	58.64	268.62
187.5	125	750	0	48.20	60.38	411.37
175	100	500	20	47.58	57.15	454831.37
200	100	500	20	49.84	59.73	2617.13

Table 7.4: Significance of input terms for microvia responses.

Input Factors	*p*-value					
	Top Via Diameter		**Via Wall Angle**		**Via Resistance**	
	40 μm	50 μm	40 μm	50 μm	40 μm	50 μm
Laser Fluence (E)	**0.005**	**0.005**	**0.002**	**0.000**	0.064	0.120
Shot Frequency (F)	0.075	**0.049**	0.637	0.361	0.378	0.255
Number of Pulses (PUL)	0.134	0.140	**0.018**	**0.023**	**0.018**	**0.023**
Helium Pressure Flow (P)	0.158	0.091	0.084	0.144	0.616	0.464
E x PUL	0.577	0.632	0.120	0.265	0.068	0.075
F x P	0.083	0.113	**0.041**	0.068	0.107	0.113

In comparison between the significant factors tabulated in Table 7.4 and those in Table 5.7, it appears that the fluence is the most important contributing factor in the formation of top diameter, since that factor is found to be significant in both studies. The significance of the effect of the number of pulses on the top diameter depended upon the vertical position of the debris removal system (see Table 5.7). In this experiment, since the debris removal systems were held constant in their optimal positions, the effect of the number of pulses loses significance. As for the via wall angle, since the effect of the positions of the debris removal systems were not investigated, both fluence and number of pulses became significant factors.

7.1.2 Neural Network Modeling

After the screening experiment, the laser input parameters (i.e., laser fluence, shot frequency, number of pulses, and helium pressure flow) were used as inputs to neural network models. Each NN model predicts the average value of one microvia response. The microvia responses include the top diameter, wall angle, and electrical resistance of both the 40 and 50 μm vias. ObOrNNS was used to build the neural process models. The

logarithmic data transformation was again used to reduce the range of the resistance data for both via sizes prior to modeling. During training of the networks, all data were used. Therefore, each network represents full experimental variations for a particular microvia response. Table 7.5 shows the training error and the NN structure for each microvia response.

Table 7.5: Neural network training for microvia responses.

Microvia Responses		**Neural Network Structure** ***x –[y] – z*** ***input – [hidden] – output***	**Average Percentage Training Error**
40 µm Via	Top Via Diameter	4 – [8 – 6] – 1	0.4663
	Via Wall Angle	4 – [5] – 1	0.2860
	Via Resistance	4 – [6 – 6] – 1	8.1127
50 µm Via	Top Via Diameter	4 – [8 – 8] – 1	0.4199
	Via Wall Angle	4 – [5] – 1	0.2695
	Via Resistance	4 – [7] – 1	9.8689

Since the 50 µm via wall angle model exhibited the lowest training error, this model was selected to determine the process failure scenarios. A process failure is defined as a deviation from a baseline (or nominal) value in the laser process inputs. In this research, the nominal values for the laser input parameters were 187.5 mJ/cm^2/pulse (laser fluence), 125 Hz (shot frequency), 750 pulses (number of pulses), and 40 psi (helium pressure flow). These nominal values were the center points of the CCC design. In order to be considered a failure, the percentage change in a particular microvia response due to

the deviation in one laser process input from its baseline had to be greater than the average percentage training error of the particular NN response model.

7.1.3 Failure Scenarios

Numerous mechanisms and combinations thereof can cause deviations in process responses. In this thesis, a process failure is defined as a deviation of more than 5% from a baseline (or nominal) value in the process inputs. To implement failure detection and diagnosis, both erroneous and nominal data must be obtained. Therefore, the laser process input parameters, which operators are allowed to adjust, were intentionally set to levels representing "deviations," and the excimer laser tool was run under the assumption that the input parameters were actually at their nominal levels. Three "normal" runs with nominal values and 16 different "faulty" runs were performed. Table 7.6 shows the failure scenarios selected with their corresponding degrees of deviation and combination levels.

The fabrication of 19 samples followed the process steps described in Chapter 3. Each combination of levels, as shown in Table 7.6, were used to fabricate one 6×6 inch board. Each board consisted of 32 replications of the 40 and 50 μm vias. After each run, response data originating directly from the tool and characterization of microvias formed by the ablation process were collected. To minimize run-to-run variation, all baseline runs were performed consecutively. Two additional tool responses – voltage (measured in volts) and head pressure (in mbar) – were included to make the failure detection and diagnosis more robust. Both tool parameters are subject to change based on the characteristics of the laser. Twenty-four to twenty-six measurements of the top via

diameter and via wall angle and 10 – 13 for the via resistance for each via size per board were performed. These measurements were divided into two groups: one was used to train the neural networks, while the other was used for validation.

Table 7.6: Failure scenarios and their corresponding levels.

Failure Scenarios	Percentage Deviation from Normal	Combination Level
Normal (3 replicates)	0%	188 125 750 40
Laser Fluence Small	+5%	**197** 125 750 40
Laser Fluence Large	+10%	**206** 125 750 40
Laser Fluence Small	-5%	**178** 125 750 40
Laser Fluence Large	-10%	**169** 125 750 40
Shot Frequency Small	+10%	188 **138** 750 40
Shot Frequency Large	+15%	188 **144** 750 40
Shot Frequency Small	-10%	188 **113** 750 40
Shot Frequency Large	-15%	188 **106** 750 40
Number of Pulses Small	+10%	188 125 **825** 40
Number of Pulses Large	+15%	188 125 **863** 40
Number of Pulses Small	-10%	188 125 **675** 40
Number of Pulses Large	-15%	188 125 **638** 40
Helium Pressure Flow Small	+10%	188 125 750 **44**
Helium Pressure Flow Large	+20%	188 125 750 **48**
Helium Pressure Flow Small	-10%	188 125 750 **36**
Helium Pressure Flow Large	-20%	188 125 750 **32**

The top via diameter was measured using a Nikon Microscope, and the via wall angle (θ, in degrees) was derived from top and bottom via diameter measurements using (3.1). The resistance of the ablated microvias was measured using a Tektronix Curve Tracer. The laser tool is equipped to automatically acquire voltage and head pressure data. The

voltage data was saved in a computer in time intervals provided by user, while the pressure data was manually collected. In addition to voltage, pulse fluence and total pulse counts were also stored. The shot frequency can be calculated using the pulse count and corresponding time intervals. In this thesis, the time interval selected was 0.18 minute ≈ 11 seconds.

7.2 Dempster-Shafer Theory of Evidence

Dempster-Shafer (D-S) theory originated from the concept of lower and upper probabilities first suggested by Dempster [45] and further developed by Shafer to manage epistemic probability, rather than chance or physical probability [46]. D-S theory is a useful methodology in malfunction diagnosis [67-68]. The technique allows the combination of different pieces of uncertain information generated by multiple sensors or models and provides the most likely source of deviation in the process responses under study.

7.2.1 Fundamental Concept

One of the basic concepts of Dempster-Shafer theory is the *frame of discernment* (symbolized by Θ), defined as a finite set of mutually exclusive and collectively exhaustive propositions. In failure diagnosis, Θ is the union of all possible failure propositions. Another important principle is the *degree of belief*, which can be explained with *support, plausibility,* and *uncertainty*. The likelihood of a failure proposition, for example A, is expressed as a bounded interval $[s(A), p(A)]$ that lies in [0, 1]. The support of proposition A, $s(A)$, measures the weight of evidence supporting A. The plausibility of

A, *p*(*A*), is the degree to which contradictory evidence is lacking. The uncertainty of *A,* *u*(*A*), is defined as the difference between plausibility and support of *A*. It is assumed that total belief is divided into various portions, each assigned to a subset of Θ.

Evidential intervals for individual failure are derived from a *basic probability mass distribution* (BPMD). A BPM is a function *m* satisfying:

$$m(f) = 0 \tag{7.1}$$

$$\sum_{A \subseteq \Theta} m\langle A \rangle = 1 \tag{7.2}$$

The quantity $m<A>$ is called the proposition A's basic probability mass, which is the measure of belief committed exactly to A, and not to any of its subsets, given a certain piece of evidence. To obtain the measure of the total belief committed to A, *Bel(A)*, one must add to $m<A>$ the quantities $m<B>$ for all proper subsets B of A. According to Dempster-Shafer theory, the plausibility of A, *p(A),* can be defined as 1 – *Bel(* $\overline{A}$ *),* which defines to what extent one fails to doubt in A or finds A plausible. It is straightforward to show that

$$p(A) = \sum_{B \cap A \neq f} m\langle B \rangle \tag{7.3}$$

The quantity *Bel(A)* can be interpreted as a global measure of one's belief that proposition A is true, while *p(A)* may be viewed as the amount of belief that could be placed in A, if further information became available.

7.2.2 Dempster's Rule of Combination

Two BPM's m_1 and m_2 in the same frame of discernment Θ can be combined by Dempster's rule of combination to yield a new BPM, $m = m_1 \oplus m_2$, which is defined by

$$m\langle Z\rangle = \frac{\sum m_1\langle X\rangle \cdot m_2\langle Y\rangle}{1-k}, \quad where, Z = X \cap Y \tag{7.4}$$

$$k = \sum m_1\langle X\rangle \cdot m_2\langle Y\rangle, \quad where, X \cap Y = f \tag{7.5}$$

This feature is useful in diagnosing failures because it provides the most likely culprit that causes deviation in process responses given multiple sources of evidence. In this thesis, the results of the D-S evidence combination are the support and plausibility assigned to each of the laser ablation process conditions. The parameter with the largest support is assumed to be the most likely cause of deviations in the process responses. Figure 7.3 shows a block diagram of the failure diagnosis methodology using NNs and D-S theory.

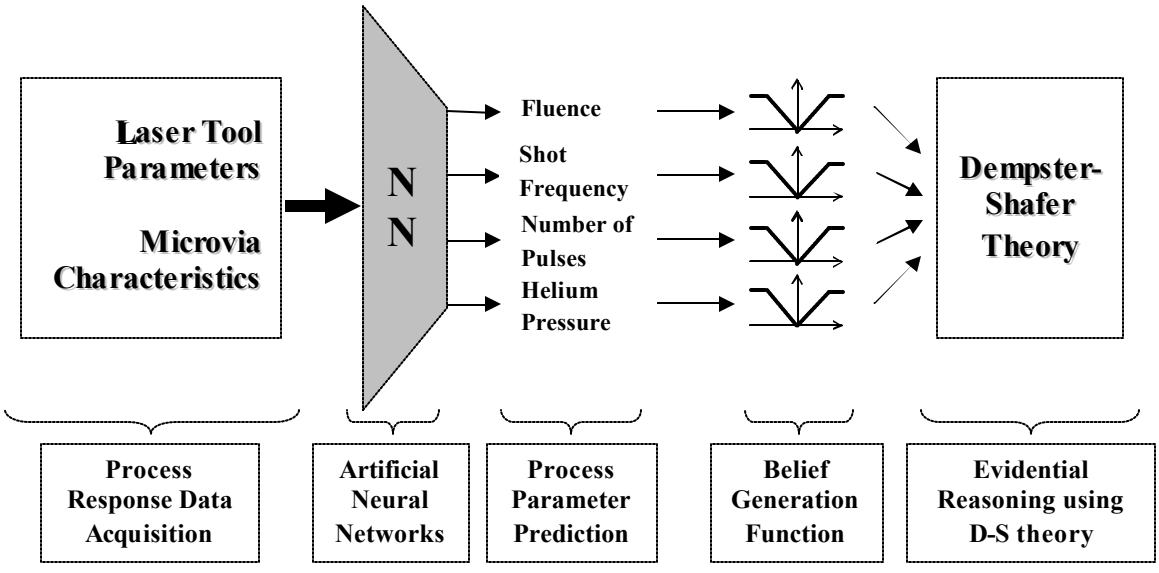

Figure 7.3. Functional schematic of failure diagnosis in the excimer laser ablation.

7.2.3 Belief Generation Function

To apply Dempster-Shafer theory for failure diagnosis, the basic probability masses (BPMs) were assigned based on neural network predictions. Given the assumption that deviations in the process responses were caused by a malfunction affecting a single process parameter, evidential belief for each parameter was generated using the following function (see Figure 7.4):

$$G(x) = \begin{cases} \left.\begin{cases} 0.8 & , x \geq x_U \\ C \times (x - x_T) & , x < x_U \end{cases}\right\} x \geq x_T \\ \left.\begin{cases} 0.8 & , x \leq x_L \\ C \times (x_T - x) & , x > x_L \end{cases}\right\} x < x_T \end{cases} \tag{7.6}$$

where, x is the predicted output of the neural network, x_T is the target process parameter value, x_U is the upper limit, and x_L is the lower limit. Limits were determined by trial and error and dependant on the parameter C, which is a constant used to adjust the slope of the belief generation function. These support functions assign small belief of failure to small deviations from target value and increase the belief linearly for increasing deviations. The maximum magnitude of the belief function is set to 0.8 in order to reflect approximately 20% uncertainty associated with parameter prediction of the NNs and the random variability of the excimer laser process. This uncertainty can be determined more precisely by either statistical means or using operator expertise. The BPMs of the four laser input parameters generated using (7.6) were combined using the Dempster-Shafer theory. Table 7.7 shows the values of the variables in (7.6) for the laser input parameters. The diagnostic routine was programmed in MATLAB™.

Table 7.7: Variables in belief generation function.

Laser Input Parameters	C	x_T	x_U	x_L
Laser Fluence (mJ/cm2/pulse)	$1/16$	187.5	200.3	174.7
Shot Frequency (Hz)	$1/21.67$	125	142.34	107.66
Number of Pulses	$1/130$	750	854	646
Helium Pressure Flow (psi)	$1/6.67$	40	45.33	34.67

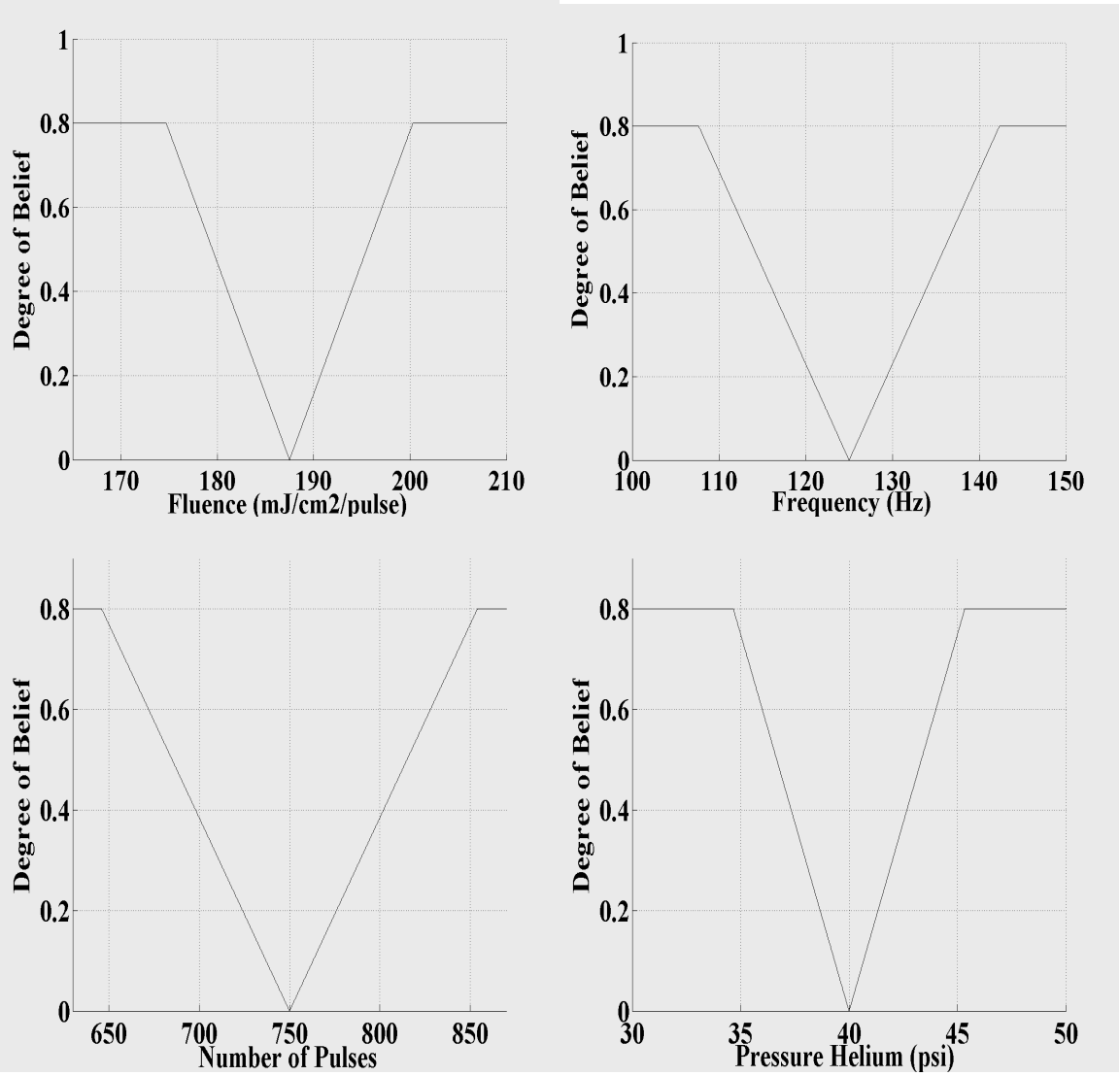

Figure 7.4. Belief generation functions for the four process input parameter.

7.3 Neuro-Fuzzy Logic

Fuzzy logic (FL) has been effectively used in the context of complex, ill-defined processes for which the knowledge of underlying dynamics is lacking [47][69]. The FL approach is to develop Fuzzy Inference Systems (FIS). A typical FIS, shown in Figure 7.5, consists of the following:

1) *Rule Base* containing the IF-THEN rules
2) *Database* that defines the membership functions, $0 \le m(S_i) \le 1$, of fuzzy sets
3) *Decision-Making Unit* that performs the inference operations
4) *Fuzzification* process that transforms the crisp inputs into degree of match
5) *Defuzzification* process that transforms the fuzzy results to crisp output.

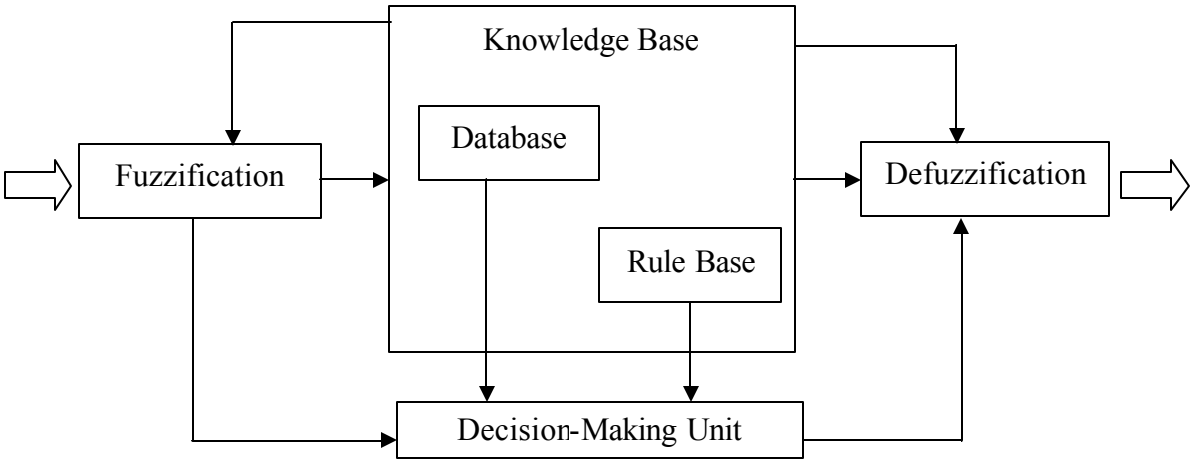

Figure 7.5. Fuzzy inference system.

7.3.1 Fundamental Concept

A fuzzy subset A of a universe of discourse U is characterized by a membership function $\mu_A: U \rightarrow [0, 1]$ which associates with each element u of U a number $\mu_A(u)$ in the interval [0, 1] which represents the grade of membership of u in A [70]. The *support* of A

is the set of points in U at which $\mu_A(u)$ is positive. A *fuzzy singleton* is a fuzzy set whose support is a single point in U. For example, A is a fuzzy singleton whose support is the point u, written as

$$A = \mu/u \tag{7.7}$$

where μ is the grade of membership of u in A. A fuzzy set A can be viewed as the union of its constituent singletons. For example, a fuzzy set A has a finite support $\{u_1, u_2, u_3\}$, then

$$A = \mu_1/u_1 + \mu_2/u_2 + \mu_3/u_3 \tag{7.8}$$

where, the + sign represents union rather than arithmetic sum. In case of non-finite support, the + sign may be replaced by the integral sign. A finite universe of discourse $U = \{u_1, u_2, u_3, u_4\}$ can be written as

$$U = 1/u_1 + 1/u_2 + 1/u_3 + 1/u_4 \tag{7.9}$$

Figure 7.6 shows two commonly used shapes for membership functions.

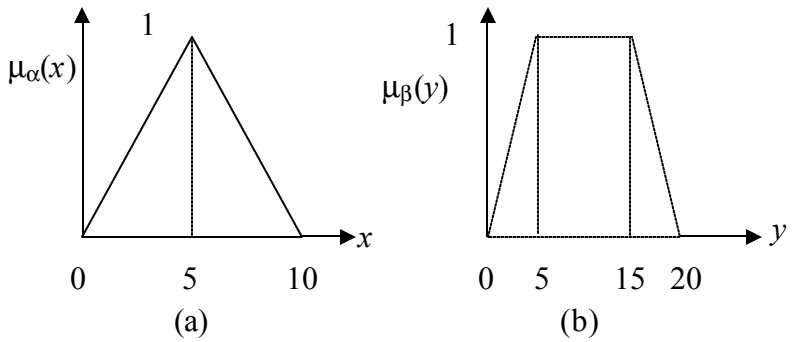

Figure 7.6. Continuous membership functions:
(a) symmetric triangle with support level U [0, 10],
(b) symmetric trapezoid with U [0, 20].

Some of the basic fuzzy set operations include "*and*" and "*or*" operators (symbolized by "? " and "V"), depicted by the minimum t-norm, and the maximum t-conorm, respectively. Another important operator is "*not*" which represents complement.

$$\text{Fuzzy-}and: \mu(\eta) = min\ [\mu(\xi_1),\ldots, \mu(\xi_v)] \tag{7.10}$$

$$\text{Fuzzy-}or: \mu(\eta) = max\ [\mu(\xi_1),\ldots, \mu(\xi_v)] \tag{7.11}$$

$$\text{Fuzzy-}not: \mu(\eta) = 1 - \mu(\xi_\iota) \tag{7.12}$$

where

$$min\ (a,b) = \begin{cases} a, & if \quad a \le b \\ b, & if \quad a > b \end{cases} \tag{7.13}$$

$$max\ (a,b) = \begin{cases} a, & if \quad a \ge b \\ b, & if \quad a < b \end{cases} \tag{7.14}$$

7.3.2 Diagnostic Implementation

The proper selection of the number, type and parameters of the fuzzy membership functions and rules is crucial to achieving the desired performance. In many situations, the selection is based on trial and error. In this thesis, an adaptive system facilitating learning and adaptation has been adopted that uses the neuro-fuzzy logic that follows the Sugeno-type fuzzy inference approach [48]. The fuzzy rules are of the form

$$\begin{aligned} &\text{IF Input1} = x \text{ AND Input2} = y, \\ &\text{THEN Output } z = ax + by + c \end{aligned} \tag{7.15}$$

The output membership functions are either linear or constant. For Sugeno's zeroth-order model, the output level z is a constant ($a = b = 0$). The output level z_i of each rule is weighted by the firing strength w_i of the rule. For example, for an AND rule with singleton Input1 = x and Input2 = y, the firing strength is

$$w_i = prod\ \{F_1(x), F_2(y)\} \tag{7.16}$$

where, $F_{1,2}\ (.)$ are the membership functions for Input1 and Input2, and where

$$prod\ (a,\ b) = ab \tag{7.17}$$

A Sugeno rule operates as shown in Figure 7.7.

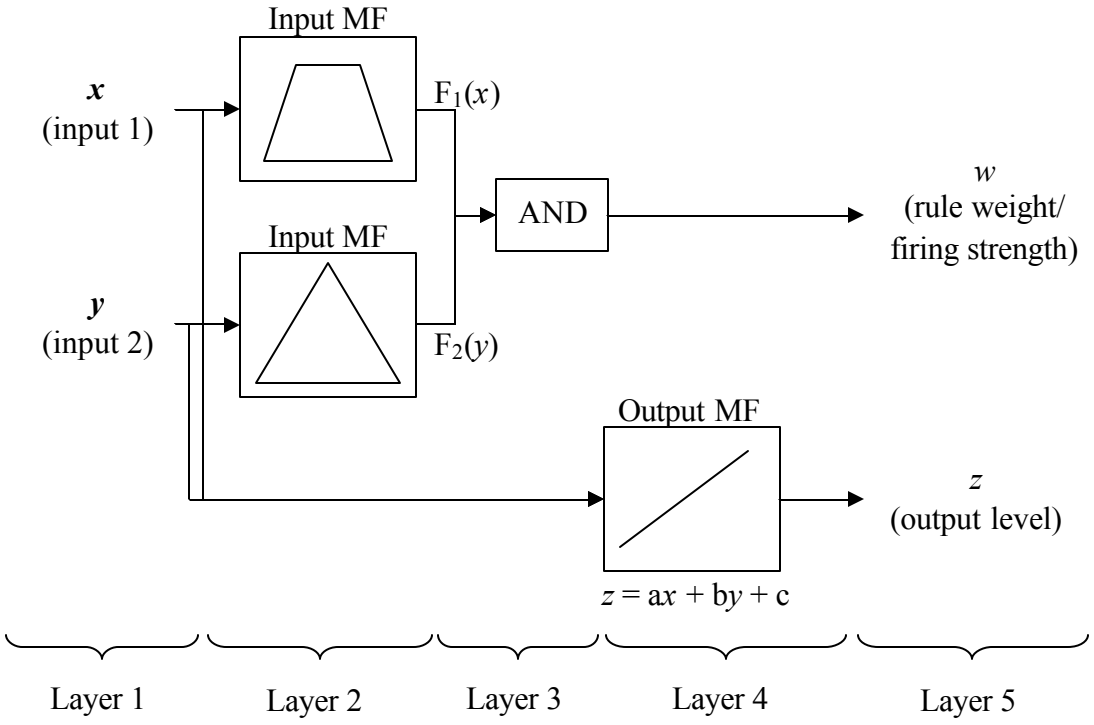

Figure 7.7. Sugeno's approach of fuzzy inference system.

As depicted in Figure 7.7, Layer 1 represents crisp inputs, and Layer 2 represents adaptive layer (the parameters are changed during training). The output of this layer is the degree of the membership of the input to the fuzzy membership function (MF). The parameters for the MF are optimized during training. Layer 3 represents a fixed (not adaptive) layer. In this layer, an arithmetic multiplication is performed. The output of this

layer is (7.16), which indicates the firing strength of the rule. In this layer, a normalization of the firing strength is also performed. Layer 4 represents an adaptive layer. In this layer, the output is the product of the normalized firing strength and a first order polynomial. For Sugeno's zeroth-order model, the output level z is a constant ($a = b = 0$); consequently, the constant is optimized during training. Layer 5 represents the output of the fuzzy inference system. The variables w and z are used in (7.18). The final output of the system is the weighted average of all rule outputs, computed as

$$Output_{FINAL} = \frac{\sum_{i=1}^{N} w_i z_i}{\sum_{i=1}^{N} wi} \tag{7.18}$$

The implementation of neuro-fuzzy approach used the MATLAB™ 6.5 Fuzzy Logic Toolbox [71]. A structure similar to that of a neural network, which maps inputs through membership functions and associated parameters and then through output membership functions and associated parameters to outputs, is used to interpret the input/output map. The toolbox includes the hybrid (i.e., error back-propagation and least-squares estimate [LSE]) training algorithm used in adjusting membership function parameters [72]. The hybrid training algorithm involves both a forward and a backward pass. On the forward pass, the inputs move forward from Layer 1 to Layer 4 (see Figure 7.7), where the consequent parameters (i.e., the coefficients in output z) are optimized using a LSE of the error between the predicted output and the actual output. On the backward pass, the RMSE of the training data set propagate back through the system and the premise parameters (membership functions) in Layer 2 are adjusted by the *gradient descent*

method. The default step-size was 0.01. The stopping criteria was either 20 epochs or a zero error tolerance, whichever was reached first. An epoch is one backward and forward pass. Membership functions for both input and output parameters were initially generated using the substractive clustering method [71]. The subtractive clustering algorithm was selected because it provided a quick one-time pass technique for estimating the minimal number of clusters and the cluster centers from the data set. These clusters defined the initial shape of membership functions and the rules. The toolbox includes the graphical adaptive neuro-fuzzy inference system (ANFIS) editor graphical user interface (GUI), which is used for building and analyzing the Sugeno-type ANFIS [73-75].

7.4 Neural Network and D-S Theory Based Detection and Diagnosis

This methodology employs response data originating directly from the equipment and characterization of microvias formed by the ablation process. The inputs to the neural networks were the excimer laser ablation process responses, which serve as failure evidence. The NNs predict the laser input process parameters that are the root cause of the observed evidence. For failure detection, the inputs of the NN consisted of the average values of 40 and 50 μm top via diameter, the average values of 40 and 50 μm via wall angle, the average values of 40 and 50 μm via resistance, the average and range values of voltage, and the maximum and mode values of head pressure. The output of the NN determined whether a combination of the inputs represented a normal condition (target output value < 0.5) or a failure (value ≥ 0.5). The *in-situ* voltage data used for NN training and testing was selected approximately 10 minutes after the laser tool started. At this point, the voltage was stable. The NN structure that resulted in the least

number of errors in failure detection was 10-3-1 (input-hidden-output neurons). The trained neural network for failure detection was validated using testing data that was not introduced during training. Testing resulted in 100% failure detected in 19 possible failure scenarios (see Table 7.8).

Table 7.8: Failure detection for testing data.

Failure Scenarios	**Neural Network Detection**
Normal 1	0.292626
Normal 2	0.468785
Normal 3	0.221619
Laser Fluence + Small (5%)	0.825914
Laser Fluence + Large (10%)	0.620095
Laser Fluence – Small (5%)	1.08651
Laser Fluence – Large (10%)	1.216133
Shot Frequency + Small (10%)	1.264132
Shot Frequency + Large (15%)	0.785479
Shot Frequency – Small (10%)	0.513271
Shot Frequency – Large (15%)	0.978001
Number of Pulses + Small (10%)	0.810993
Number of Pulses + Large (15%)	0.958297
Number of Pulses – Small (10%)	1.109626
Number of Pulses – Large (15%)	0.974408
Helium Pressure Flow + Small (10%)	0.905281
Helium Pressure Flow + Large (20%)	1.202801
Helium Pressure Flow – Small (10%)	1.037329
Helium Pressure Flow – Large (20%)	1.155875
NOTE: normal condition (value < 0.5) and a failure (value ≥ 0.5)	

For failure diagnosis, four types of neural networks were established to predict the process conditions that corresponded to the observed responses. The first model used the average values of 40 and 50 μm top via diameter and the average values of 40 and 50 μm

via wall angle as inputs. The second model used the average, standard deviation, and range values of voltage, as well as the maximum and mode values of head pressure as the inputs. The third model used combinations of the inputs of the previous two. The fourth model used the average values of 40 and 50 μm via resistance (logarithmically transformed) as inputs. The outputs on each case were the average values of the four process conditions (laser fluence, shot frequency, number of pulses, and helium pressure flow). Figure 7.8 shows the first NN model used for failure diagnosis. The NN structures that resulted in the least prediction error were 4-(8-8)-4 (input-hidden(s)-output) for the first model, 5-(6-6)-4 for the second model, 9-(6-6)-4 for the third model, and 2-8-4 for the fourth model.

Initially, each process response (i.e., top via diameter, via wall angle, via electrical resistance, voltage, and head pressure) was used to predict the four process conditions. These resulted in a less accurate failure diagnosis (i.e., the total number of false and missed alarms > 8 in 19 failure scenarios). Some modifications that involved combining some response parameters to predict the four process conditions were performed. The via resistance response was left independent of others because no further improvement was shown in the failure diagnosis when it was included. Table 7.9 shows the average percentage prediction errors for the four NNs. The second model had the largest prediction error mainly because helium pressure flow did not affect both voltage and head pressure (the debris removal system is an independent structure from the laser generator.)

Table 7.9: Prediction error for the neural networks used in failure diagnosis.

Neural Network Model	Neural Network Input	Neural Network Output	Average % Prediction Error
1st Model	• Top Via Diameter • Via Wall Angle	• Laser Fluence • Shot Frequency • Number of Pulses • Helium Pressure Flow	2.90%
2nd Model	• Voltage • Head Pressure	• Laser Fluence • Shot Frequency • Number of Pulses • Helium Pressure Flow	4.55%
3rd Model	• Combination of 1st and 2nd Models	• Laser Fluence • Shot Frequency • Number of Pulses • Helium Pressure Flow	3.39%
4th Model	• Via Resistance	• Laser Fluence • Shot Frequency • Number of Pulses • Helium Pressure Flow	3.46%

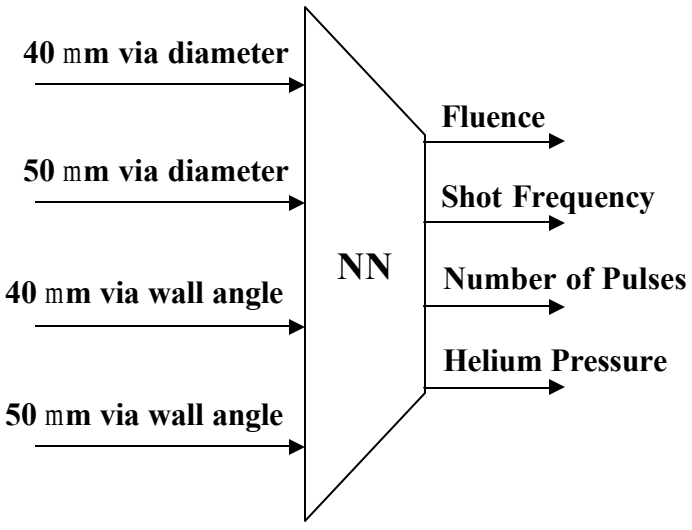

Figure 7.8. First neural network model used for failure diagnosis.

Using separate validation data, trained neural networks were used to predict the levels of all four laser input parameters simultaneously, and evidence combination was

performed on a run-to-run (R2R) basis. Once evidence combination was performed, individual support for the propositions was calculated using (7.4) and (7.5), and the corresponding plausibility was derived using (7.3). It was assumed that a malfunction maybe explained by an inadvertent shift in one of four process input parameters. It is also instructive to examine the belief of the "No Failure" condition as an initial diagnostic procedure – the lower its belief values, the higher possibility of a malfunction.

The results of diagnostic inference for all failure scenarios are shown in Table 7.10. The parameter with the largest support is assumed to be the most likely cause of deviations in the process responses. Failure diagnosis was successful, although there was one false alarm ("Normal 3") in 19 possible failure scenarios. This is shown in parentheses in Table 7.10. The false alarm was caused by a higher degree of support assigned to a perceived failure in the number of pulses than to the "No Failure" condition.

The two neural network models that assigned a high perceived failure in the number of pulses were the second and third models. This incorrect diagnosis was primarily due to inherent errors in the tool that can cause small shifts (i.e., increase) in voltage data compared with the data of the other two "Normal" scenarios. Thus, the voltage data for "Normal 3" had the closest resemblance to the data for "Pulse + Small" condition in terms of the average, standard deviation, and range. Another close resemblance between the voltage data of "Normal 3" and the data of "(Shot) Frequency + Small" condition was also found. However, the result based on combination of evidence using D-S theory showed a small degree of support for a failure in shot frequency.

Table 7.10: Failure scenarios and their corresponding support level.

Failure Conditions	Support Level Generated by Dempster's Rule of Combination				
	A	**B**	**C**	**D**	**E**
Normal 1	0.2901	0.02148	0.1698	0.01696	**0.5016**
Normal 2	0.04426	0.000226	0.36	0.001788	**0.5937**
Normal 3	0.3515	0.01905	**(0.6224)**	0.001471	**0.005451**
Fluence + Small (5%)	**0.8078**	0.0005736	0.1612	0.003319	0.02705
Fluence + Large (10%)	**0.999**	3.454e-006	0.0008437	0.0001309	3.501e-008
Fluence – Small (5%)	**0.9971**	4.638e-006	0.00221	0.0007226	9.21e-006
Fluence – Large (10%)	**0.9885**	0.0111	0.0001183	0.000284	4.222e-013
Frequency + Small (10%)	0.395	**0.5109**	0.09157	5.976e-005	0.002204
Frequency + Large (15%)	0.06877	**0.916**	0.01459	0.0004393	0.0001985
Frequency – Small (10%)	0.001863	**0.7061**	0.2774	0.01128	0.003159
Frequency – Large (15%)	2.111e-005	**0.9123**	5.105e-005	0.0876	7.132e-007
Pulses + Small (10%)	0.00505	0.004871	**0.9254**	0.06457	9.141e-006
Pulses + Large (15%)	0.2562	0.04951	**0.6939**	0.0002148	8.06e-005
Pulses – Small (10%)	0.03704	0.06608	**0.8924**	0.004243	2.695e-006
Pulses – Large (15%)	0.001798	0.01538	**0.9819**	0.0009106	1.743e-008
Pressure + Small (10%)	0.0004402	0.0362	0.000204	**0.9631**	6.305e-006
Pressure + Large (20%)	0.02139	0.004927	0.009104	**0.9645**	2.359e-007
Pressure – Small (10%)	0.0001692	5.893e-006	0.0002601	**0.9991**	0.0004153
Pressure – Large (20%)	0.0004432	0.001329	0.0005508	**0.9977**	1.131e-009

NOTE: **A** = Failure in Laser Fluence; **B** = Failure in Shot Frequency; **C** = Failure in Number of Pulses; **D** = Failure in Helium Pressure Flow; **E** = No Failure

7.5 Adaptive Neuro-Fuzzy Inference System Detection and Diagnosis

The zeroth-order model ANFIS networks were trained and validated based on process response data originating directly from the equipment and characterization of microvias formed by the ablation process to detect and diagnose potential sources of deviations in the responses. The inputs were the process responses, which serve as failure evidence. The ANFIS diagnosis predicted the malfunctioning laser parameter that was the root cause of the observed evidence. The assumption was that deviations in the process responses were caused by a malfunction affecting a single process parameter. Figure 7.9 shows a block diagram of this failure diagnosis methodology.

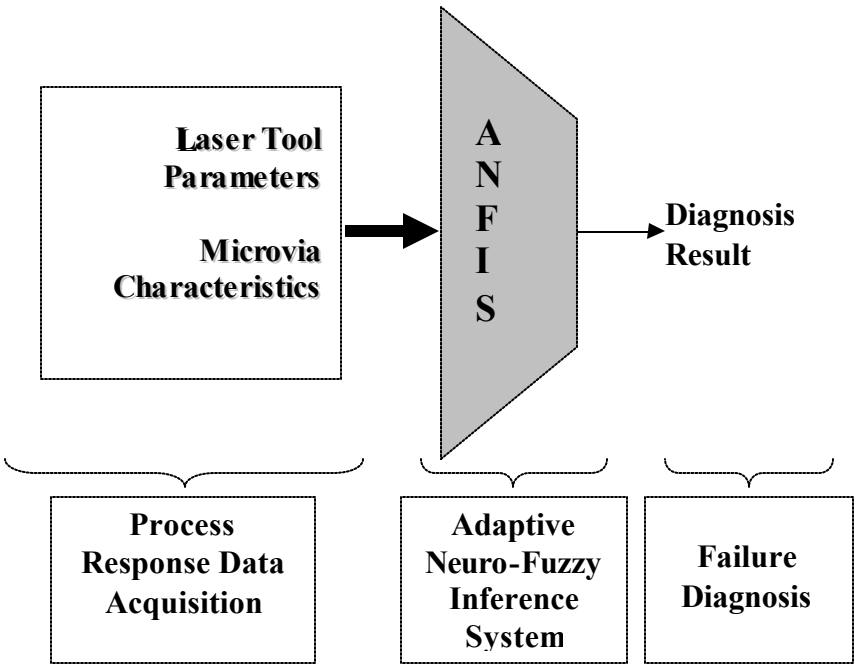

Figure 7.9. Functional schematic of failure diagnosis using ANFIS.

The inputs to ANFIS consisted of the average values of the 40 and 50 μm top via diameter, the average values of the 40 and 50 μm via wall angle, the average values of the 40 and 50 μm via resistance (logarithmically transformed), the average and range values of voltage (from data collected 10 minutes after the tool started), and the maximum and mode values of head pressure. In failure detection, the output of ANFIS is either a signal for a failure or a normal condition. A failure occurs when the predicted output is ≥ 0.5, and normal is when output < 0.5. Figure 7.10 depicts the ANFIS failure detection. The ANFIS formulation had 18 Gaussian membership functions per input.

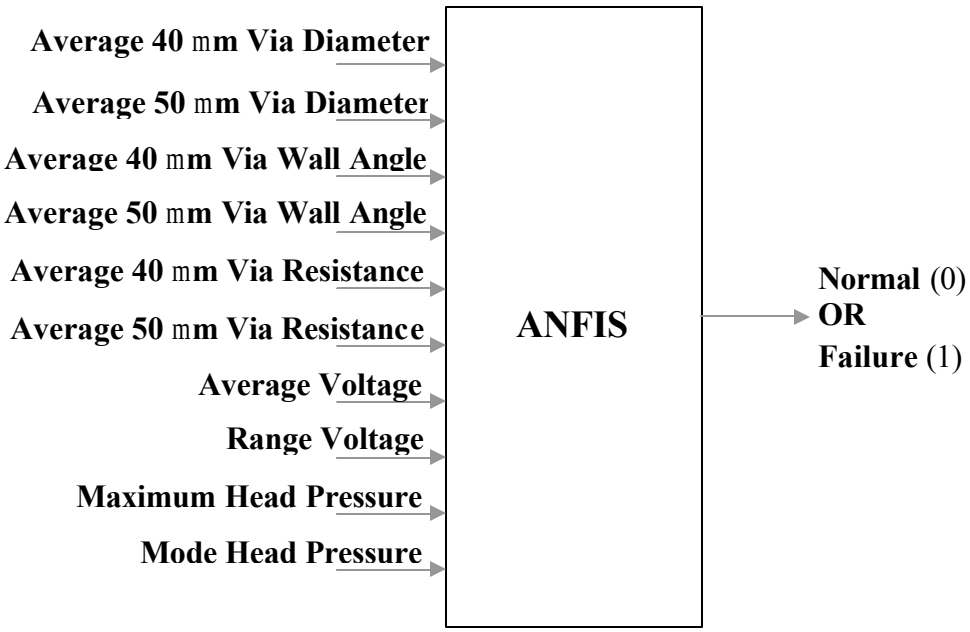

Figure 7.10. ANFIS failure detection in excimer laser ablation.

Using separate validation data, the trained ANFIS model was used to detect failure given several combinations of inputs. Failure detection was successful in 19 possible failure scenarios: only a single false alarm – "Normal 3" – occurred (see Table 7.11).

Table 7.11: Failure conditions and their corresponding test detection.

Test	Failure Conditions	ANFIS Detection
1	Normal 1	0.003205
2	Normal 2	0.3704
3	Normal 3	(1)
4	Laser Fluence + Small (5%)	0.6916
5	Laser Fluence + Large (10%)	1
6	Laser Fluence – Small (5%)	1
7	Laser Fluence – Large (10%)	1
8	Shot Frequency + Small (10%)	1
9	Shot Frequency + Large (15%)	1
10	Shot Frequency – Small (10%)	0.9833
11	Shot Frequency – Large (15%)	1
12	Number of Pulses + Small (10%)	0.9828
13	Number of Pulses + Large (15%)	1
14	Number of Pulses – Small (10%)	1
15	Number of Pulses – Large (15%)	1.001
16	Helium Pressure Flow + Small (10%)	1
17	Helium Pressure Flow + Large (20%)	1
18	Helium Pressure Flow – Small (10%)	1
19	Helium Pressure Flow – Large (20%)	1
NOTE: normal condition (value < 0.5) and a failure (value ≥ 0.5)		

The false alarm was primarily due to inherent errors in the tool that can cause small shifts (i.e., increase) in voltage data. As mentioned in Section 7.4, the voltage data for "Normal 3" had a close resemblance with the data of two failure conditions in terms of the average, standard deviation, and range. The failure conditions are "(Number of) Pulses + Small" and "(Shot) Frequency + Small". The false alarm could be rectified by means of voting. In other words, the final detection is based on the number of normal versus failure detections, whichever occurs most frequently. In this case, since two out of three "Normal" conditions were detected correctly by ANFIS, the final detection indicates a normal condition.

Failure diagnosis using ANFIS makes use of an integer (0 or 1) indicating whether a particular laser input process is malfunctioning or not. One ANFIS model is trained and subsequently validated for one laser input process. For example, the ANFIS model dedicated for laser fluence predicts whether the process evidence is caused by a failure in fluence ($value \geq 0.5$) or other than fluence ($value < 0.5$). The ANFIS models for laser fluence, shot frequency, number of pulses, and helium pressure flow diagnosis had five, 18, 12, and seven Gaussian membership functions per input, respectively.

Figure 7.11 depicts frequency diagnosis. If the process evidence points to, for example, a failure in fluence, another ANFIS model is used to determine which type of failure mode in fluence causes the deviation in process responses. Each process input that is prone to fail has four failure modes (represented by the integers 1 – 4). Thus, a positive small failure is represented by $0.5 \leq value < 1.5$. Similarly, a positive large failure is represented by $1.5 \leq value < 2.5$, a negative small failure $2.5 \leq value < 3.5$, and a negative large failure $3.5 \leq value < 4.5$. The ANFIS models for determining modes in laser fluence, shot frequency, number of pulses, and helium pressure flow diagnosis had 17, 19, 17, and 19 Gaussian membership functions per input, respectively. Table 7.12 shows the failure parameters and their corresponding target values. Figure 7.12 illustrates fluence mode diagnosis.

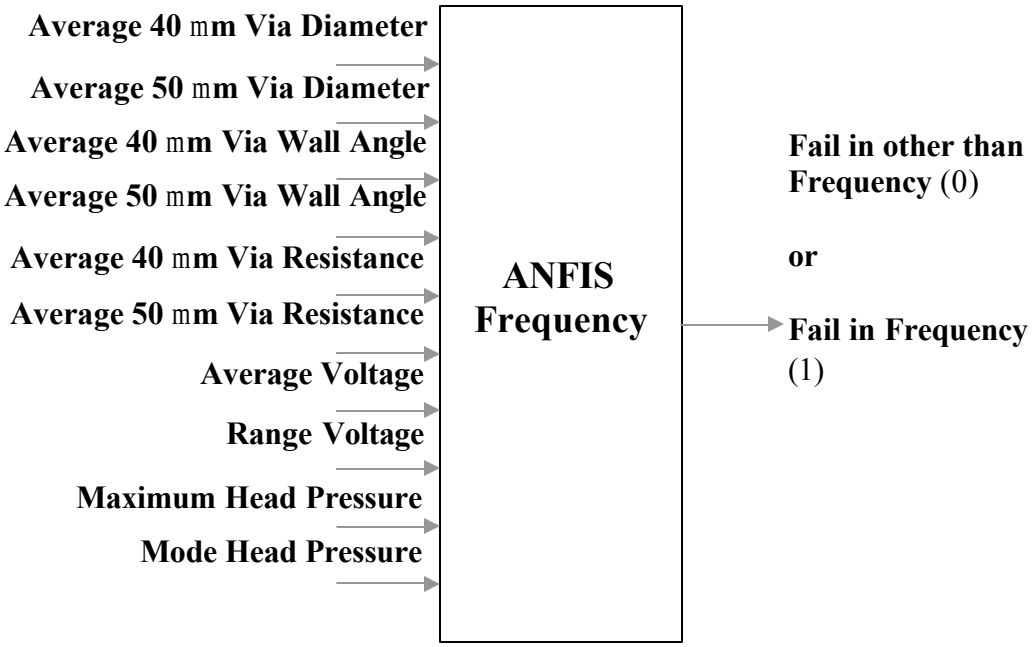

Figure 7.11. The I/O of ANFIS shot frequency diagnosis.

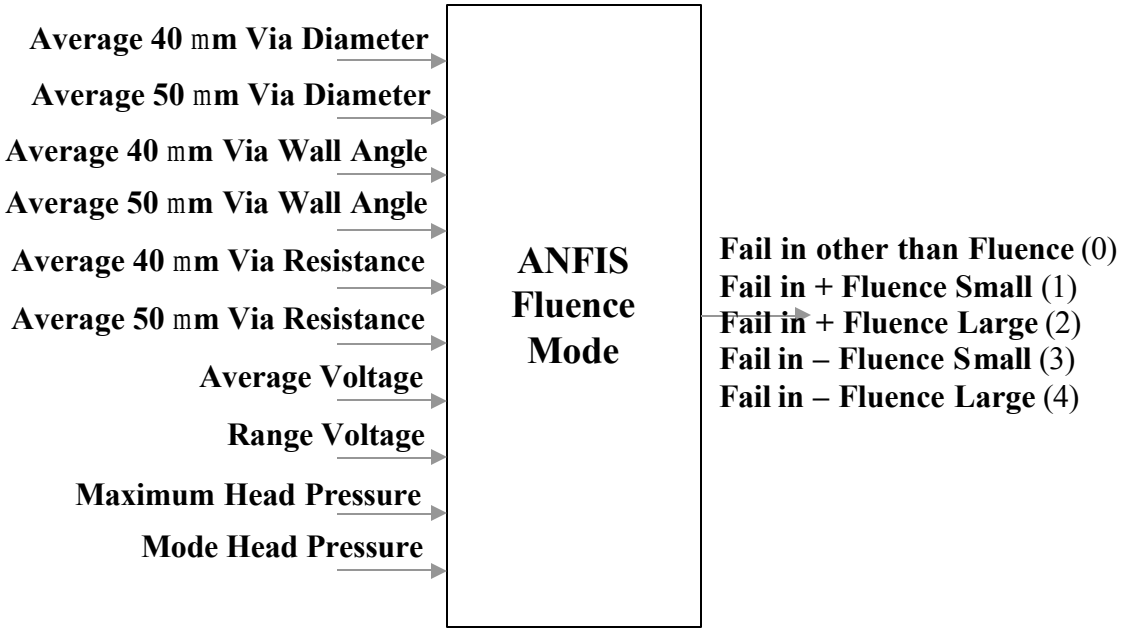

Figure 7.12. The I/O of ANFIS laser fluence mode diagnosis.

Table 7.12: Failure parameters and modes and their corresponding target values.

No Failure/ Failure	Target	Failure Parameter	Target	Failure Mode	Target
No Failure	0				
Failure	1	Fail in Laser Fluence	1	+5%	1
				+10%	2
				-5%	3
				-10%	4
				Other	0
		Fail in Other than Fluence	0		
		Fail in Shot Frequency	1	+10%	1
				+15%	2
				-10%	3
				-15%	4
				Other	0
		Fail in Other than Frequency	0		
		Fail in Number of Pulses	1	+10%	1
				+15%	2
				-10%	3
				-15%	4
				Other	0
		Fail in Other than Pulses	0		
		Fail in Helium Pressure Flow	1	+10%	1
				+20%	2
				-10%	3
				-20%	4
				Other	0
		Fail in Other than Helium Pressure	0		

The results of diagnostic inference for all failure scenarios are shown in Table 7.13. Failure diagnosis was successful, although there was one false alarm – "Normal 3" – and one missed alarm – "(Shot) Frequency + Small" – in the 19 possible failure scenarios. These are shown in parentheses in Table 7.13. The false alarm was caused by a prediction assigned to a perceived failure in the shot frequency, particularly in "(Shot) Frequency + Large", rather than to the "No Failure" condition. As mentioned in Section 7.4, the

voltage data of "Normal 3" had a close resemblance with the data of "(Shot) Frequency + Small" condition. This contributes to the false alarm generated and diagnosed by ANFIS.

The missed alarm in the failure diagnosis was caused by the perceived failure in "(Shot) Frequency + Large" than the failure in "(Shot) Frequency + Small" condition. This incorrect diagnosis was mainly due to the lack of distinct failure evidence corresponding to the characteristics of microvias and tool response parameters between the two frequency failures modes.

7.6 Summary

In this chapter, two approaches: (1) feed-forward neural networks and (2) adaptive neuro-fuzzy networks were utilized for run-to-run failure detection and diagnosis in excimer laser ablation. Deviations in response data originating directly from the equipment and characterization of microvias formed by the ablation process were employed as evidence of malfunctions affecting a single process parameter. The microvia response characteristics consisted of via diameter, via wall angle, and via resistance. The tool response parameters include voltage and head pressure. Resistance measurements on copper deposited in the ablated vias were performed to characterize the degree to which debris remaining inside the vias affected quality. The laser system parameters included laser fluence, shot frequency, number of pulses, and helium pressure flow. To simulate failures, the excimer laser ablation process conditions were intentionally set to certain levels away from the nominal values. Fabrication of both erroneous and nominal data was conducted, and the data collected was then divided into two groups: one for training, and the other one for testing.

Table 7.13: Failure conditions and their corresponding diagnosis.

Test	Failure Conditions	Fail in Fluence	Fail in Frequency	Fail in Pulses	Fail in Pressure Flow
		Failure Mode	Failure Mode	Failure Mode	Failure Mode
1	Normal 1	-0.001648	1.88e-005	0.08345	-0.005285
		-0.002401	5.966e-013	0.013	-2.441e-017
2	Normal 2	-0.003911	-0.02377	0.3682	-0.0002974
		-0.004001	-0.0002771	0.3153	-2.898e-021
3	Normal 3	-0.0004775	**(0.8878)**	0.1846	-0.0005171
		0.1699	**1.957**	0.3913	-1.031e-019
4	Fluence + Small (5%)	**0.9536**	-0.009497	0.1552	-0.0009709
		0.7615	-7.124e-007	0.1095	1.597e-022
5	Fluence + Large (10%)	**1.004**	-2.442e-005	-0.0331	-0.0008384
		2.005	-1.237e-012	-0.002134	-3.594e-028
6	Fluence – Small (5%)	**0.976**	-1.256e-009	0.01462	0.001032
		3	-5.623e-025	0.0007858	-5.324e-027
7	Fluence – Large (10%)	**1.009**	-5.071e-013	-0.001233	-0.0005874
		3.986	-6.038e-033	-3.328e-006	3.722e-032
8	Frequency + Small (10%)	-0.0008832	**0.9479**	0.01625	-0.0001511
		-0.01441	**(1.711)**	0.4077	-9.561e-020
9	Frequency + Large (15%)	-0.0005344	**0.9511**	0.0609	0.001814
		0.04195	**1.982**	0.3586	3.365e-019
10	Frequency – Small (10%)	0.007322	**0.7372**	-0.005312	-0.001191
		0.03346	**2.783**	-0.06931	1.928e-023
11	Frequency – Large (15%)	-0.0001736	**0.8625**	0.0002735	0.3139
		2.796e-011	**3.959**	2.008e-008	0.2958
12	Pulses + Small (10%)	-0.003881	-0.0002573	**0.72**	-0.0009315
		-0.0004307	-2.795e-009	**0.9121**	-1.609e-018
13	Pulses + Large (15%)	-0.001565	0.001146	**0.8966**	-0.0002674
		0.002469	1.687e-008	**1.978**	-4.71e-024
14	Pulses – Small (10%)	0.0005638	-0.03969	**0.9448**	-0.0007093
		-0.007712	-0.0007418	**3.264**	-8.036e-022
15	Pulses – Large (15%)	0.0978	0.001516	**1.021**	0.01347
		-0.002233	5.648e-008	**3.993**	8.808e-020
16	Pressure + Small (10%)	-0.0001843	7.546e-007	3.286e-005	**1.001**
		1.678e-010	1.132e-015	-4.906e-009	**0.9889**
17	Pressure + Large (20%)	-0.0002015	0.04023	1.715e-005	**0.7978**
		1.276e-010	0.0009067	4.255e-010	**1.924**
18	Pressure – Small (10%)	-0.0001981	0.001529	-0.0001603	**1.023**
		1.965e-013	1.187e-006	-3.7e-011	**3.059**
19	Pressure – Large (20%)	-0.0001845	-0.01766	-7.087e-005	**1.09**
		1.782e-011	-0.0002141	5.217e-010	**3.764**

In the first approach, failure detection and diagnosis in the excimer laser process was achieved using a combination of NNs and Dempster-Shafer theory. The NN models were used to generate evidential belief for each laser process inputs prone to fail. D-S theory was used to combine evidences. The parameter with the largest support was assumed to be the most likely cause of deviations in the process responses. Successful failure detection was achieved in 100% of 19 possible failure scenarios. Moreover, successful failure diagnosis was also achieved, with only a single false alarm occurred in the 19 failure scenarios. Based on these results, NNs were demonstrated to be an effective technique for excimer laser ablation failure detection and diagnosis. D-S theory, used in conjunction with the NNs, was shown to be an appropriate inference technique.

In the second approach, the adaptive neuro-fuzzy inference system was used to detect and diagnose failures in the process. ANFIS was used to predict the laser input parameter that acted as a root cause of deviations in process responses. The prediction was categorized with numeral integers representing input parameters. Results indicated only a single false alarm occurred in 19 possible failure detection scenarios. In failure diagnosis, a single false alarm and a single missed alarm occurred. Thus, ANFIS was also a suitable technique for failure detection and diagnosis in excimer laser ablation for microvia formation.

In comparing NN technique and ANFIS, the NN performed more accurate failure detection (i.e., 100% detection) in 19 possible scenarios. In terms of failure diagnosis, both techniques showed comparable capability. The two techniques indicated different diagnosis results for failures potentially caused by shot frequency and number of pulses, both of which are provided by users of the laser tool are used and controlled by a

computer system. The diagnosis was likely confused by the fact that shot frequency and number of pulses are dependent. A failure in one parameter during operation affects the other parameter. The dependence of the two parameters violates the assumption that a malfunction is caused by an inadvertent shift in only one process input parameter. Studies involving multiple sources of malfunctions will be addressed in future work. NNs and ANFIS achieved approximately 95% and 90% successful diagnosis results, respectively.

These results can contribute to maintaining consistent ablation process, thus minimizing erroneous processing and equipment downtime, and ultimately leading to improved process yield.

CHAPTER 8

CONCLUSIONS AND FUTURE WORK

This thesis focuses on a key piece of electronics manufacturing equipment and its underlying process: excimer laser ablation. The Anvik laser tool emits 308 nm ultraviolet light. This tool was utilized to fabricate microvias in a multilayer microelectronics substrate. The ablated material was Kapton® E polyimide, and the via sizes ranged from 10 – 50 μm. The characteristics of the microvias generated depended on complex interactions between the laser and the material. Due to the high complexity of the process, it is difficult to quantify the exact mathematical relationship between the input factors and target parameters. Several techniques for process characterization, modeling, and optimization have been presented. Moreover, two methodologies for automated run-to-run process failure detection and diagnosis have also been proposed to potentially lower equipment downtime. The methodologies have been evaluated and validated for microvia formation using the excimer laser ablation system. This chapter discusses the contribution of this thesis and suggests potential future work.

8.1 Contributions of the Research

This research attempts to characterize the excimer laser ablation process. The methods used to model and optimize the process (i.e., statistics and artificial intelligence), as well as to detect and diagnose failures, offer significant advantages in terms of

accuracy and robustness. In real manufacturing settings, the methodologies developed in this research can reduce misprocessing and equipment downtime.

8.1.1 Modeling and Optimization

In the first phase of this research, the excimer laser ablation process was characterized using statistical methods. Such characterization is important to determine the significant laser system parameters affecting microvia process responses. Subsequently, neural networks were used to model the process based on the identified significant parameters. The models generated can be visualized using multidimensional response surfaces that depict the overall trends of microvia response variations with respect to laser input parameters. Both individual response and combined NN models were generated. Although the individual response models elucidate the conditions that impact a given response, the adjustments required to optimize these conditions for all responses simultaneously are often conflicting. The combined model, therefore, has greater practical utility, since all responses are subject to the same set of process conditions. Neural network modeling is superior in accuracy to statistical methods and easier to derive than physical or analytical methods [55]. Moreover, it does not require any assumptions regarding the physical and chemical aspects of a process or system behavior. Thus, neural networks can be of significant interest in high-volume manufacturing where accurate nonlinear modeling techniques are often required.

In the second phase, genetic algorithms, in conjunction with the NN models, were used for process optimization. In this optimization step, a systematic method of identifying specific sets of excimer laser process conditions (or "recipes") to achieve

desired microvia targets was executed. These desired targets included open vias, specific via diameters, steep wall angles, and low via resistance. The genetic algorithm approach is capable of efficient search through large nonlinear design space to obtain optimal response values. Furthermore, this approach requires only objective function value information. No derivative information or continuity of the solution space assumption is required. Experimental verification demonstrated that the optimized recipes improved ablation results by as much as 40% for film thickness, 30% for the via diameter, 9% for via wall angle, and by more than 100% for via resistance.

8.1.2 Run-to-Run Failure Detection and Diagnosis

In the final phase of this research, run-to-run process failure detection and diagnosis were performed. The methodologies used involved neural networks and Dempster-Shafer theory, as well as neuro-fuzzy networks, to detect process shifts and identify the most likely culprit that caused deviations in the process responses. These deviations are indications of necessary process adjustments or malfunctions, and they affect the reliability and performance of the process responses. Both D-S theory and neuro-fuzzy logic were used to develop an automated inference system.

Successful failure detection was achieved in 100% of 19 possible failure scenarios using NNs. Moreover, successful failure diagnosis was achieved (95% successful diagnosis), with only a single false alarm occurred in the 19 failure scenarios using the combination of NNs and D-S theory. As for the neuro-fuzzy approach, results indicated only a single false alarm occurred in 19 possible failure detection scenarios. In failure

diagnosis, 89% successful diagnosis was achieved, with a single false alarm and a single missed alarm.

Needless to say, *in-line* malfunction diagnosis is extremely valuable in semiconductor manufacturing and microelectronics packaging. The failure detection methodologies developed herein can prevent large losses during microvia fabrication. In addition, the proposed malfunction diagnosis systems can indicate which laser system parameter has shifted, thereby allowing necessary process adjustments to be performed rapidly. Malfunction detection and diagnosis contribute to maintaining consistent via fabrication, thus minimizing production loss and overall manufacturing cost.

8.2 Future Work

Further modification and enhancements to the proposed methods for process modeling and optimization can be performed. The complexity of the ablation process depends on many factors affecting the interaction between the laser and the material. Additional laser system parameters and/or varieties of material ablated should be included in future studies to generate more robust models.

Regarding the neural networks, apart from feed forward networks, recurrent networks can be incorporated to model time-dependent process behavior. Such study, however, requires careful and accurate real-time *in-situ* process monitoring, which is not feasible for the current work due to equipment limitations. Process monitoring of the debris generated during ablation using sensors is by far the most intriguing, yet challenging task. The relationship between the debris and the process responses requires better understanding. Regarding the optimization stage, a hybrid optimization technique

combining genetic algorithms and hill climbing approaches such as gradient decent could be used to speed up the performance of genetic optimization and generate more accurate solutions.

Further modification and enhancements to the proposed methods for run-to-run process failure detection and diagnosis can also be performed. With regard to the false and missed alarm issues, a subsystem following the diagnosis can be placed employing a voting strategy. In other words, the final decision would represent the most frequent result of the decisions of multiple diagnostic systems. Both false and missed alarm issues can also be reduced by obtaining more experimental data for neural network and neuro-fuzzy network training and testing resulting in more robust models.

It is also suggested that the types of malfunction be further examined with regard to the percentage deviations of a process parameter. A small shift is hard to detect and diagnose because the effect of such a shift might not be readily apparent from the process responses. A more robust real-time fault detection and diagnosis system can also be developed by means of *in-situ* process sensors and neural networks. Such a system can identify the *incipient* failures prior to misprocessing during manufacturing; thus, potentially eliminating manufacturing loss. To establish such a diagnostic system, more diverse types of malfunction cases should be considered, since in reality, not only single component failures, but multiple simultaneous component failures can cause malfunctions. To diagnose multiple component failures, it is necessary to study the effects of simultaneous deviations in the laser system parameters on microvia process responses. Such effects can then be used to train and validate neural networks to predict the shifted parameters. D-S theory can be used to combine multiple evidences and infer

which parameter(s) have shifted. This study, however, requires more experiments, which are costly and time consuming. In a university research environment, there is usually a limitation in the number of parameters in the tool that can be adjusted resulting in limited types of malfunctions. A complete real-time diagnosis system for excimer laser ablation will be valuable in maintaining high yield and minimizing manufacturing cost.

APPENDIX A

MATLAB Code for Dempster-Shafer Theory of Inference

A.1 RunDS.m

```
%****************************************************************
% Author: Ronald Setia                                          %
% Advisor: Prof. Gary S. May                                    %
% Intelligent Semiconductor Manufacturing Group                 %
% Dempster-Shafer Theory of Inference                           %
%****************************************************************

clear all

%****************************************************************
% Load the data from 4 neural network
%****************************************************************

evidence = 4;

eviname (1,1) = {'viadiawallvolt'};
eviname (2,1) = {'viadiawall'};
eviname (3,1) = {'insitu'};
eviname (4,1) = {'viares'};


% Filename with .dat extension is preferable ****************************

if ismember('viadiawallvolt',eviname)==1,
   file_viadiawallvolt = load ('viadiawallvolt.dat');
   vdwv_size = size(file_viadiawallvolt);
end

if ismember('viadiawall',eviname)==1,
   file_viadiawall = load ('viadiawall.dat');
end
```

```
if ismember('insitu',eviname)==1,
   file_insitu = load ('insitu.dat');
end

if ismember('viares',eviname)==1,
   file_viares = load ('viares.dat');
end


%*****************************************************************
% Belief Functions                                               %
% To generate beliefs for each component predicted by neural network sensor  %
%*****************************************************************

%TARGET REQUIREMENTS
%Target values for the laser process inputs

target_fluence = 187.5;
target_frequency = 125;
target_userPulse = 750;
target_userHelium = 40;

for (design=2:2),
S1=sprintf('\n');
disp(S1);
S1=sprintf('DESIGN No: %d', design);
disp(S1);
success=0;

if (design==2),
%Run D-S theory for all testing data ... in this case 19

for (numtest=1:vdwv_size(1)),
sprintf('TEST DATA No: %d',numtest);

    temp_vdwv = file_viadiawallvolt(numtest,:);
    temp_vdw = file_viadiawall(numtest,:);
    temp_vr = file_viares(numtest,:);
    temp_ins = file_insitu(numtest,:);

    combo(1,:) = temp_vdwv;
    combo(2,:) = temp_vdw;
    combo(3,:) = temp_ins;
    combo(4,:) = temp_vr;
```

```
%The laser process inputs...in this case 4:
%laser fluence, shot frequency, user number of pulses, and user helium pressure flow

for j = 1:evidence,
   numhypo (j,1) = 5;

      %A = Laser fluence (mJ/cm2/pulse)
      %B = Shot frequency (Hz)
      %C = User number of pulses
      %D = User helium pressure flow (psi)
      %F = Error
      %E = No Failure
      %ABCD mean UNION of (A,B,C,D)

      hyponame (j,1) = {'A'};
      hyponame (j,2) = {'B'};
      hyponame (j,3) = {'C'};
      hyponame (j,4) = {'D'};
      hyponame (j,5) = {'F'};

   for k = 1:4,
%*****************************************************************
% The Belief Functions                                           %
%*****************************************************************
      if strcmp('A',hyponame(j,k))==1,
         if (combo(j,k)>=target_fluence),
            if (combo(j,k)>200.3),
               Belief = 0.8;
            else
               Belief = (combo(j,k)-target_fluence) ./ 16;
            end
         else
            if (combo(j,k)<174.7),
               Belief = 0.8;
            else
               Belief = (target_fluence-combo(j,k)) ./ 16;
            end
         end

      elseif strcmp('B',hyponame(j,k))==1,
         if (combo(j,k)>=target_frequency),
            if (combo(j,k)>142.34),
               Belief = 0.8;
            else
               Belief = (combo(j,k)-target_frequency) ./ 21.67;
```

```
            end
        else
            if (combo(j,k)<107.66),
                Belief = 0.8;
            else
                Belief = (target_frequency-combo(j,k)) ./ 21.67;
            end
        end

    elseif strcmp('C',hyponame(j,k))==1,
        if (combo(j,k)>=target_userPulse),
            if (combo(j,k)>854),
                Belief = 0.8;
            else
                Belief = (combo(j,k)-target_userPulse) ./ 130;
            end
        else
            if (combo(j,k)<646),
                Belief = 0.8;
            else
                Belief = (target_userPulse-combo(j,k)) ./ 130;
            end
        end

    elseif strcmp('D',hyponame(j,k))==1,
        if (combo(j,k)>=target_userHelium),
            if (combo(j,k)>45.33),
                Belief = 0.8;
            else
                Belief = (combo(j,k)-target_userHelium) ./ 6.67;
            end
        else
            if (combo(j,k)<34.67),
                Belief = 0.8;
            else
                Belief = (target_userHelium-combo(j,k)) ./ 6.67;
            end
         end
    end

    hypothesis (j,k) = Belief;
end

hypothesis (j,5) = combo(j,5);
```

```
   %Calculate the E = No Failure based on A, B, C, D
   numhypo (j,1) = 6;
   hyponame (j,6) = {'E'};
   hypothesis (j,6) = (0.8-hypothesis(j,1))*(0.8-hypothesis(j,2))*
                      (0.8-hypothesis(j,3))*(0.8-hypothesis(j,4));
   convert01 = sum(hypothesis(j,1:6));

   for k = 1:6,
      hypothesis (j,k) = hypothesis(j,k)/convert01;
   end
end

hypothesis

%*****************************************************************
%RESULTS from DST function
[newm, newMVal, K] = DST(evidence, hyponame, hypothesis, numhypo);
%*****************************************************************

%PRODUCE RESULTS ***********************************************
[success] = GetResult(newm, newMVal, K, numtest,success);
%*****************************************************************

clear j;
clear k;
clear hyponame;
clear hypothesis;
clear numhypo;

hypothesis = [];

end
end

DS2=sprintf('Success = %d out of 19', success);
disp(DS2);
end
```

A.2 DST.m

```
function [newm, newMVal, K] = DST(evidence, hyponame, hypothesis, numhypo)

%Calculating Dempster's rules for the combination of evidence **************
% hyponame: the name of hypothesis in cell array (one row one evidence)
% hypothesis: the value of the hypothesis in matrix (one row one evidence)
% numhypo: column vector of number of hypothesis
% hyponame: new bpm name of combined evidences in vector cell array
% hypothesis: new bpm value of combined evidences in vector
% K = conflict
%*************************************************************

for i = 1:(evidence-1),
   [n, v, K] = dempster(hyponame, hypothesis, numhypo);
   temp1 = hyponame;
   temp2 = hypothesis;
   hyponame = {};
   hypothesis = [];
   hyponame(1,:) = n;
   hypothesis(1,:) = v;

   if (evidence-i+1) >= 3,
      for j = 3:(evidence-i+1),
         for k = 1:length(temp1(j,:)),
            hyponame(j-1,k) = temp1(j,k);
            hypothesis(j-1,k) = temp2(j,k);
         end
      end
   end
end
%*************************************************************


%The results from Dempster's rule of combination ************************
%New Basic Probability Mass Function: SUM(X) = 1
newm = n;
newMVal = v;

K;
return
```

A.3 GetResult.m

```
function S = result(newm,newMVal,K,testnum,S)
%The less the WoC, the more consistent evidences between 2 bpm's **********
WeightofConflict = log(1/(1-K));
DS=sprintf('Weight of Conflict = %9.5f ', WeightofConflict);
disp(DS);
%*****************************************************************

%Calculating the SUPPORT and PLAUSIBILITY for each Hypothesis *********
for i = 1:length(newm),
   support = 0;
   plausible = 0;

   for j = 1:length(newm),
      common = size(intersect(newm{i},newm{j}));

      if ismember(newm{j},newm{i}) & (length(newm{i}) >= length(newm{j})),
         sprintf('support');
         i;
         j;
         support = support + newMVal(j);
      end

      if ismember(newm{i},newm{j}) & (length(newm{i}) < length(newm{j})),
         sprintf('plausible option 1');
         i;
         j;
         plausible = plausible + newMVal(j);

      elseif (common(2) > 0),
         sprintf('plausible option 2');
         i;
         j;
         plausible = plausible + newMVal(j);
      end
   end

   data_support(i) = support;
   data_plausible(i) = plausible;
end
```

```
if (testnum>=1 & testnum<=3),
   if data_support(6)==max(data_support),
      S=S+1;
   end

elseif (testnum>=4 & testnum<=7),
   if data_support(1)==max(data_support),
      S=S+1;
   end

elseif (testnum>=8 & testnum<=11),
   if data_support(2)==max(data_support),
      S=S+1;
   end

elseif (testnum>=12 & testnum<=15),
   if data_support(3)==max(data_support),
      S=S+1;
   end

elseif (testnum>=16 & testnum<=19),
   if data_support(4)==max(data_support),
      S=S+1;
   end
end

for i=1:length(newm),
   DS1=sprintf('\n');
   disp(DS1);
   DS1=sprintf('%s = [%0.4g, %0.4g]', newm{i}, data_support(i), data_plausible(i));
   disp(DS1);
end

return
```

A.4 dempster.m

```
% Dempster-Shafer Rule of Combination
% newhname: new bpm name of combined evidences
% newhvalue: new bpm value of combined evidences
% K = conflict

function [newhname, newhvalue, K] = dempster(hname, hvalue, numh)

%Initialization *****************
maxnumh = max(numh(1:2));
name = {};
value = [];
storeZEROname = [];
matrixname = {};
matrixvalue = [];
K = 0;
index = [];
%**************************


%Getting the intersection between 2 hyponame (2 hname) ******************
% e.g. AB & ABC = AB
for i = 1:maxnumh,
   for j = 1:maxnumh,
      matrixname (i,j) = {intersect(hname{1,j},hname{2,i})};
   end
end
%*****************************************************************


matrixname = matrixname'; %Transpose the matrix in accordance with its value
matrixvalue = hvalue(1,:)'*hvalue(2,:); %The matrix value
matrixvalue = num2cell(matrixvalue); %Change the matrix value to cell array


%Creating Structure for the name and the value ...easier to manipulate
DS = struct('symbol',matrixname,'symval',matrixvalue);

clear i,j;

%Searching the DS matrix for common elements and combining the values for
%the same element
%Check the current value in the matrix againts the next value in the matrix
for i = 1:(maxnumh*maxnumh),
   b = size(DS(i).symbol);
   if (ismember(DS(i).symbol,name)==0 & b(2)~=0),
```

```
 %Check for the last item in the DS matrix in case it is not in the list yet
if (i==(maxnumh*maxnumh)),
   name = [name, {DS(i).symbol}];
   val = DS(i).symval;
   value(i) = val;
   index = [index; i];

else
 %Check current value against the next value till last item in
%matrix
for j = (i+1):(maxnumh*maxnumh),
   i;
   j;
   c = size(DS(j).symbol);
   if  ((b(2) ~= 0) & (c(2) ~= 0)),
      i;
      j;
      if (strcmp(DS(i).symbol,DS(j).symbol) == 1),
         sprintf('good  - good  - the same');
         if ismember(DS(i).symbol,name) == 1
            value(i) = value(i) + DS(j).symval;
         else
            name = [name, {DS(i).symbol}];
            val = DS(i).symval + DS(j).symval;
            value(i) = val;
            index = [index; i];
         end

      else
         sprintf('good - good - not the same');
         if ismember(DS(i).symbol,name) == 1
         else
            name = [name, {DS(i).symbol}];
            val = DS(i).symval;
            value(i) = val;
            index = [index; i];
         end
      end

   elseif ((b(2) ~= 0) & (c(2) == 0))
      i;
      j;
      sprintf('good - bad');
      if ismember(DS(i).symbol,name) == 1
```

```
            else
               name = [name, {DS(i).symbol}];
               val = DS(i).symval;
               value(i) = val;
               index = [index; i];
            end
         else
            break
         end
      end
   end

   elseif (b(2) == 0),
      sprintf('bad - dont care');
      i;
      j;
      storeZEROname = [storeZEROname; i];
   end
end

%Rearranging the newly created bpm value vector ************************
index;
value;
for i=1:length(index),
   newvalue(i) = value(index(i));
end
newvalue;

%Calculating the K = conflict ***************************************
% e.g. A & B = 0
for i = 1:(maxnumh*maxnumh),
   d = size(DS(i).symbol);
   if (d(2) == 0),
      sprintf('calculating K');
      K = K + DS(i).symval;
   end
end
K;

%The results ********************************************************
newhname = name;
newhvalue = newvalue./(1-K);

return
```

APPENDIX B

MATLAB Code for Implementation of

Adaptive Neuro-Fuzzy Inference System

B.1 FuzzyDiagnosis_cascade.m

```
%*****************************************************************
% Author: Ronald Setia                                           %
% Advisor: Prof. Gary S. May                                     %
% Intelligent Semiconductor Manufacturing Group                  %
% ANFIS Implementation                                           %
%*****************************************************************

clear all

%Load FIS
NFF = readfis ('No Fault Fault 18.fis');              %ANFIS for No Fault or Fault

Fluence = readfis ('Fluence 5.fis');          %ANFIS for failure in Fluence or others
Frequency = readfis ('Frequency 18.fis');     %ANFIS for failure in Frequency or others
Pulses = readfis ('Pulses 12.fis');           %ANFIS for failure in Pulses or others
HePressure = readfis ('Helium 7.fis'); %ANFIS for failure in Helium Pressure or others

WhichFluence = readfis ('Which Fluence 17.fis');    %ANFIS for which fluence error
WhichFreq = readfis ('Which Frequency 19.fis');     %ANFIS for which frequency error
WhichPulses = readfis ('Which Pulses 17.fis');      %ANFIS for which pulses error
WhichPress = readfis ('Which Helium 19.fis'); %ANFIS for which He pressure error

%Load Test Data
test_data = load ('testData.dat');

for i=1:19, %19 Failure modes (16 Failures + 3 Non failures)

   %Get a row
   test = test_data(i,:);
   TestNo(i) = i;
```

```
%Is it a Non-Failure or Failure?
   YesNo_fail = evalfis([test(1) test(2) test(3) test(4) test(5) test(6) test(7) test(8) test(9)
test(10)], NFF);

   %It is a failure with +/- 0.5
   if ((YesNo_fail >= 0.5) & (YesNo_fail < 1.5)),
      ResFail(i) = YesNo_fail;

      %Calculate the chance of being a failure in each of these parameters
      fluence = evalfis([test(1) test(2) test(3) test(4) test(5) test(6) test(7) test(8) test(9)
test(10)], Fluence);
      freq = evalfis([test(1) test(2) test(3) test(4) test(5) test(6) test(7) test(8) test(9)
test(10)], Frequency);
      pulses = evalfis([test(1) test(2) test(3) test(4) test(5) test(6) test(7) test(8) test(9)
test(10)], Pulses);
      pressure = evalfis([test(1) test(2) test(3) test(4) test(5) test(6) test(7) test(8) test(9)
test(10)], HePressure);

       %It is a failure in fluence with +/- 0.5
      if ((fluence >= 0.5) & (fluence < 1.5)),
         ResFlue(i) = fluence;

         %Determine which fluence error
         whichFlue = evalfis([test(1) test(2) test(3) test(4) test(5) test(6) test(7) test(8)
test(9) test(10)], WhichFluence);
         ReswhichFlue(i) = whichFlue;

      else
         ResFlue(i) = fluence;
         whichFlue = evalfis([test(1) test(2) test(3) test(4) test(5) test(6) test(7) test(8)
test(9) test(10)], WhichFluence);
         ReswhichFlue(i) = whichFlue;
      end

       %It is a failure in frequency with +/- 0.5
      if ((freq >= 0.5) & (freq < 1.5)),
         ResFreq(i) = freq;

         %Determine which frequency error
         whichFreq = evalfis([test(1) test(2) test(3) test(4) test(5) test(6) test(7) test(8)
test(9) test(10)], WhichFreq);
         ReswhichFreq(i) = whichFreq;
```

```
        else
            ResFreq(i) = freq;
            whichFreq = evalfis([test(1) test(2) test(3) test(4) test(5) test(6) test(7) test(8)
test(9) test(10)], WhichFreq);
            ReswhichFreq(i) = whichFreq;
        end

        %It is a failure in pulses with +/- 0.5
        if ((pulses >= 0.5) & (pulses < 1.5)),
            ResPulse(i) = pulses;

            %Determine which pulses error
            whichPulse = evalfis([test(1) test(2) test(3) test(4) test(5) test(6) test(7) test(8)
test(9) test(10)], WhichPulses);
            ReswhichPulse(i) = whichPulse;

        else
            ResPulse(i) = pulses;
            whichPulse = evalfis([test(1) test(2) test(3) test(4) test(5) test(6) test(7) test(8)
test(9) test(10)], WhichPulses);
            ReswhichPulse(i) = whichPulse;
        end

        %It is a failure in He pressure with +/- 0.5
        if ((pressure >= 0.5) & (pressure < 1.5)),
            ResHe(i) = pressure;

            %Determine which He pressure error
            whichHe = evalfis([test(1) test(2) test(3) test(4) test(5) test(6) test(7) test(8) test(9)
test(10)], WhichPress);
            ReswhichHe(i) = whichHe;

        else
            ResHe(i) = pressure;
            whichHe = evalfis([test(1) test(2) test(3) test(4) test(5) test(6) test(7) test(8) test(9)
test(10)], WhichPress);
            ReswhichHe(i) = whichHe;
        end

    else  %It is not a failure
        ResFail(i) = YesNo_fail;

        fluence = evalfis([test(1) test(2) test(3) test(4) test(5) test(6) test(7) test(8) test(9)
test(10)], Fluence);
        freq = evalfis([test(1) test(2) test(3) test(4) test(5) test(6) test(7) test(8) test(9)
test(10)], Frequency);
```

```
        pulses = evalfis([test(1) test(2) test(3) test(4) test(5) test(6) test(7) test(8) test(9)
test(10)], Pulses);
       pressure = evalfis([test(1) test(2) test(3) test(4) test(5) test(6) test(7) test(8) test(9)
test(10)], HePressure);
        ResFlue(i) = fluence;
        ResFreq(i) = freq;
       ResPulse(i) = pulses;
       ResHe(i) = pressure;

       whichFlue = evalfis([test(1) test(2) test(3) test(4) test(5) test(6) test(7) test(8) test(9)
test(10)], WhichFluence);
        whichFreq = evalfis([test(1) test(2) test(3) test(4) test(5) test(6) test(7) test(8) test(9)
test(10)], WhichFreq);
       whichPulse = evalfis([test(1) test(2) test(3) test(4) test(5) test(6) test(7) test(8) test(9)
test(10)], WhichPulses);
       whichHe = evalfis([test(1) test(2) test(3) test(4) test(5) test(6) test(7) test(8) test(9)
test(10)], WhichPress);
       ReswhichFlue(i) = whichFlue;
       ReswhichFreq(i) = whichFreq;
       ReswhichPulse(i) = whichPulse;
       ReswhichHe(i) = whichHe;
   end
end

%Printout the results ... ********************************************
S1 = sprintf('=================================================');
S2 = sprintf('                          Failure Diagnosis Results                          ');
S3 = sprintf('-------------------------------------------------------------------------------------');
S4 = sprintf('Test No. | No Failure/ Failure | Fail in Fluence | Fail in Freq | Fail in Pulses |
Fail in He Pressure ');
S5 = sprintf('-------------------------------------------------------------------------------------');
disp(S1);disp(S2);disp(S3);disp(S4);disp(S5);

for j = 1:19,
S6 = sprintf(' %0.4g   |       %0.4g       |      %0.4g     |    %0.4g    |     %0.4g     |
%0.4g        ', TestNo(j), ResFail(j), ResFlue(j), ResFreq(j), ResPulse(j), ResHe(j));
S7 = sprintf('        |                   |      %0.4g     |    %0.4g    |     %0.4g     |       %0.4g
', ReswhichFlue(j), ReswhichFreq(j), ReswhichPulse(j), ReswhichHe(j));
S8 = sprintf('\n');
disp(S6);disp(S7);disp(S8);
end
```

REFERENCES

[1] http://www.prc.gatech.edu (accessed on March 9, 2005).

[2] R. Tummala, "SOP: What Is It and Why? A New Microsystem-Integration Technology Paradigm-Moore's Law for System Integration of Miniaturized Convergent Systems of the Next Decade," *IEEE Trans. Adv. Packag*., vol. 27, no. 2, pp. 241-249, 2004.

[3] T. Ohsaki, E. Sugita, and S. Yamaguchi, "New Thick Film Multilayer Interconnection Technology Using an Nd:YAG Laser," *IEEE Trans. Comp., Hybrids, Manufac. Technol.*, vol. 5, no. 4, pp. 382-388, 1982.

[4] D. Moser, "Lasers Tool Up for Via Formation", *Laser Focus World*, vol. 37, issue 6, pp. 213-214, 2001.

[5] Eric K. W. Gan, H. Y. Zheng, and G. C. Lim, "Laser Drilling of Micro-Vias in PCB Substrates," *Proc. Electron. Packag. Technol. Conf.*, pp. 321-326, 2000.

[6] R. S. Patel and T. F. Redmond, "Via Production Benefits from Excimer-Laser Tools", *Laser Focus World*, vol. 32, issue 1, pp. 71-75, 1996.

[7] K. Prasad and E. Perfecto, "Multilevel Thin Film Packaging: Applications and Processes for High Performance Systems," *IEEE Trans. Comp. Packag., Manufac. Technol. B*, vol. 17, no. 1, pp. 38-49, 1994.

[8] R. S. Patel, T. F. Redmond, C. Tessler, D. Tudryn, and D. Pulaski, "Laser Via Ablation Technology for MCMs Thin Film Packaging – Past, Present, and Future at IBM Microelectronics," *Proc. 27th Interntl. Symp. Microelecton.,* vol. 2369, pp. 31-41, 1994.

[9] T. G. Tessier and G. Chandler, "Compatibility of Common MCM-D Dielectrics with Scanning Laser Ablation Via Generation Processes," *IEEE Trans. Comp., Hybrids, Manufac. Technol.*, vol. 16, no. 1, pp. 39-45, 1993.

[10] E. E. Guzzo and J. S. Preston, "Laser Ablation as a Processing Technique for Metallic and Polymer Layered Structure," *IEEE Trans. Semi. Manufac.*, vol. 7, no. 1, pp. 73-78, 1994.

[11] T. E. Garza-Lopez, E. Sancaktar, and K. L. Mittal, "Excimer lasers: how they work and ablate," *Vacuum Technology & Coating*, pp. 53-59, 2002.

[12] PennWell Corporation, "Industrial Laser Solutions for Manufacturing," vol. 18, issue 10, Oct. 2003 (monthly issue).

[13] E. Locke, E. Hoag, and R. Hella, "Deep Penetration Welding with High-Power CO_2 Lasers," *IEEE Journal of Quantum Electronics*, vol. 8, no. 2, pp. 132-135, 1972.

[14] H. K. Park, C. P. Grigoropoulos, W. P. Leung, and A. C. Tam, "A Practical Excimer Laser-Based Cleaning Tool for Removal of Surface Contaminants," *IEEE Trans. Comp., Hybrids, Manufac. Technol.*, vol. 17, no. 4, pp. 631-643, 1994.

[15] T. Koga, B. –M. Moon, I. Zakharchenko, K. V. Rao, and H. Medelius, "Magnetism and Structure of YBaCuO Superconducting Films Deposited in Unusual Geometries Using Nd:YAG Laser," *IEEE Trans. Magn.*, vol. 29, no. 6, pp. 3601-3603, 1993.

[16] R. D. Schaeffer, "Laser Micromachining", seminar sponsored by the Laser Micromachining Group and Laser Systems Group at Resonetics, www.resonetics.com (accessed on February 24, 2004).

[17] *Private consultation* with Professor Dennis Hess, Department of Chemical and Biomolecular Engineering, Georgia Institute of Technology.

[18] R. Srinivasan and V. Mayne-Banton, "Self-developing Photoetching of Poly (ethylene terephthalate) Films by Far-ultraviolet Excimer Laser Radiation," *Appl. Phys. Lett.*, vol. 41, no. 6, pp. 576-578, 1982.

[19] J. E. Andrew, P. E. Dyer, D. Forster, and P. H. Key, "Direct Etching of Polymeric Materials Using a XeCl Laser," *Appl. Phys. Lett.,* vol. 43, no. 8, pp. 717-719, 1983.

[20] E. Sutcliffe and R. Srinivasan, "Dynamics of UV Laser Ablation of Organic Polymer Surfaces," *J. Appl. Phys.*, vol. 60, no. 9, pp. 3315-3322, 1986.

[21] S. Kuper and M. Stuke, "Ablation of Polytetrafluoroethylene (Teflon) with Femtosecond UV Excimer Laser Pulses," *Appl. Phys. Lett.*, vol. 54, no. 1, pp. 4-6, 1989.

[22] G. H. Pettit and R. Sauerbrey, "Pulsed Ultraviolet Laser Ablation," *Appl. Phys. A: Solids Surf.*, vol. 56, no. 1, pp. 51-63, 1993.

[23] G. H. Pettit and R. Sauerbrey, "Fluence-dependent Transmission of Polyimide at 248 nm Under Laser Ablation Conditions," *Appl. Phys. Lett.*, vol. 58, no. 8, pp. 793-795, 1991.

[24] S. R. Cain, F. C. Burns, C. E. Otis, and B. Braren, "Photothermal Description of Polymer Ablation: Absorption Behavior and Degradation Time Scales," *J. Appl. Phys.*, vol. 72, no. 11, pp. 5172-5178, 1992.

[25] M. Himmelbauer, E. Arenholz, and D. Bauerle, "Single-shot UV-laser Ablation of Polyimide with Variable Pulse Lengths," *Appl. Phys. A: Materials Science & Processing*, vol. 63, pp. 87-90, 1996.

[26] G. C. D'Couto and S. V. Babu, "Heat Transfer and Material Removal in Pulsed Excimer-laser-induced Ablation: Pulse Width Dependence," *J. Appl. Phys.*, vol. 76, no. 5, pp. 3052-3058, 1994.

[27] R. Srinivasan, in *Laser Ablation*, edited by J. C. Miller (Springer, Berlin, 1994), pp. 107-133.

[28] L. V. Zhigilei, P. B. S. Kodali, and B. J. Garrison," A Microscopic View of Laser Ablation," *J. Phys. Chem. B*, vol. 102, no. 16, pp. 2845 – 2853, 1998.

[29] T. W. Hodapp and P. R. Fleming, "Modeling Topology Formation during Laser Ablation," *J. Appl. Phys.*, vol. 84, no. 1, pp. 577-583, 1998.

[30] C. Paterson, A. S. Holmes, and R. W. Smith, "Excimer Laser Ablation of Microstructures: A Numerical Model," *J. Appl. Phys.*, vol. 86, no. 11, pp. 6538 – 6546, 1999.

[31] B. S. Yilbas, "Study of Affecting Parameters in Laser Hole Drilling of Sheet Metals," *Trans. ASME, J. Engng. Mater. Technol.*, vol. 109, pp. 282-287, 1987.

[32] M. Ghoreishi, D. K. Y. Low, and L. Li, "Statistical Modeling of Laser Percussion Drilling for Hole Taper and Circularity Control," *Proc. Instn. Mech. Engrs, part B: J. Engng. Manufact.*, vol. 216, pp. 307-319, 2002.

[33] J. Brannon, "Excimer Laser Ablation and Etching: Making a Mark in Many Applications," *IEEE Circuits & Devices*, vol. 13, no. 2, pp. 11-18, 1997.

[34] W. L. Wang, J. G. Conley, Y. N. Yan, and J. Y. H. Fuh, "Towards Intelligent Setting of Process Parameters for Layered Manufacturing," *J. Intelligent Manufac.*, vol. 11, no. 1, pp. 65-74, 2000.

[35] G. Casalino and F. M. C. Minutolo, "A Model for Evaluation of Laser Welding Efficiency and Quality Using an Artificial Neural Network and Fuzzy Logic," *Proc. Instn. Mech. Engrs, part B: J. Engng. Manufac.*, vol. 218, pp. 641-646, 2004.

[36] B. F. Yousef, G. K. Knopf, E. V. Bordatchev, and S. K. Nikumb, "Neural Network Modeling and Analysis of the Material Removal Process During Laser Machining," *Interntl. J. Adv. Manufac. Technol.*, vol. 22, no. 1-2, pp. 41-53, 2003.

[37] S. Haykin, *Neural Networks: A Comprehensive Foundation*. Macmillan, Inc., Englewood Cliffs, NJ, 1994, pp. 138-229.

[38] D. Montgomery, *Introduction to Statistical Quality Control*. Wiley: New York, 1997.

[39] G. Box, W. Hunter, and J. Hunter, *Statistics for Experimenters*. Wiley: New York, 1978.

[40] C. Himmel and G. May, "Advantages of Plasma Etch Modeling Using Neural Networks Over Statistical Techniques," *IEEE Trans. Semiconduct. Manufact.*, vol. 6, no. 2, pp. 103-111, 1993.

[41] M. Mocella, J. Bondur, and T. Turner, "Etch Process Characterization Using Neural Network Methodology: A Case Study," *SPIE Proc. Module Metrology, Contr., Clustering,* vol. 1594, pp. 232-242, 1991.

[42] Y. Huang, T. Edgar, D. Himmelblau, and I. Trachtenberg, "Constructing a Reliable Neural Network Model for a Plasma Etching Process Using Limited Experimental Data," *IEEE Trans. Semiconduct. Manufact.*, vol. 7, no. 3, pp. 333-344, 1994.

[43] P. J. Cheng and S. C. Lin, "Using Neural Networks to Predict Bending Angle of Sheet Metal Formed by Laser," *International Journal of Machine Tools & Manufacture*, vol. 40, no. 8, pp. 1185-1197, 2000.

[44] D. Goldberg, *Genetic Algorithms in Search, Optimization, and Machine Learning*, Reading, MA: Addison-Wesley, 1989.

[45] G. Shafer, *A Mathematical Theory of Evidence*. Princeton, NJ: Princeton University Press, 1976.

[46] W. Hines and D. Montgomery, *Probability and Statistics in Engineering and Management Science.* New York, Wiley, 1980.

[47] L. A. Zadeh, "Fuzzy Sets as a Basis for a Theory of Possibility," *J. Fuzzy Sets and Systems*, no. 1, pp. 3-28, 1978.

[48] M. Sugeno, *Industrial Applications of Fuzzy Control*. Elsevier Science Pub. Co., 1985.

[49] J. T. Verdeyen, *Laser Electronics.* Upper Saddle River, NJ: Prentice Hall, 1995.

[50] *Private consultation* with Jim Higgins, Light Machinery Inc.

[51] http://www.m-w.com/cgi-bin/dictionary?book=Dictionary&va=ablating (accessed on August 12, 2005).

[52] K. Jain and M. Zemel, “A Comparison of Printed Circuit Board Imaging Technologies,” *Printed Circuit Fabrication*, vol. 24, no. 8, pp. 24, 2001.

[53] K. Jain, M. Zemel, and M. Klosner, “Large-Area, High-Resolution Lithography and Photoablation Systems for Microelectronics and Optoelectronics Fabrication,” *Proceedings of the IEEE*, vol. 90, no. 10, pp. 1681-1688, 2002. (Invited Paper)

[54] http://www.cadence.com (accessed on August 20, 2005).

[55] G. May, “Manufacturing ICs the neural way,” *IEEE Spectr.*, vol. 31, 47-51, 1994.

[56] K. Hornik, M. Stinchcombe, and H. White, “Multilayer feedforward networks are universal approximators,” *Neural Networks,* vol. 2, pp. 359-366, 1989.

[57] D. B. Fogel, “An information criterion for optimal neural network selection,” *IEEE Trans. Neural Networks*, vol. 2, 490-497, 1991.

[58] C. Davis, S. Hong, R. Setia, R. Pratap, T. Brown, B. Ku, G. Triplett, and G. May, "An Object-Oriented Neural Network Simulator for Semiconductor Manufacturing Applications," *IIIS 8th Annual Multi-Conf. Syst. Cybern. Inform.*, vol. V, pp. 365-370, 2004.

[59] http://www.brooks.com/pages/255_rs_series.cfm (accessed on August 20, 2005).

[60] G. Box, *Box on Quality and Discovery with Design, Control, and Robustness.* Wiley: New York, 2000. (Edited by G. Tiao, S. Bisgaard, W. Hill, D. Pena, S. Stigler)

[61] J. H. Holland, *Adaptation in Nature and Artificial Systems.* Ann Arbor, MI: University of Michigan Press, 1875.

[62] J. F. Frenzel, “Genetic Algorithms: A new breed of optimization,” *IEEE Potentials*, vol. 12, no. 3, pp. 21 – 24, 1993.

[63] S. Han and G. May, “Using Neural Network Process Models to Perform PECVD Silicon Dioxide Recipe Synthesis Via Genetic Algorithms,” *IEEE Trans. Semiconduct. Manufact.*, vol. 10, no. 2, pp. 279-287, 1997.

[64] T. Kim and G. May, "Optimization of Via Formation in Photosensitive Dielectric Layers Using Neural Networks and Genetic Algorithms," *IEEE Trans. Electron. Packag. Manufact*., vol. 22, no. 2, pp. 128-136, 1999.

[65] *Private consultation* with Dr. George White, Packaging Research Center at the Georgia Institute of Technology.

[66] D. Y. Shih, H. L. Yeh, J. Paraszczak, J. Lewis, W. Graham, S. Nunes, C. Narayan, R. McGouey, E. Galligan, J. Cataldo, R. Serino, E. Perfecto, C. A. Chang, A. Deutsch, L. Rothman, J. J. Ritsko, and J. S. Wilczynski, "Factors affecting the interconnection resistance and yield in multilayer polyimide/copper structures," *IEEE Trans. Comp., Hybrids, Manufact. Technol.*, vol. 16, no. 1, pp. 74-88, 1993.

[67] J. Boston, "A signal detection system based on Dempster-Shafer theory and comparison to fuzzy detection," *IEEE Trans. Sys. Man and Cybernetics, Part C: applications and reviews*, vol. 30, no. 1, Feb. 2000.

[68] S. J. Hong and G. May, "Neural Network-Based Real-Time Malfunction Diagnosis of Reactive Ion Etching using In-Situ Metrology Data," *IEEE Trans. Semi. Manufac.*, vol. 17, no. 3, pp. 408-421, 2004.

[69] R. Isermann, "Model Based Fault Detection and Diagnosis Methods," *Proc. of the American Control Conf.*, pp. 1605-1609, 1995.

[70] L. A. Zadeh, "Outline of a New Approach to the Analysis of Complex Systems and Decision Processes," *IEEE Trans. Syst. Man Cyber.,* vol. smc-3, no. 1, pp. 28-44, 1973.

[71] The MathWorks, Inc., "Fuzzy Logic Toolbox," (online documentation in HTML format);http://www.mathworks.com/access/helpdesk/help/toolbox/fuzzy/index.html (accessed on May 12, 2005).

[72] J. S. Jang, "ANFIS: Adaptive-Network-Based Fuzzy Inference System," *IEEE Trans. Syst., Man, Cybern.,* vol. 23, no. 3, pp. 665-685, 1993.

[73] M. A. Awadallah, M. M. Morcos, S. Gopalakrishnan, and T. W. Nehl, "A Neuro-Fuzzy Approach to Automatic Diagnosis and Location of Stator Inter-Turn Faults in CSI-Fed PM Brushless DC Motors," *IEEE Trans. Energy Conversion*, vol. 20, no. 2, pp. 253-259, 2005.

[74] M. A. Awadallah and M. M. Morcos, "Switch Fault Diagnosis of PM Brushless DC Motor Drive Using Adaptive Fuzzy Techniques," *IEEE Trans. Energy Conversion*, vol. 19, no. 1, pp. 226-227, 2004.

[75] R. T. Lauer, B. T. Smith, and R. R. Betz, "Application of a Neuro-Fuzzy Network for Gait Event Detection Using Electromyography in the Child With Cerebral Palsy," *IEEE Trans. Biomed. Eng.,* vol. 52, no. 9, pp. 1532-1540, 2005.

VITA

Ronald Setia was born on February 24, 1978 in Münster, Germany. He attended Canisius College Senior High School in Jakarta, Indonesia and graduated in May 1996. He continued his academic career at the University of Notre Dame in Sound Bend, Indiana, USA, where he received the Bachelor of Science in computer engineering in May 2000. He graduated *magna cum laude*. During his study at Notre Dame, he was invited to join two prestigious engineering honor societies: Tau Beta Pi and Eta Kappa Nu. Ronald Setia continued his studies at the Georgia Institute of Technology in Atlanta, Georgia, USA. He received the Master of Science degree in electrical and computer engineering in December 2001. During summer of 2001, he worked as a process engineer intern at IBM Corporation in East Fishkill, New York. In January 2002, he joined the Intelligent Semiconductor Manufacturing Group at Georgia Tech under the supervision of Professor Gary S. May. Since then he has been a Graduate Research Assistant.

Ronald's doctorate thesis focuses on modeling and diagnosis of excimer laser ablation. In his research, artificial intelligent (AI) techniques – including neural networks and genetic algorithms – and statistical methods were used to characterize, model, and optimize the laser ablation process. He also applied AI techniques to detect and diagnose failures in the process. He has published two IEEE Transaction papers and several conference papers. He is interested in integrated-circuit manufacturing, microsystems packaging, micro-electromechanical systems, and nanotechnology.

PUBLICATIONS

Journal Publications

[1] **R. Setia** and G. S. May, "Modeling and Optimization of Via Formation in Dielectrics by Laser Ablation Using Neural Networks and Genetic Algorithms," *IEEE Transactions on Electronics Packaging Manufacturing*, vol. 27, no. 2, 2004.

[2] **R. Setia** and G. S. May, "Run-to-Run Failure Detection and Diagnosis using Neural Networks and Dempster-Shafer Theory: An Application to Excimer Laser Ablation," accepted for publication in *IEEE Transactions on Electronics Packaging Manufacturing*, September 2005.

[3] J. Sutanto, **R. Setia**, A. Papania, G. S. May, and P. J. Hesketh, "Using Neural Networks to Model an Electromagnetic-Actuated Microactuator," submitted to *IoP Journal of Micromechanics and Microengineering,* July 2005.

[4] **R. Setia** and G. S. May, "In-Line Failure Detection and Diagnosis of Excimer Laser-Based Microvia Fabrication Using Computational Intelligence," submitted to *LIA Journal of Laser Applications*, November 2005.

Conference Publications

[1] **R. Setia** and G. S. May, "Using Neural Networks and Dempster-Shafer Theory for Failure Detection and Diagnosis of Excimer Laser Ablation," *LIA 24th International Congress on Applications of Lasers & Electro-Optics: Laser Microfabrication*, pp. 125-134, Miami FL, USA, 2005.

[2] **R. Setia** and G. S. May, "Comparison of Intelligent Modeling Techniques Applied to Microvia Formation using Excimer Laser Ablation," *IIIS 9th World Multi-Conference on Systemics, Cybernetics and Informatics*, vol. VI, pp. 224-230, Orlando FL, USA, 2005.

[3] **R. Setia**, J. S. Bintoro, A. Papania, G. S. May, and P. J. Hesketh, "Artificially Intelligent Models of an Electromagnetic-Actuated Microactuator: An Application of Neural Networks in MEMS," *TIMA/IEEE Symposium on Design, Test, Integration, and Packaging of MEMS/MOEMS*, pp. 125-130, Montreux, Switzerland, 2005.

[4] **R. Setia**, G. S. May, V. Sundaram, R. R. Tummala, and H. H. Roh, "Sensitivity Analysis and Optimization of Excimer Laser Ablation for Microvia Formation using Neural Networks and Genetic Algorithms," *IEEE/SEMI 29th International Electronics Manufacturing Technology Symposium*, vol. 29, pp. 131-139, San Jose CA, USA, 2004.

[5] C. Davis, S. J. Hong, **R. Setia**, R. Pratap, T. Brown, B. Ku, G. Triplett, S.S. Han, and G. S. May, "An Object-Oriented Neural Network Simulator for Semiconductor Manufacturing Applications," *IIIS 8th World Multi-Conference on Systemics, Cybernetics and Informatics*, vol. V, pp. 365-370, Orlando FL, USA, 2004.

[6] **R. Setia** and G. S. May, "Modeling The Laser Ablation Process Using Neural Networks," *ASME Advances in Electronic Packaging*, vol. 1, pp. 161-167, Maui HI, USA, 2003.

[7] **R. Setia** and G. S. May, "Neural Network Modeling of the Resistance of Metallized Vias Formed by Laser Ablation in Polymer Dielectrics," *IEEE 15th Biennial University/Government/Industry Microelectronics Symposium*, pp. 236–240, Boise ID, USA, 2003.

[8] **R. Setia** and G. S. May, "A Neuro-Fuzzy Approach to Failure Detection and Diagnosis of Excimer Laser Ablation in Microvia Formation," *SPIE International Symposium on Lasers and Applications in Science and Technology*, San Jose CA, USA, 2006. (Accepted for publication)